Modelling, Simulation, and Optimization of Molecular Breast Tomosynthesis

van Roosmalen, Jarno

Citation (APA)
van Roosmalen, J. (2018). Modelling, Simulation, and Optimization of Molecular Breast Tomosynthesis DOI:
10.4233/uuid:c07810d6-5c8c-4f84-ba36-f1c146beae77

Modelling, Simulation and Optimization of Molecular Breast Tomosynthesis

Jarno van Roosmalen

Modelling, Simulation, and Optimization of Molecular Breast Tomosynthesis

Jarno van Roosmalen

Modelling, Simulation, and Optimization of Molecular Breast Tomosynthesis

Dissertation

for the purpose of obtaining the degree of doctor
at Delft University of Technology,
by the authority of the Rector Magnificus prof.dr.ir. T.H.J.J. van der Hagen,
chair of the Board for Doctorates
to be defended publicly on
Tuesday 3 July 2018 at 15:00 o'clock

by

Jarno VAN ROOSMALEN

Master of Science in Industrial and Applied Mathematics,
Eindhoven University of Technology, the Netherlands
born in 's-Hertogenbosch, the Netherlands

This dissertation has been approved by the promotor.

Composition of the doctoral committee:
Rector Magnificus   chairperson
Prof. dr. F. J. Beekman,   Delft University of Technology, promotor
Dr. ir. M. C. Goorden   Delft University of Technology, copromotor

independent members:
Dr. L. de Wit-van der Veen   NKI-AVL
Prof.dr. P.L. Jager   McMaster University, Canada
Prof.dr. J.F. Verzijlbergen   Radboud University Nijmegen
Prof.dr.ir. N. Karssemeijer   Radboud University Nijmegen
Prof.dr. B. Rieger   Delft University of Technology

Reserve member:
Prof.dr. P. Dorenbos   Delft University of Technology

To My Parents

"It is not the critic who counts; not the man who points out how the strong man stumbles, or where the doer of deeds could have done them better. The credit belongs to the man who is actually in the arena, whose face is marred by dust and sweat and blood; who strives valiantly; who errs, who comes short again and again, because there is no effort without error and shortcoming; but who does actually strive to do the deeds; who knows great enthusiasms, the great devotions; who spends himself in a worthy cause; who at the best knows in the end the triumph of high achievement, and who at the worst, if he fails, at least fails while daring greatly, so that his place shall never be with those cold and timid souls who neither know victory nor defeat."

Theodore Roosevelt
Excerpt from the speech "Citizenship In A Republic"
delivered at the Sorbonne, in Paris, France on April 23th, 1910

Contents

Chapter 1

Introduction

Medical imaging technology has become an integral part of modern medicine as it enables non-invasively visualizing the interior of a patient to establish a medical diagnosis, to select, plan or monitor a therapy or to assess its outcome. Many different imaging techniques exist with a multitude of clinical applications in e.g. cardiology, neurology, and oncology. This thesis is concerned with the development of a new imaging tool dedicated to detecting and characterizing breast cancer. Breast cancer is one of the most common forms of female cancers and it is a leading cause of death for women in developed countries (Torre et al., 2015; Ferlay et al., 2015). Improving breast imaging technology could lead to earlier and/or more accurate diagnosis, which in turn may result in better patient outcomes. Moreover, improved imaging technology may be vital for more accurate personalized medicine e.g. to support selection of therapies for individual patients and to monitor the effects of the chosen therapy at short notice (Mankoff et al., 2007).

Below we provide a short overview of different imaging modalities (i.e. types of imaging techniques) dedicated to breast imaging. We start with describing anatomical breast imaging modalities which can provide insight in the location of different tissue types. Next, we discuss the class of molecular imaging techniques that provide functional breast images revealing different cell properties. As the scanner developed in this work belongs to the latter class we will describe the properties of molecular imaging in detail. For thorough review articles of breast imaging technologies, the reader is referred to Hruska and O'Connor (2013); Sechopoulos (2013); Menezes et al. (2014) and Fowler (2014).
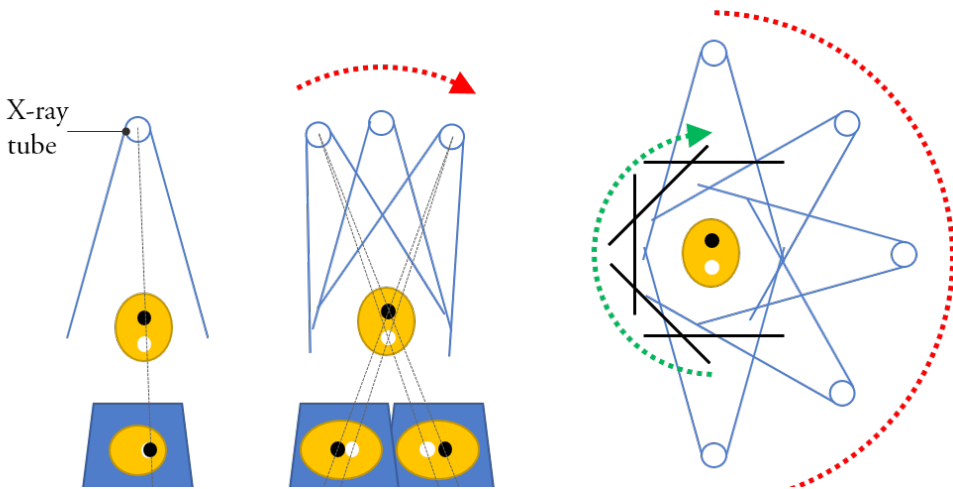
Figure 1-1 Illustration of different x-ray imaging modalities. (a) A direct planar x-ray detector image is formed when x-ray tube and detector are stationary. (b) X-ray tomosynthesis, in which a set of detector images is acquired over a limited angular range by moving the x-ray source. From these detector images, a 3D image of the object is reconstructed. (c) X-ray Computed Tomography, in which detector images are collected from all around the object (at least 180 degree angular range) by moving the x-ray source and the detector. A 3D reconstructed image is then calculated from these detector images.

1.1 Anatomical Breast Imaging Modalities

The most well-known and most widespread modality in breast cancer imaging is x-ray mammography where x-rays are transmitted through a strongly compressed breast to form a planar (2D) image of the breast on the detector. Image contrast between different structures in the breast is caused by differences in x-ray attenuation of different tissues. Many countries have large-scale breast cancer screening programs using mammography, e.g. in the Netherlands all women between 50 and 75 years are invited for screening every two years. Clinical trials indicate that large scale regular screening of women above a certain age could reduce mortality due to breast cancer (Nyström et al., 2002; Otto et al., 2003). Although mammography is a mature technology, it has still seen improvements in recent years. When introduced in the 1970s, mammography used screen-film to record images, while nowadays screen-film has been replaced by digital mammography which increased the sensitivity, i.e. the fraction of cancers detected (Zackrisson and Houssami, 2016).

Although mammography is standardly applied for breast cancer diagnosis and results in high resolution images of the breast, it also has its disadvantages. Because mammography only acquires planar images, malignancies can be hidden by overlying tissues, which occurs more often for women with dense breast tissue. Such an occlusion of features by overlying tissue could be resolved by using a 3D imaging technique. Other advantages of 3D imaging include enabling estimation of the depth at which a tumour is located, and providing more information on tumour size and shape. Figure 1-1 illustrates in general the difference between planar x-ray imaging and two types of 3D imaging techniques: x-ray tomosynthesis and x-ray Computed Tomography (CT). X-ray CT is a well-known 3D modality that has been around for several decades, and is widely used for a large variety of indications and for almost any organ. During a modern CT scan the source and detector rotate around the patient to acquire many 2D projections (see Figure 1-1(c)), normally over an arc of 360 degrees. A 3D image of the object is then reconstructed from all these 2D detector images. As the rotation of source and detector is usually around a patient lying on a dedicated scanning table transparent to x-rays, CT scanners do not just image the breast. This implies delivery of radiation dose to a larger part of the patient's body than would be strictly required. Moreover, this set-up causes large scatter effects, strong x-ray attenuation, and other beam degradation effects. These are some of the reasons that x-ray CT is not commonly used for breast cancer screening. As a compromise between x-ray mammography and x-ray CT, x-ray tomosynthesis dedicated to breast imaging has attracted much interest over the last decade. In this technique, the x-ray tube moves in an arc over the compressed breast acquiring x-ray projections from a limited number of angles (see Figure 1-1(b)) from which a 3D image of the breast is then reconstructed. This way, although the range of viewing angles is less than what is used in CT, breast images still contain some 3D information. Recently, several large trials showed a good potential for x-ray tomosynthesis to replace mammography in large-scale screening programs (Sechopoulos, 2013; Skaane et al., 2014; Hammond et al., 2015; Lång et al., 2015).

Besides CT and x-ray tomosynthesis, other imaging modalities based on different image forming principles are also used for anatomical breast imaging. Examples include Ultra Sound imaging (US), or Magnetic Resonance Imaging (MRI), which mostly perform anatomical imaging. US is often used as an adjunct modality to mammography, and its imaging forming principle is based on the reflective properties of tissues for ultrasonic sound waves. It has the advantages that it doesn't use harmful ionizing radiation, is inexpensive and requires no contrast injections. Moreover, it can be used easily to support taking biopsies. However, the results are highly dependent on the skills of the technologist and vary between users making it hard to standardize these scans. MRI is based on the behaviour of nuclear spins in a strong magnetic field and basically shows the density of hydrogen atoms (i.e. water and fat) in tissues. MRI is often used for high-risk patients. It has been shown to have a high sensitivity for detecting tumours (Plana et al., 2012). However, MRI is relatively expensive, is not tolerated by all patients, and has a lower specificity (i.e. the fraction of negative cases classified as such) than for example mammography (Drukteinis et al., 2013; Schneble et al., 2014).

1.2   Molecular Breast Imaging Modalities

A tumour can also be detected and/or characterized by injecting specific tumour targeting molecules that send out photons that can be measured outside the patient's body. Both nuclear and optical imaging methods are in use for this purpose and these are complementary, as they reveal different information or are used under different circumstances. However, optical imaging methods suffer from the fact that strong scatter and attenuation of optical photons leads to extremely poor quantification and detectability when a tumour is not located near the body's surface. As a result, diagnostic clinical molecular imaging is currently almost exclusively done with nuclear imaging methods. The injected molecules used for nuclear imaging are labelled with isotopes that emit either single gamma photons or positrons. In case of positrons, these will result in annihilation gamma photons near the positron emission location. Different types of nuclear scanners exist such as planar scintigraphy and Single Photon Emission Computed Tomography (SPECT) which both image single gamma emitters and Positron Emission Tomography (PET) for positron emitters (Cherry et al., 2012). As the breast scanner investigated in this thesis belongs to the class of single gamma emitter imaging, we will zoom in more on its principles in the next sections. After describing the imaging technology, we will discuss the achievements reached with preclinical molecular imaging and the developments in the use of molecular imaging techniques for breast imaging.

Single gamma emitting tracers emit gamma photons of a known fixed energy or multiple known energies isotropically, i.e. in all directions and a fraction of emitted gamma photons will exit the patient's body. This fraction depends on the energy of the gamma photons, and for a tracer to be useful for imaging it must be sufficiently large. Next to the energy of the emitted gamma photons, another important characteristic of radiotracers is their half-life, i.e. the average time in which half the isotopes have decayed. A relatively short half-life is beneficial because only a small amount of the tracer is needed to emit sufficient photons. Moreover, it helps to reduce the
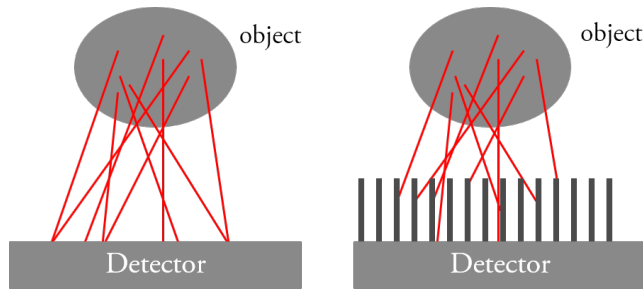
Figure 1-2 Illustration of the need for collimation. (a) Without a collimator, there is no correspondence between location of emission and detection. (b) With a collimator, only radiation from selected directions can reach the detector.

dose to the patient after the scan is finished, although the latter also depends on the way and time span in which the tracer leaves the body, for example via the urine. At the same time, the half-life should be long enough to allow manufacturing, transport, and preparation of the tracer without losing a large fraction of the isotope.

Gamma photons that escaped the body are detected using a gamma camera consisting of a collimator and a gamma detector. Unfortunately, placing a gamma detector directly next to a patient will not result in a usable image, as any point on the detector will detect photons coming from many locations within the patient, which we cannot discriminate as the gamma detectors cannot measure the angle of incidence of detected photons. In optical imaging, this would be resolved by using a lens or reflector. However, in practice high energy gamma photons effectively cannot be reflected or refracted, but directional information can be obtained by using a collimator made of e.g. lead or tungsten which is placed in between patient and gamma detector (see Figure 1-2); a collimator blocks most of the radiation and only lets through photons from certain directions. This way when the gamma detector detects a gamma photon, it contains directional information and based on this information an image can be formed.

1.2.1   Collimation

Several types of collimators exist, such as parallel, diverging, or converging hole collimators, (multi-)pinhole collimators and slit-slat collimators. Figure 1-3 shows an overview.

Figure 1-3 Schematic representation of different collimator types (cross-sections): (a) parallel hole collimator, (b) diverging hole collimator, (c) converging hole collimator, (d) pinhole collimator, and (e) slit-slat collimator, with light-grey indicating a stack of slats perpendicular to the slit.

The parallel hole collimator illustrated in Figure 1-3(a) is the most widely used type of collimator in most nuclear imaging applications. It consists of a s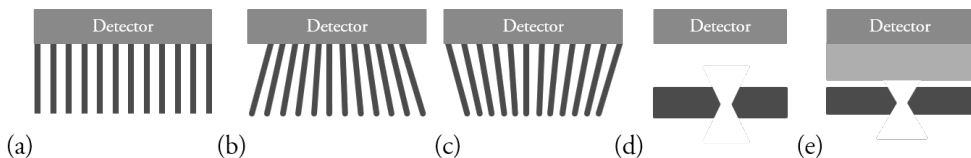lab of a heavy metal (usually a lead or tungsten alloy) with many long parallel holes throughout the material separated by thin septa. These holes restrict the unattenuated gamma photon paths to those travelling more or less perpendicular to the detector surface. By tuning the thickness of the collimator and the hole sizes one can influence the amount of radiation allowed to pass through the collimator. Long narrow holes will lead to high resolution images, but in that case only a small fraction of gamma photons can pass, while shorter wider holes let more radiation pass at the price of more uncertainty on the origin of the gamma photons (Moore et al., 1992; Gunter, 1996; Formiconi et al., 2004). Here resolution is a measure for the smallest details that can be resolved in an image, and a higher resolution implies the ability to resolve smaller details.

When the object to be scanned is smaller than the size of the gamma detector, parallel hole collimators can be transformed into converging collimators, see Figure 1-3(b). In that case in one or two directions the holes are no longer parallel but are all directed towards a common focus point or line. This causes the image of the object to be magnified onto the detector, and as more detector surface is used it improves the sensitivity (i.e. the fraction of emitted radiation that is detected) at the cost of a smaller field-of-view (FOV, the area that is "seen" by the collimator) compared to parallel hole collimation with the same detector. The magnification also leads to improved resolution, as the same detector resolution now corresponds to smaller features in the object (Tsui et al., 1986; Capote et al., 2013). The reverse is also possible resulting in diverging collimators that minify an image onto a smaller detector, see Figure 1-3(c).

A second class of collimators is formed by (multi-) pinhole collimators. Pinhole collimators consist of a large piece (e.g. plate or cylinder) of attenuating material with one or multiple small holes in it, see Figure 1-3(d). Through these holes a projection is created on the detector. Depending on the ratio of the distance between object and pinhole and pinhole and detector the projection is minified or magnified. Like for converging collimators, using magnification allows overcoming the limited resolution of the gamma detectors. By placing multiple pinholes, one can effectively use the surface of a large detector and simultaneously obtain multiple views of an object (Beekman and van der Have, 2007; Rentmeester et al., 2007).

Another type of collimator is the slit-slat collimator, see Figure 1-3(e). It consists of a stack of slabs, acting along one dimension as a parallel hole collimator, and a plate with one or more slits perpendicular to the slats. In this direction, the collimator resembles a pinhole collimator. The idea is to be able to combine the properties of both types of collimators (Metzler et al., 2006; Daekwang and Metzler, 2012).

1.2.2 **Gamma Detectors**
Gamma photons that pass through the collimator ultimately reach the gamma detector. The goal of a gamma detector is to estimate the position and energy of incoming gamma photons. Several types of detectors exist, each with their advantages and disadvantages.
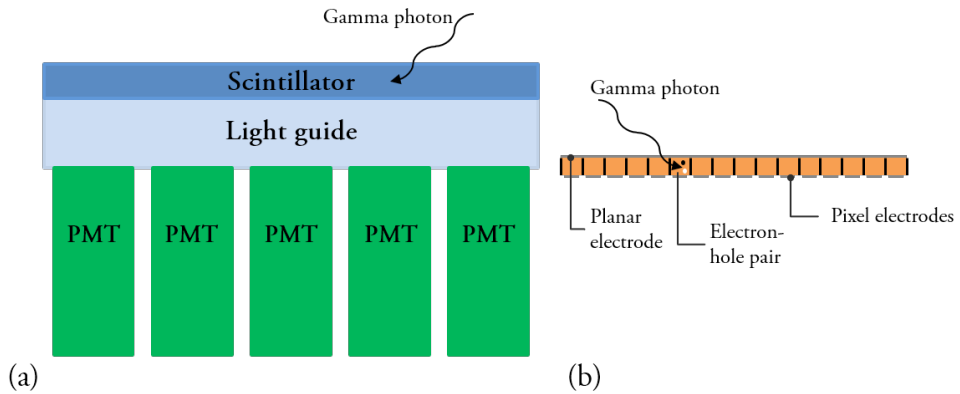
Figure 1-4 Schematic representations of different gamma detectors. (a) A traditional gamma detector with a NaI(Tl) scintillator crystal, a glass light guide and a PMT array. (b) A pixelated CZT detector with the electrodes and an electron-hole pair created by an incoming gamma photon.

Clinical SPECT systems usually employ relatively large detectors (typically in the order of 40 by 50 cm). Such large area gamma detectors are often based on a continuous NaI(Tl) scintillator read-out by an array of photo-multiplier tubes (PMTs) as is visualized in Figure 1-4. The design of this type of detector is virtually unchanged since its inception in the 1960s (Anger, 1964). In the scintillator, a gamma photon is converted into thousands of visible light photons, which are detected and converted into electrical signals by the PMTs. The PMTs' signals are approximately proportional to the amount of incident light photons and are then processed to estimate the position of interaction and the energy of the gamma photon. This estimation can be done using Anger logic (Anger, 1964), which is essentially a weighted average of the signals, or with more advanced methods like Maximum Likelihood (ML) estimation (Barrett et al., 2009; Hesterman et al., 2010).

Recently other detectors have been gaining in popularity. For example, some planar breast imaging systems use Cadmium Zinc Telluride (CZT) detectors (Mueller et al., 2003; Hruska et al., 2008; Hruska et al., 2012), which are semiconductor detectors. The conversion of gamma photon to electrical signal is based on the electron-hole pairs created in the semiconductor by the gamma photon. As a bias voltage is applied over the semiconductor, the electrons and holes drift to the electrodes and create a small current. The advantage of these detectors is that they are more compact and have a better energy resolution of ~6.5% at 140 keV than NaI(Tl)-based detectors with ~10% (Keidar et al., 2016). The most important disadvantage is the cost, as CZT detectors of similar size are considerably more expensive than NaI(Tl)-based detectors.

There are many more detector designs possible, often designed to improve a certain property at the costs of others. For example, NaI(Tl) scintillators can be cut to create discrete pixels, which can improve the resolution at the cost of detection efficiency and manufacturing costs. This then may also require the use of small PMTs or position-sensitive PMTs for read-out which increases

the cost of the detector even further. Recently, PMTs have started to be replaced by Silicon PMs (SiPMs), which are semiconductor chips containing many small avalanche photo-diodes.

1.2.3 Preclinical achievements

Dedicated SPECT to image small animals is key in pharmaceutical research, e.g. for developing new tracers, testing new cancer therapies, understanding diseases etc. In the past 15 years there has been considerable progress in the performance of these preclinical scanners (Peterson and Shokouhi, 2012). As many methods in this thesis are based on preclinical achievements we discuss some of them here shortly.

The small size of the animals involved in preclinical imaging (e.g. a mouse weighs roughly 1/3000 of a human) means high resolution imaging is required. At the same time, the small size of the animal allows easy use of detectors much larger than the object, which enables exploitation of pinhole magnification. Therefore, multi-pinhole collimators are now routinely used in small animal SPECT (Peterson and Shokouhi, 2012). Another advantage of using multi-pinhole collimators is that pinholes can be arranged in such a way that sufficient angular sampling is achieved in a central region without requiring any scanner movement. This central focal region can still be moved over the object to scan larger areas (Vastenhouw and Beekman, 2007; Vaissier et al., 2012). In contrast, in traditional SPECT scanners the parallel hole collimator and detector rotate around the object to acquire projections over different angles.

Using such focused pinhole collimation enables achieving resolutions better than 0.25 mm in mice (Ivashchenko et al., 2014) while using NaI(Tl)-based gamma detector with only 3.5 mm resolution. These very high resolutions are very important in certain applications, like mouse joint imaging. In other applications, resolution is less important, and a high sensitivity is preferred, e.g. to work with low dose, or to follow fast processes in vivo. Recently developed collimators were able to reach a sensitivity of 1.3% while still achieving a 0.85 mm resolution and were able to image only a quarter MBq of activity (Ivashchenko et al., 2015).

1.2.4 Nuclear breast imaging modalities

Having explained the basics of nuclear imaging with single gamma emitters, we come back to breast imaging and discuss the existing nuclear breast imaging modalities. Different nuclear imaging modalities exist that can either provide 2D or 3D images. Planar imaging is often accomplished with parallel hole collimators that create a direct projection of the object onto the detector and in case of breast imaging this is called molecular breast imaging (MBI) or alternatively breast single gamma imaging (BSGI) or mammo-scintigraphy (Rhodes et al., 2005; Brem et al., 2008; O'Connor et al., 2008; O'Connor et al., 2009). MBI is being used as an adjunct to mammography, but several trials are investigating its use in screening programs (Hruska, 2016; Shermis et al., 2016).

Several groups have already attempted 3D imaging of single photon emitting tracers in breasts. Modalities providing 3D information include SPECT, and molecular breast tomosynthesis

(MBT) (Madhav et al., 2006; Williams et al., 2010; Perez et al., 2011; Gopan et al., 2014; Gong and Williams, 2015).

Dedicated breast PET systems (sometimes known as Positron Emission Mammography (PEM)) are also under development (Kalles et al., 2013; Abreu et al., 2006; Luo et al., 2010; Miyake and Nakamoto, 2017). Most of these systems are in their early evaluation stages. For an overview of recent developments see Miyake et al. (2016).

1.3   Reconstruction Algorithms

In planar imaging modalities, the acquired projection images are used directly. For all of the 3D imaging modalities -including SPECT, PET, and tomosynthesis- the acquired data has to be processed to retrieve the 3D distribution of the tracer, a process called reconstruction (Qi and Leahy, 2006). There are several algorithms available for reconstruction of tomographic emission data. The two most important algorithms are Filtered Back Projection (FBP) and Maximum Likelihood Expectation Maximization (MLEM) (Shepp and Vardi, 1982; Lange and Carson, 1984).

Filtered back projection or FBP is an algorithm out of the class of analytic reconstruction methods. These analytic methods calculate the activity distribution in one step based on the projection data. FBP assumes that the recorded projection is approximately a line integral over the activity distribution at each point. It was initially developed for classical scanners with parallel hole collimation where the lines are parallel to each other and perpendicular to the detector. By rotating the camera around the patient, many such projections are recorded under different angles. This process can mathematically be represented as the Radon-transform of the activity distribution. The FBP reconstruction algorithm calculates the discrete inverse Radon-transform. The algorithm back projects the image of each projection along the lines of incidence and sums them using a filter that weighs the contributions. This algorithm was later extended to include converging
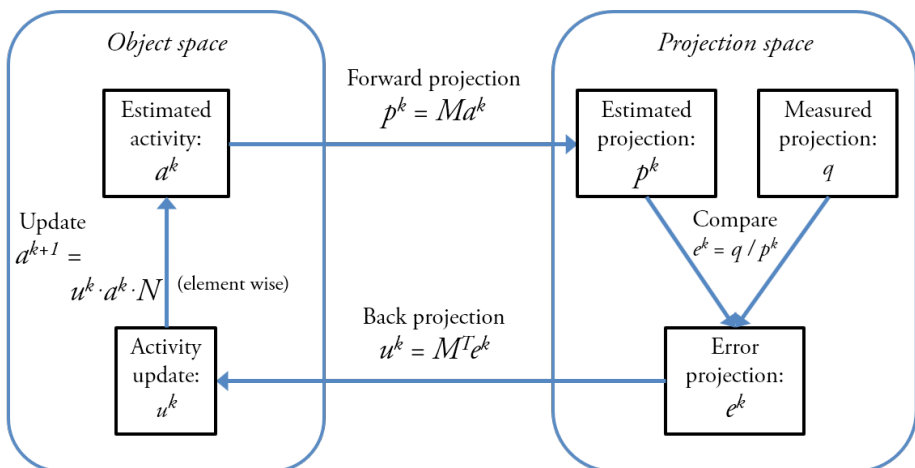

Figure 1-5 A schematic overview of the steps in the MLEM reconstruction method

collimators, where by rebinning and reordering, a parallel set of projections can be created. This is much harder to do for more complex geometries like pinhole collimators. In general, FBP is fast and easy to use. However, FBP assumes that one has an unlimited number of projections and perfect noiseless data. This is not reachable in practise and can cause image artefacts. Other approximations are made, such as ignoring the finite collimator and/or detector resolution.

A second class of algorithms of which MLEM and its variants are important examples, consists of iterative methods. These have been shown to be more robust to noise than FBP and they allow implementing all physical processes of photon transport in the scanner. MLEM is derived by modelling the counting statistics of the projection data, and provides the most likely distribution of activity that could have created the measured projection data. An overview of iterative reconstruction methods can be found in Qi and Leahy (2006).

MLEM starts with an initial guess of the tracer distribution, which is updated in each iteration to improve the estimate. Here we describe how MLEM operates, see also Figure 1-5 for an illustration. The process of forming a projection in a scanner can be written as

$$p = \mathrm{M}\, a + n.$$

Here a is a vector representing the 3D activity distribution, p is the measured projection data (i.e. the number of detected gamma photons in each pixel), M is a matrix with elements representing the probability that a photon emitted in a certain voxel is detected in a specific pixel, and lastly n is a noise component. The goal of the MLEM algorithm is to find -given p, knowing M, and with a statistical model for n- the distribution a that is most likely to have generated the measured projections p. The basic steps of a MLEM reconstruction are as follows. The current estimate a^k of the activity is projected using the model M to obtain estimated projections p^k. The estimated projections are then compared to the measured projections q resulting in error projections. These are back projected into image space using the transverse model M^T resulting in an activity error map which is then used to generate a new activity estimate a^{k+1}, taking into account a normalisation factor N. With this new activity estimate, a new projection p^{k+1} is then estimated. This is repeated till the desired number of iterations has been reached.

The reconstruction algorithms can only provide accurate reconstructions if the model M contains all the relevant physics of the imaging process. In practise, it is often unavoidable to make approximations.

1.3.1 *Interaction of gamma photons with matter*
To be able to model the image formation process in a nuclear imaging device, we should understand which types of interaction occur when a gamma photon passes through the human body, the collimator and interacts with the detector. Here, we will restrict ourselves to those interactions relevant for the models used in this thesis. For a more comprehensive treatment, the reader is referred to Wernick and Aarsvold (2004) or Shultis and Faw (2016). A first interaction

that can occur is absorption of the gamma photon via the photoelectric effect. This occurs mostly when the gamma photons interact with one of the electrons in the inner shell of the atoms. The photoelectric effect effectively results in the absorption of the gamma photon and when it occurs in the patient or collimator it decreases the fraction of photons reaching the detector. A second type of interaction is Compton scatter. In this case, a photon interacts with one of the outer electrons and as a result changes direction and loses part of its energy. So, when it is detected, the photon path assumed by the reconstruction algorithm is not correct (unless explicit care is taken to model this in at least a statistical sense), as it is not a straight path. Therefore, it can cause activity to be reconstructed in the wrong place. If a photon scatters in the detector, instead of the patient or collimator, it only deposits parts of its energy. This can result in errors in the energy and/or position estimate for the detected gamma photon.

1.4   Simulations

For the evaluation and optimization of new scanners, it is beneficial to be able to perform computer simulations. Simulations allow assessing if a concept may work before building an expensive device, and if the expected results offer sufficient improvement over existing technology. Moreover, simulations allow easy manipulation of many parameters, which is not always possible in real devices. Simulation is a very broad term, and can mean many things. In the context of this thesis, simulations are performed to either mimic the process of generating projection data like the output generated by a physical scanner or to acquire reconstructed images by including processing of the raw data. Note that the reconstruction software also requires a good model of the scanner, and therefore has very similar components as the software for generating projections. In general, there are a few different classes of software that can be used for the modelling of a nuclear imaging device.

One class consists of analytical methods to describe the interactions of the gamma photons with materials in an average or statistical sense. This kind of software provides the user with the probability that a photon emitted in a certain voxel will be detected in a certain detector pixel, exactly what is needed in reconstruction software. When generating simulated projections, these probabilities can be used to generate a noise realization from the appropriate Poisson distribution to simulate a scan that could correspond to these probabilities. These kinds of analytical methods uses a macroscopic view of the system. Advantages of these methods include direct access to the probabilities, and a reasonable speed as it describes the average behaviour of the system, and does not look at individual gamma photons. Disadvantages are that the physical processes considered are usually limited to those that can be easily modelled analytically on a macroscopic scale.

The second class contains Monte Carlo (MC) methods, called so for their use of random numbers in the simulation. For the simulation of nuclear imaging devices, MC simulations often follow individual particles and decide along their trajectory what interactions they undergo in the different materials, tracking any secondary particles that are produced. MC thus often models the physics at a more microscopic level. An advantage of this kind of method is that it is possible

to include many physical processes like scattering very precisely in the model. However, MC methods are also notoriously slow (even when acceleration techniques are used) as many particles must be simulated to obtain sufficient statistics. They thus require large and often inhibitory amounts of computational power.

1.5   Thesis outline

This thesis focuses on the modelling, simulation, and optimization of a molecular breast tomosynthesis device. In **Chapter 2**, this system is introduced and in a simulation study we show the potential benefits of MBT over existing planar MBI systems.

In **Chapter 3**, we evaluate the simulation software used throughout this thesis, by comparing our in-house developed voxelized ray-tracer which includes several approximations with an existing MC simulation package which is considered to provide the ground-truth. We show that sufficient accuracy can be achieved using our dedicated software while reducing the computational burden significantly. Specifically, we validate that the choice to not model scattered gamma photons coming from the patient's torso and reaching the detector is justified when simulating MBT scans.

Analytical evaluation of collimator design requires closed form expressions for the resolution and sensitivity of collimators. In **Chapter 4**, we derive a new expression for the sensitivity of converging SPECT collimators. In contrast to existing expressions, this expression does not diverge near the focal region and is valid over the whole FOV of the collimator. This allows the optimization of collimators for which the focal length is close to or in the object of interest.

The MBT system introduced in **Chapter 2**, is being optimized in **Chapter 5**. In this chapter, we focus on optimal pinhole collimation and optimal choice of detector type. Using analytical formulas, we find that there is an optimal detector-breast distance that provides the highest sensitivity at a given system resolution. Scanners with such optimized detector-breast distances are then evaluated by performing full system simulations using the software from **Chapter 3**. This way we investigate which system resolution is best for lesion detection. This analysis includes both conventional gamma detectors as well as modern CZT detectors, which we show to result in a similar scanner performance.

As other collimators than pinhole collimators could be useful for MBT, we optimize collimation using fan beam and slit-slat collimators for MBT in **Chapter 6**. In the analytical analysis of fan beam collimators, we use the formula derived in **Chapter 4**. For the optimized geometries, we conduct full system simulations and we compare the resulting images with those obtained with the optimal pinhole designs (**Chapter 5**).

Lastly **Chapter 7** gives a summary of the results in this thesis, and discusses recommendations for further research.

Chapter 2

Molecular breast tomosynthesis with scanning focus multi-pinhole cameras

This chapter is adapted from:

Abstract

Planar molecular breast imaging (MBI) is rapidly gaining in popularity in diagnostic oncology. To add 3D capabilities, we introduce a novel Molecular Breast Tomosynthesis (MBT) scanner concept based on multi-pinhole collimation. In our design, the patient lies prone with the pendant breast lightly compressed between transparent plates. Integrated webcams view the breast through these plates and allow the operator to designate the scan volume (e.g. a whole breast or a suspected region). The breast is then scanned by translating focusing multi-pinhole plates and NaI(Tl) gamma detectors together in a sequence that optimizes count yield from the volume-of-interest. With simulations, we compared MBT with existing planar MBI. In a breast phantom containing different lesions, MBT improved tumour-to-background contrast-to-noise ratio (CNR) over planar MBI by 12% and 111% for 4.0 and 6.0 mm lesions respectively in case of whole breast scanning. For the same lesions, much larger CNR improvements of 92% and 241% over planar MBI were found in a scan that focused on a breast region containing several lesions. MBT resolved 3.0 mm rods in a Derenzo resolution phantom in the transverse plane compared to 2.5 mm rods distinguished by planar MBI. While planar MBI cannot provide depth information, MBT offered 4.0 mm depth resolution. Our simulations indicate that besides offering 3D localization of increased tracer uptake, multi-pinhole MBT can significantly increase tumour-to-background CNR compared to planar MBI. These properties could be promising for better estimating the position, extend and shape of lesions and distinguishing between single and multiple lesions.

2.1   Introduction

Mammography is currently the most frequently used imaging modality in breast cancer screening, as it allows for performing fast, high-resolution, and relatively low-dose imaging of the breast. Nevertheless, mammography has its limitations; it is widely recognized that for women with radiographically dense breasts, the sensitivity and specificity of mammography are significantly reduced (Kolb *et al.*, 2002; Carney *et al.*, 2003; Pisano *et al.*, 2008). Therefore, other modalities such as ultrasound imaging, X-ray tomosynthesis, Magnetic Resonance Imaging, Positron Emission Tomography, Molecular Breast Imaging (MBI) and Single Photon Emission Computed Tomography (SPECT) are actively being investigated to complement or replace mammography for some groups of patients (Harris, 2010; Lee *et al.*, 2010). For a comprehensive review of the different breast imaging modalities we refer to Hruska and O'Connor (2013), and Fowler (2014).

Different imaging modalities can provide complementary types of information. Functional nuclear imaging techniques, which visualize uptake of radio-labelled molecules have the ability to visualize the physiology of breast tissue opposed to just its anatomic appearance. Therefore,

these techniques cannot solely detect tumours, but they may also reveal specific characteristics of the cancer and indicate possible response to therapy, or be used for therapy follow-up (Mankoff *et al.*, 2007). Benefits of functional techniques are widely recognized as shown by the recent development of dedicated breast PET systems (Miyake *et al.*, 2014) and several dedicated planar breast imaging systems for single photon emitting tracers. These planar systems are known under a wide range of names such as Breast Specific Gamma Imaging, MBI and, mammo-scintigraphy (O'Connor *et al.*, 2008; Brem *et al.*, 2008; Hruska *et al.*, 2012b; Dickerscheid *et al.*, 2013; Sun *et al.*, 2013). We will here collectively refer to them as planar MBI. Planar MBI was initially developed as an alternative imaging modality for specific patient groups, like women with dense breasts (O'Connor *et al.*, 2007). Recently, there has been a very active development in planar MBI instrumentation, resulting in strong sensitivity improvements. This enabled the use of a lower dose, which may open up the possibility for using MBI in breast cancer screening.

Planar (2D) breast imaging has the disadvantage that it does not provide information on the depth of a suspect lesion and that malignant features may be obscured by overlapping breast tissue. As an extension to 2D mammography, X-ray tomosynthesis (which adds 3D information to mammography) is currently growing in popularity (Sechopoulos, 2013) as several screening studies demonstrated improved lesion detection and reduced recall rates of X-ray tomosynthesis over mammography (Skaane *et al.*, 2013; Lång *et al.*, 2015). Given these results, it may be worthwhile to explore similar extensions for planar MBI. Besides providing 3D tumour localization, 3D information may allow discriminating between a large tumour and several small ones close together and enable better estimation of its size and shape. Several groups have already attempted 3D imaging of single photon emitting tracers in breasts using dedicated SPECT or molecular tomosynthesis systems (Madhav *et al.*, 2006; Williams *et al.*, 2010; Perez *et al.*, 2011; Gopan *et al.*, 2014; Gong and Williams, 2015). However, compared to recent planar systems, the sensitivity-resolution trade-offs of these scanners are still sub-optimal, mainly due to the relatively large distance between breast and detector.

One way to achieve 3D molecular breast imaging with high resolution and sensitivity could be by utilizing and adapting techniques from the field of preclinical SPECT which has seen much innovation and progress in the past decade (Peterson and Furenlid, 2011; Peterson and Shokouhi, 2012). Modern small animal SPECT commonly uses pinhole collimators to project the tracer distributions onto the gamma detectors. To obtain high-count yields from a specific volume-of-interest (VOI), such as an organ or tumour, one can use focusing multi-pinhole geometries (Beekman and van der Have, 2007; van der Have *et al.*, 2009). In this class of scanners, the user can designate a specific scan volume, e.g. by using a graphical user interface based on optical cameras that view the subject. The subject is then stepped in a specific sequence through the scanner in order to optimize the count yield from the VOI. Such focusing multi-pinhole collimators may also be well suited for high resolution and high sensitivity imaging of breast tumours (Branderhorst *et al.*, 2011; Branderhorst *et al.*, 2014), while maintaining excellent capabilities for imaging the entire breast.

In this work, we explore the use of a focusing multi-pinhole geometry for 3D breast imaging. The design is based on two multi-pinhole plates acting as collimators that are placed in close proximity to a lightly compressed breast. With this geometry, data is acquired over a limited range of angles similar to X-ray tomosynthesis. The breast is viewed through transparent compression plates by webcams, which allow the user to select the VOI to be scanned on a graphical interface. The aim of this paper is to present and evaluate this novel dedicated molecular breast tomosynthesis (MBT) scanner design. With simulations, we (i) compare MBT's performance with recently developed planar MBI, (ii) evaluate the ability to collect depth information for tumour detection, and (iii) investigate if and how much MBT scans are improved by focusing on a VOI instead of imaging the whole breast.

2.2   Methods

In this section, we describe the novel MBT design as well as the planar MBI camera that it is compared with. Additionally, details of the digital phantoms used and simulations performed are provided.

2.2.1   *MBT scanner design*

In the MBT scanner proposed in this paper, the patient lies prone on a specially designed bed (Figure 2-1(a)) that has an opening for the breast. To also allow imaging of breast tissue close to the chest wall, the pendant breast should hang as deep as possible in the adjustable slit formed by two L-shaped round-edged transparent Perspex plates underneath the bed (see Figure 2-2) (Beekman, 2011, 2014). These plates lightly compress the pendant breast. We assume similar levels of compression as reported for planar MBI (Hruska *et al.*, 2008)), which is much less than the compression used in mammography. This improves patient comfort, which is required as in radiotracer-based breast imaging patients typically will have to endure a 10 to 20 min scan. Some level of compression is preferred as it prevents motion during a scan and it reduces the thickness of the breast, which is beneficial for sensitivity, as the collimators can be placed closer to the breast's tissue.

The whole imaging set-up underneath the bed can be rotated (see Figure 2-1(b)) between scans. Thus, it allows for compressing the breast under similar view angles and breast deformation as used in X-ray mammography and planar MBI, i.e. the craniocaudal (CC) view and the mediolateral oblique (MLO) view. By summing the acquired 3D images along the appropriate direction, comparable 2D images can be generated. Consecutive image acquisitions for different orientations of course require re-compressing the breast in another position, as one also has to do for planar MBI or mammography. A prototype patient bed was evaluated with a group of 10 women, and, no problems with placing of the shoulders and arms were found, as their position was the same for MLO compression as for CC compression.

Although this paper focuses on breast imaging capabilities of MBT, an additional feature of this flexible setup is that it might also allow scanning of the armpit by having the patients lie on

Figure 2-1 Patient table and compression for the proposed MBT scanner. (a) A woman lying prone on the scanner table with one breast in the opening in the bed. (b) Schematic representation of the compression in the scanner. As shown, the breast can be imaged in different views analogous to the craniocaudal (CC) and mediolateral oblique (MLO) views in mammography. (c) The patient is laying on her side and fully extending her arm downward between the compression plates which allows for scanning the right armpit. (d) Schematic representation of imaging the armpit.

their side and move their arm downwards, see Figure 2-1 (c & d). However, the capabilities for the latter application would have to be investigated during a separate study.

Optical cameras view the compressed breast through the transparent compression plates (see Figure 2-2(a)). With a graphical user interface, the user can then designate the volume to be scanned, which can e.g. be the whole breast, a suspected region, or a known tumour. Targeted imaging based on scan planning with optical cameras is already in use in preclinical SPECT and it has been shown that focusing on a VOI leads to increased count yields from the VOI (Branderhorst *et al.*, 2011). This can result in improved contrast-to-noise trade-offs or offer the possibility of reduced acquisition time or lower tracer dose.

After volume selection, two collimator-detector combinations, which are positioned below the patient bed, move into the scanning position (Figure 2-2(b)). During scanning, these gamma detectors and collimators translate and in this way acquire gamma-ray projections of the com-
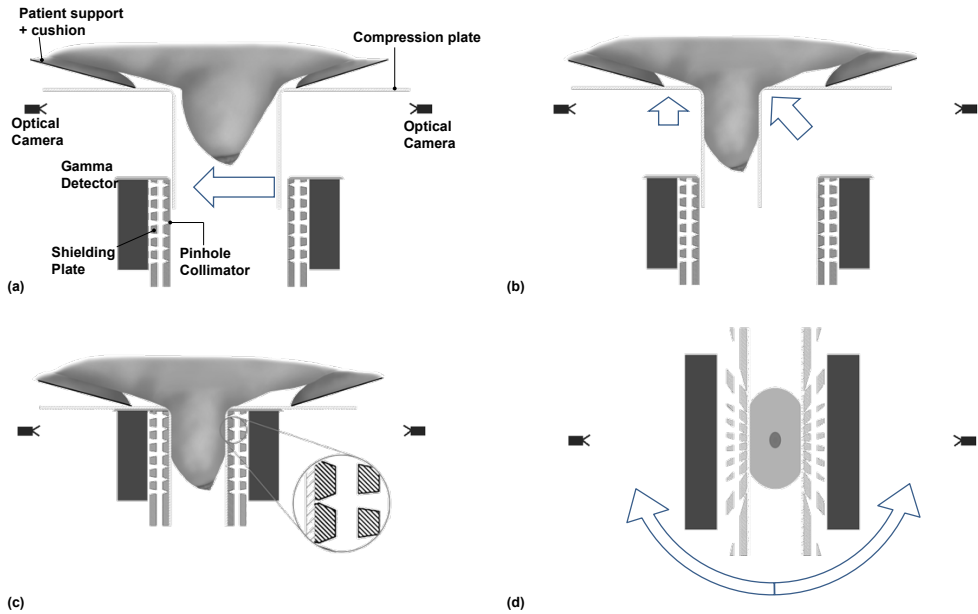
Figure 2-2 The compression process and scanner geometry: (a) Transparent plates compress the breast (artist impression) and a VOI is selected using optical cameras. (b) After scan volume selection, the collimator plates and gamma detectors move into scanning position (arrows). (c) Collimator and gamma detector in scanning position, with inset showing collimator detail. (d) Perpendicular cross-section through collimator-gamma detector set-up showing the pinhole geometry. Dashed lines indicate the pinhole axes, which converge on a line 40 mm from the collimator. Arrows indicate rotation of whole scanner-head to enable different views.

pressed breast in different positions. Collimator and gamma detector designs are described below as well as the sequence of positions used.

2.2.1.1 MBT multi-pinhole collimator.

Collimation of the gamma photons emitted by the tracer is achieved by using two 10 mm thick tungsten collimator plates each containing 63 pinholes that all "see" part of the breast and project onto one of the two gamma detectors which are placed 3.6 cm from the compression plates (12 mm thickness) (see Figure 2-2(c & d)). The pinhole axes in each collimator plate are directed towards a focus line 40 mm from the collimator face; see Figure 2-2(d) in which pinhole axes are drawn for one of the collimator plates. The knife-edge pinholes have a diameter of 2.7 mm and an opening angle of 42 degrees. Overlapping projections on the gamma camera can cause image artefacts, e.g. Vunckx *et al.* (2008); Mok *et al.* (2009). Therefore, projections from different pinholes are prevented from overlapping by a tungsten shielding plate, which is placed in between the collimator and detector, similar to the shielding tube introduced in Beekman *et al.* (2005). This shielding plate contains rectangular holes and has a thickness of 12 mm. The pinholes and the corresponding holes in the shielding plate are positioned such that the projections on the detector from different pinholes are adjacent with a 3 mm separation between them. The distance
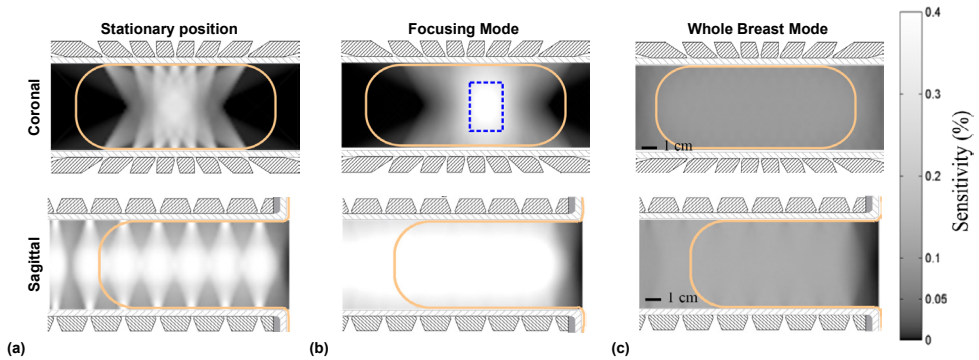
Figure 2-3 Maps of the sensitivity in the FOV of the system. Top row represents sensitivity in a cross section along the coronal plane, bottom row along the sagittal plane. Maps represent (a) a single stationary collimator position, (b) the Focusing Mode and (c) the Whole Breast Mode. Solid orange contour lines indicate the size of an average breast, blue dashed rectangle is the area for which sensitivity in the Focusing Mode is reported in section 2.3.

between the pinholes in the sagittal view (Figure 2-3) is 23.9 mm, while in the coronal view the distance varies from 13.3 to 38 mm. The combined thickness of collimator and shielding plate provides sufficient stopping power for imaging tracers based on ^{99m}Tc and 123I (e.g., for ^{99m}Tc a fraction of 6.10-33 is transmitted).

Tomographic imaging requires sufficient angular sampling of the data to be able to guarantee good reconstructions. In breast imaging, it is very hard to simultaneously obtain complete sampling and place the collimator close to the breast, the latter being highly desirable for obtaining high sensitivities with pinhole collimators and high resolutions with pinhole and parallel hole collimators. In our system, the arrangement of the pinholes in two collimator plates means that the pinholes do not cover a full 180-degree range, as is required for data completeness (Orlov, 1975; Tuy, 1983). Consequently, we expect the resolution parallel to our detectors to be higher than the resolution in the perpendicular direction. This resembles the way X-ray tomosynthesis adds 3D information to mammography, without achieving the full 3D capability of X-ray Computed Tomography. Therefore, we use the term molecular breast tomosynthesis (MBT) to describe our scanner, instead of breast SPECT.

2.2.1.2 MBT Detector.
In this simulation study, we evaluated the use of a conventional PMT-based scintillation detector employing a continuous NaI(Tl) crystal. In contrast, cadmium zinc telluride (CZT) detectors are often selected for planar MBI because they can provide better spatial and energy resolutions than continuous NaI(Tl) coupled to an array of PMTs. However, compared to planar MBI, system resolution in a pinhole-geometry such as used in MBT is not limited by the intrinsic detector resolution because pinholes can generate magnified projections of the activity distribution on the detector. Thus, image resolutions far better than the detector resolution can be obtained; e.g. small-animal systems can obtain 0.25 mm image resolution using conventional detectors with

only 3.2 mm intrinsic detector resolution (Ivashchenko *et al.*, 2014). Standard available CZT detectors offer lower detection efficiency than NaI(Tl) and initial calculations of system resolution and sensitivity of different MBT designs with CZT or NaI(Tl) detectors have shown that for the MBT design proposed here the higher spatial resolution of CZT detector does not outweigh the loss in efficiency (van Roosmalen *et al.*, 2015). The higher energy resolution of CZT compared to NaI(Tl) can be advantageous for scatter rejection although some studies indicate that scatter might not be a significant issue for this type of geometry as we discuss in more detail in section 2.2.5.1. As a conventional PMT-based NaI(Tl) gamma detector is also available at much lower costs than CZT detectors, we prefer this type of detector for our design.

For our detectors, we assumed an active area of 25x15 cm2 and a scintillator thickness of 9.5 mm for each detector, which is read out by an array of 2-inch PMTs. For breast imaging, it is important and challenging to image also breast tissue close to the chest wall. This sets strong requirements on the allowed dead area near the detector's edge. Barrett *et al.* (2009) have used Maximum Likelihood processing of the PMT signals (Milster *et al.*, 1990; Moore *et al.*, 2007; Barrett *et al.*, 2009), instead of standard Anger logic. They showed that it is possible to reduce dead edge effects for NaI(Tl) detector. Based on their results, we assume a total dead edge of 5 mm, which includes shielding/housing of the crystal. An intrinsic detector resolution of 3.2 mm was assumed which can be attained with Anger logic already. The detector efficiency was assumed to be 90%, corresponding to the stopping power of 9.5 mm NaI(Tl) for 140 keV gamma photons (^{99m}Tc).

2.2.2   *Movement and scanning modes*

The focused collimator design presented here provides users of the MBT scanner with the unique ability of having the freedom to perform different scans by focusing on a volume of choice. Focusing on a VOI is beneficial because this way the count yield from the VOI can be increased (Branderhorst *et al.*, 2011). The slices shown in Figure 2-3(a) illustrate which part of the breast is "seen" by the pinholes when detectors and collimators are in a single stationary position. To image a user-selected volume, the field-of-view (FOV) has to be translated over the breast such that the whole scan volume is viewed over a range of angles (Vastenhouw and Beekman, 2007; Vaissier *et al.*, 2012). This FOV translation is done by synchronized step-and-shoot movement of the collimators and detectors. The sagittal slice in Figure 2-3(a) shows that the FOV contains areas with low sensitivity in between the pinholes. Therefore, the collimators and detectors always have to move in the anterior direction to cover these gaps. The amount of movement depends on breast size but is independent of the size of the VOI. Additionally, collimators and detectors move to the left and to the right (from the patient's reference frame), parallel to the breast. The sequence of steps in horizontal direction depends on the selected VOI. The goal is to design a scan sequence that optimizes count yield from the VOI while simultaneously obtaining a reasonably uniform sensitivity in the whole VOI. The specific scan sequences used in this paper are provided below in section 2.2.5.2 that describes the phantom experiments.

The movement of collimators and detectors does not only increase the size of the FOV, but also increases the number of angles that sample a point in the FOV. We take all available information into account, as the projection data from all positions is used simultaneously for reconstruction, instead of stitching local reconstructions (Vastenhouw and Beekman, 2007).

To compare how different types of scans perform, we will test two different scan modes in this paper. First, the Whole Breast Mode is e.g. for the situation in which the presence of lesions or their location is not known and the whole breast has to be scanned to search for them. Secondly, a Focusing Mode scan sequence in which one focuses on a smaller region of the breast containing tumours is evaluated. Such a scan may be performed when it is expected that a tumour is present at a certain location and one wants to obtain as detailed as possible its characteristics, e.g. exact shape, activity uptake, etc.

2.2.3 Planar MBI system

We compare performance of our dedicated MBT scanner with planar MBI. A geometry based on the planar MBI scanner developed by Hruska *et al.* (2012a; 2012b) is simulated in this paper. We selected this system as our benchmark, as it has had considerable development and optimisation, thereby making it a good reference for what is currently possible with planar MBI. Furthermore, this system can be used with a similar compression of the breast as our design, allowing for a relatively straightforward comparison.

The simulated planar MBI system employs a pixelated CZT detector of 20 x 16 cm^2 with 1.6 mm pixels. The tungsten parallel hole collimator is registered to this detector, meaning that each hole of the collimator corresponds to exactly one detector pixel. The square holes have a length of 9.4 mm, a side-length of 1.225 mm and the septal thickness is 0.375 mm.

2.2.4 Phantom scans

We evaluated the systems' performance on two different phantoms. First, a resolution phantom is used to assess the smallest details that can be resolved. Second, we show simulated images of an anthropomorphic breast shaped phantom containing several lesions to evaluate characteristics for tumour imaging.

2.2.4.1 Resolution phantom.

To determine resolution of MBT, a Derenzo resolution phantom was simulated. The phantom had 6 sectors with rods of 2.0, 2.5, 3.0, 3.5, 4.0, and 4.5 mm diameter (see Figure 2-5(a)). The distance between rods was twice the rod diameter, and the length was 40 mm. The rods contained an activity concentration of 37 kBq/ml. We did not assume any activity in the background, but did incorporate attenuation in a breast shaped region (see below for the breast phantom). A linear attenuation coefficient of 0.0151 mm-1 was assumed which is valid for 140 keV photons in water.

We performed two different simulations, both of 10 min scans but with different phantom orientations. In the first simulated scan, the phantom was placed such that the rods are perpen-
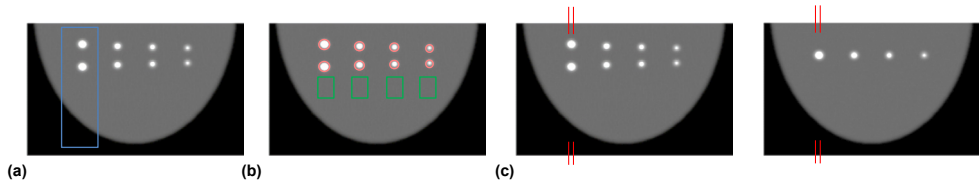
Figure 2-4 Slices through the breast phantom with regions used in analysis indicated. (a) Region used in Focusing Mode for imaging largest spheres. (b) Red circles are regions for contrast and CNR calculation, green box is background region for the same. (c) Lines indicate location of profiles shown in Figure 2-8.

dicular to the transverse plane. The second scan had the rods in a direction perpendicular to the coronal plane. These positions were chosen to determine resolution both in the plane parallel to the detectors as in the plane perpendicular to them (i.e., how accurate is the depth information). We sampled the phantom on a 0.375 mm voxel grid to simulate projections. For MBT we reconstructed the phantom on a 0.75 mm grid using 20 iterations of MLEM as explained below. Note that for planar MBI the projections are used directly and no reconstruction is required. The images are shown unfiltered.

2.2.4.2 Breast phantom.

As our set-up uses moderate compression of the breast, the breast can be modelled quite well as half an elliptically shaped disk (Dong *et al.*, 2011). Approximating an averagely sized breast, a 110 mm chest-to-nipple distance, a width of 150 mm, and a thickness of 55 mm were set in accordance with results from other breast scans with similar compression (Scopinaro *et al.*, 1999; Rhodes *et al.*, 2005; O'Connor *et al.*, 2007; Hruska *et al.*, 2008; O'Connor *et al.*, 2008; Weinmann *et al.*, 2009), and slightly thicker then often found in mammography literature, in which much more compression is used (Sullivan *et al.*, 1991; Helvie *et al.*, 1994).

To assess how differently sized lesions are imaged, we placed four sets with three lesions each in the phantom. Each set has different lesion sizes (4.0, 4.5, 5.0 and 6.0 mm), see Figure 2-4, which shows 2 slices through the phantom. Within each set, the central lesion was placed at a depth of 22 mm, with the other two lesions at a depth of 33 mm, making a triangular arrangement. This is done to test the ability of MBT to differentiate between lesions at different depths. The phantom was sampled on a 0.75 mm voxel grid (and reconstructed on 1.5 mm grid for MBT as explained below).

We assumed a background activity concentration of 3.7 kBq/mL, consistent with an injection of 925 MBq ^{99m}Tc-Sestamibi as experimentally determined by Mann *et al.* (2012) and consistent with count levels from Hruska *et al.* (2012a). We assume a concentration of 37 kBq/ml in the lesions to give an tumour-background uptake ratio of 10:1, as found in common practise (Maublant *et al.*, 1996; Lee *et al.*, 2004; Hruska and O'Connor, 2008; Sullivan *et al.*, 2012). Again, we simulated 10-minute acquisition time.

2.2.5   Simulations and image reconstruction

In this subsection, we describe the simulation methods used, for both MBT and planar MBI, as well as the way of analysing the results.

2.2.5.1   MBT.

To simulate images that can be obtained by MBT, we developed a ray tracing simulator (**Chapter 3**) that calculates the probability that a gamma photon emitted from a certain volume element (voxel) in the breast is detected in a certain detector pixel. This simulator uses the collimator modelled as a voxelized volume (with a voxel size of 0.0625 mm) as its input, where each voxel contains either air or tungsten. The ray tracer calculates the collimator attenuation by determining the amount of collimator material encountered by a gamma photon for each voxel-pixel combination. A threshold was used to ignore small contributions (gamma photons that had a chance of less than the threshold to pass through the collimator were ignored). The depth-of-interaction in the scintillator crystal is modelled by also raytracing the gamma photon through the scintillator, similarly as was described in (Goorden *et al.*, 2016). Consequently, the detector efficiency of 90% is automatically taken into account. The intrinsic detector resolution was incorporated by modelling detector response with a 3.2 mm FWHM Gaussian. We assumed detector pixels of 1.072 mm in a 234x140-pixel grid.

To calculate phantom projections, we represented the phantoms on a regular voxel grid (voxel size was mentioned for each phantom in section 2.2.4). With the raytracer set to a threshold of 1%, we generated simulated projections from the phantoms for each of the positions in the scan sequence. Hereby, we accounted for the activity concentration in the phantom and the scanning time in each position. Moreover, the attenuation in the phantom was modelled using a uniform attenuation coefficient of 0.0151 mm-1 valid for 140 keV photons in water. Poisson distributed noise was added to each projection to take into account counting statistics. As mentioned in section 2.2.1.2, earlier phantom studies for a similar geometry showed that scatter from the torso is not a significant problem (Wang *et al.*, 1996; Hruska and O'Connor, 2006). This is because gamma photons coming from the torso can only end up on the detector if they scatter over a large angle. As large-angle scattering is associated with a relatively large energy loss, the scattered photons can be identified relatively easy with energy selection. To validate if this was indeed the case for our proposed geometry, we performed simulations with the well-known Monte Carlo package GATE (Jan *et al.*, 2004; Jan *et al.*, 2011) using the realistic MCAT phantom (Segars and Tsui, 2009; Segars *et al.*, 2010) and activity concentrations found in literature (Wackers *et al.*, 1989; Wang *et al.*, 1996; Hruska and Connor, 2008; Perez *et al.*, 2010). These simulations (Wang *et al.*, 2016) predict that the scatter fraction from the heart and torso in the photopeak (assuming 10% energy resolution and a photopeak window width of 20%) is less than 1.5%, in agreement with the experimental results from (Wang *et al.*, 1996; Hruska and O'Connor, 2006). Therefore, the use of a raytracer that models attenuation but ignores scatter is justified for this geometry.

For the tomographic reconstruction of the projection data, we used the Maximum Likelihood Expectation Maximization (MLEM) algorithm. The system matrix used in MLEM was calculated

with the same ray tracer as used for the projections but with a threshold of 2% (of the not-attenuated probability of detection) and at a two times courser voxel size than that used to calculate projections. The discrepancy in voxel size and cut off thresholds between phantom projections and system matrix is to mimic a continuous activity distribution without having an actual threshold on gamma photon transport. We did not use a subset-based acceleration scheme because we found that the lack of complete angular sampling resulted in artefacts even for a small number of subsets. Moreover, we did not use attenuation correction, as the method for obtaining highly accurate information of the breast contour is not yet established. With these settings, a single MLEM iteration takes about 5 minutes using 6 threads on a AMD Opteron 6344 at 2.6 GHz.

2.2.5.2   Scan Sequences for MBT.
As explained in section 2.2.2, the choice of scan sequence can significantly impact reconstructed images. The sequences used for this study were optimized to yield a uniform sensitivity over the scan area. This was done by translating the sensitivity map from Figure 2-3 (a) according to each scan position in the sequence and then calculating an average sensitivity over all scan positions. This results in an estimated sensitivity map for the scan sequence as a whole. In general, increasing the number of steps and thereby reducing the distance between the steps improves the uniformity. Several scan sequences with different amounts of positions were tested. We chose a sequence with the requirement that the 1st percentile of voxels had a sensitivity of at least 10% of the mean sensitivity. From all sequences that fulfilled this requirement, we chose the one that used the lowest amount of positions. The sensitivity of the 1st percentile was used as metric instead of e.g. the standard deviation as even small areas with very low sensitivity can cause image artefacts without showing in the standard deviation of the sensitivity if the rest is smooth enough. Moreover, our software currently requires the step-size to be an integer multiple of the voxel size used during reconstruction.

We evaluate the use of two different sequences, a Whole Breast Mode and a Focusing Mode. For both modes, we use the same number of steps in the anterior direction. Given the averagely sized breast assumed in this paper (see subsection 2.2.4.2), the movement in the anterior direction is done in 10 overlapping steps. The positions for each of these steps are 0.0, 1.5, 4.5, 6.0, 9.0, 10.5, 13.5, 15.0, 18.0 and 19.5 mm, where 0.0 denotes the initial position, which is as close as possible to the chest.

For the left-right movement in Whole Breast Mode, we use a slightly different set of positions for each alternating row (i.e. steps in the anterior direction). This helps to get a uniform coverage of the breast, while keeping the number of positions low, which reduces the overhead time associated with each movement. The positions are

$$\begin{cases} -75, -66, -57, -48, -39, -30, -21, -12, -3, 6, 15, 24, 33, 42, 51, 60, \text{ and } 69 \text{ mm}, & \text{for even rows,} \\ -69, -60, -51, -42, -33, -24, -15, -6, 3, 12, 21, 30, 39, 48, 57, 66, \text{ and } 75 \text{ mm}, & \text{for odd rows,} \end{cases}$$

with 0 denoting the position with the collimator centred over the breast. In Focusing Mode, the

horizontal movement of collimator and detector is given with respect to the centre of the VOI. For the VOI setting used in our simulations (see Figure 2-4(a) and section 2.2.4.2), the positions are given by -9.0, -6.0, -3.0, -1.5, 1.5, 3.0, 6.0, and 9.0 mm.

Data from the resolution phantom was acquired with the Whole Breast Mode, while for the breast phantom both modes were tested.

2.2.5.3 Planar MBI.

We simulated the planar MBI system using the same ray tracing software as used for the MBT scanner. The voxelized collimator model (with 0.025 mm voxels) used in this software was carefully aligned with the detector to match the holes to the detector pixels. We did not assume detector blurring, as the simulated system uses a pixelated detector design. The planar scanner directly produces an image instead of projections that serve as input to a reconstruction algorithm. Therefore, we only calculate a single forward projection and add Poisson noise to it. We assumed two detectors, one on each side of the breast. We then show the geometrical mean of the two images from the opposite detectors, as this has been shown to give the best results (Judy *et al.*, 2010).

2.2.6 Analysis of images

Besides visually inspecting different images, we compared different breast phantom images by calculating the contrast C of the lesion with respect to the background

$$C = \frac{\bar{S} - \bar{B}}{\bar{B}} \tag{2-1}$$

We also determined the contrast-to-noise ratio CNR given by

$$CNR = \frac{\bar{S} - \bar{B}}{\sigma_B} \tag{2-2}$$

In these equations $\bar{S}$ is the average voxel value taken in a circular region with the same diameter as the lesion placed on top of the lesion, $\bar{B}$ is the average signal in a background region, and σ_B is the standard deviation in the background region and serves as measure of the noise. The regions used are shown in Figure 2-4(b).

To get a measure of how contrast varies over different noise realizations, we simulated 20 noise realizations. For reconstructed images such as obtained with MBT, contrast and noise both depend on the number of iterations used and the post-filtering applied while planar MBI images are only affected by the level of post-filtering. We choose to use a constant number of 20 iterations for MBT, and investigate the contrast-to-noise trade-off by applying a progressive series of Gaussian filters (with FWHM from 0 to 10 mm in steps of 1 mm) both for planar MBI and MBT. For each noise realisation, the contrast and noise were determined, and the average of the contrast over the noise realisations was plotted in a contrast versus noise graph.
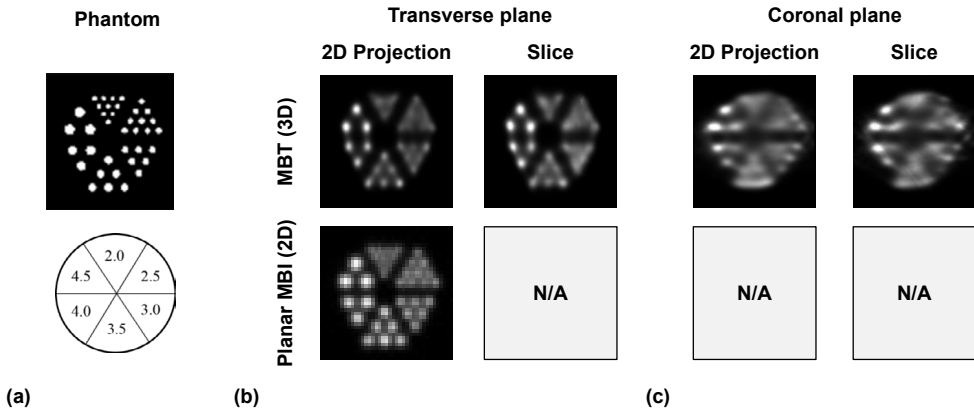
Figure 2-5 Images of capillary Derenzo resolution phantom. (a) Capillary Derenzo resolution phantom with 40 mm length rods having diameters of 2.0, 2.5, 3.0, 3.5, 4.0 and 4.5 mm. (b) Simulation results for said phantom, where top row is for the MBT system and bottom row is image for planar MBI. First column shows sum of the reconstructed slices (for MBT and planar MBI), second column shows a slice (only for MBT) through the reconstruction. (c) Similar images as in (b) are shown but now for the phantom placed in the coronal plane. Note that planar MBI cannot provide an image in this plane, due to lack of depth information. Slice thickness was 5 mm.
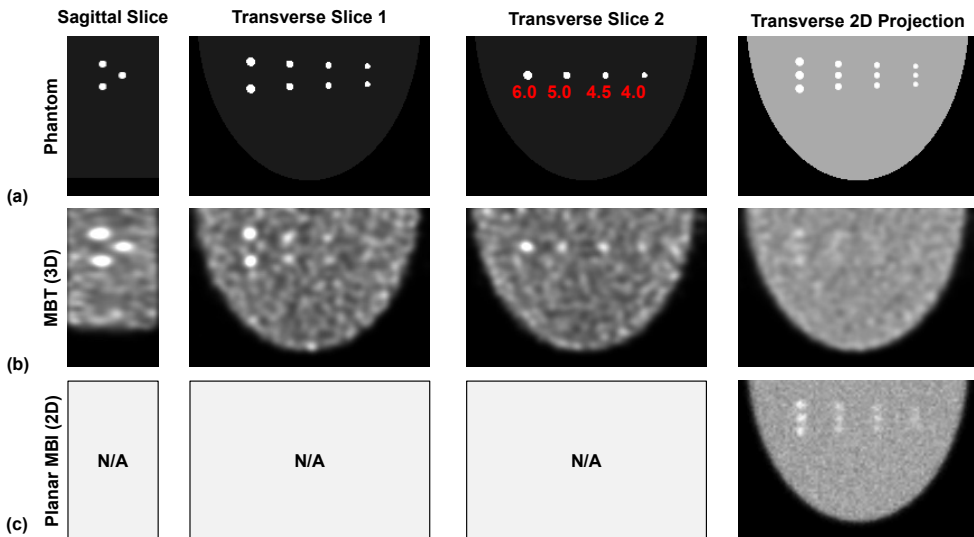
Figure 2-6 Simulated images of breast shaped phantom containing lesions of 4.0, 4.5, 5.0 and 6.0 mm. (a) Phantom images with from left to right: slice parallel to sagittal plane through the lesions, transverse slice at depth of two lesions, transverse slice at depth of third lesion, sum of transverse slices for comparison with planar MBI; All slices are 1.5 mm thick. (b) MBT images in the same representation as in (a), and shown using 4.0 mm FWHM Gaussian filter to match noise in 2D projection to planar MBI. (c) Unfiltered planar MBI image, representing a geometrical mean of two detector imag-es placed at either side of the breast.

As stated in section 2.3.3, MBT images shown were post-filtered with a 4.0 mm FWHM Gaussian filter. This filter was chosen as it resulted in the same noise level as the planar MBI images that we displayed.

2.3   Results

2.3.1   Sensitivity maps and scan sequences

In Figure 2-3(a), we provide a map representing the sensitivity of MBT in sagittal and transverse slices through the breast for one stationary collimator-detector position. The sensitivity map clearly reveals a pattern representing the FOVs of individual pinholes. By moving the collimators and detectors, this pattern is averaged out. Moreover, regions of decreased sensitivity in the FOV of one collimator are sampled by the opposite collimator, although with a relatively low sensitivity. In Figure 2-3(b) and (c), we show the resulting average sensitivity for the Focusing Mode and the Whole Breast Mode scan sequences tested in this paper. In the Whole Breast Mode, the complete breast is imaged with an almost uniform sensitivity of 0.05%. The Focusing Mode has 4.1 times higher average sensitivity compared to the Whole Breast Mode in the VOI indicated by the blue dashed box in Figure 2-3(b).

2.3.2   Resolution phantom

Simulated images of the Derenzo resolution phantom are shown in Figure 2-5. A 2D projection is shown both for MBT (by summing reconstructed slices) and for planar MBI while a slice through the phantom is provided for MBT. For the first scan, the phantom was placed in the transverse plane (i.e. parallel to the collimator plates). With the phantom oriented this way, MBT could resolve 3.0 mm rods (see Figure 2-5(b)) while the planar breast imaging system resolved the 2.5 mm and larger rods (see Figure 2-5(b)).

The phantom was then placed in the coronal plane, for a second scan simulation. From the images, it is clear that MBT can still distinguish the 4.0 mm rods (see Figure 2-5(c)), although we see attenuation artefacts in the centre of the figure. Given the geometry of the collimator (i.e. the limited angular sampling), it was expected to find a poorer depth resolution than the 3.0 mm resolution obtained in the transverse plane. Note that planar MBI systems cannot provide imaging in the depth direction, so one would only be able to get a side view of the phantom.

2.3.3   Breast shaped phantom

For the breast phantom, simulated images for 10-minute scans are provided in Figure 2-6. In Figure 2-6(a), a sagittal slice through the phantom, 2 transverse slices (at the depth of the lesions), and the transverse sum are shown (representing a 2D projection of the breast). Corresponding slices and transverse 2D projection obtained with MBT can be found in Figure 2-6(b). For MBT, we used the Whole Breast Mode sequence for obtaining data. Due to its planar nature, MBI can only provide a 2D projection, which is shown in Figure 2-6(c).
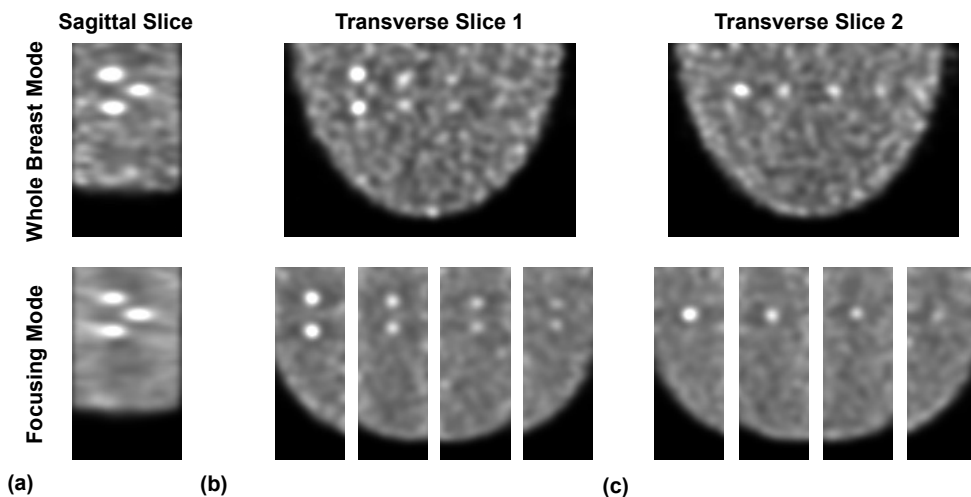
Figure 2-7 Comparison of Whole Breast Mode and Focusing Mode of MBT for same digital breast phantom as in Figure 2-6(a). Slices through reconstructed images are shown in (a) sagittal plane and in (b, c) transverse plane at 2 different depths.

In the 2D projections of the breast obtained with MBT and planar MBI, tumours at different depths appear to have equally strong tracer uptake, which immediately shows the limitation of planar imaging; the difference in depth of the tumours cannot be inferred from a planar scan. All MBT images in Figure 2-6 were filtered with a 3D Gaussian filter with a FWHM of 4.0 mm, resulting in the same noise level as planar MBI for the 2D projections (as explained below). As MBT provides a full 3D reconstruction of the tracer's biodistribution, it allows extracting more information than just a 2D projection. This advantage is clearly illustrated by the slices taken at various depths in the breast phantom and shown in Figure 2-6(b). The slices show that not all three lesions are at the same depth.

A unique property of MBT is the ability to select a patient-dependent scan volume. To analyse the advantage of focusing on a region with known tumours, we also imaged the same phantom with the scan sequence in which we focused on a set of tumours (the Focusing Mode, VOI is shown in Figure 2-4 (a)). Such a focused scan was repeated for each set of tumours in the phantom. In Figure 2-7, we compare images obtained in the Focusing Mode to those acquired in the Whole Breast Mode. Figure 2-7(a) shows a sagittal slice through the centre of the breast while transverse slices through the tumours are provided in Figure 2-7 (b &c).

Profiles through the centre of the 6.0 mm lesions acquired from different images are compared in Figure 2-8 (locations of the profiles are indicated in Figure 2-4 (c)). Figure 2-8(a) compares profiles obtained from 2D projections from MBT (both modes) and planar MBI. From these we see that planar MBI has the highest contrast, but that in the background region the focusing mode results in a smoother profile, i.e. is less noisy than planar MBI and MBT Whole Breast Mode.
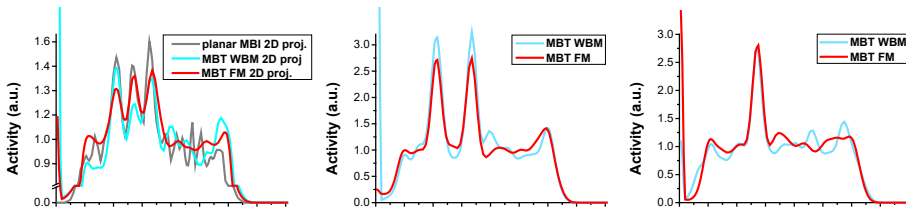
Figure 2-8 Profiles (1.5 mm wide) through centre of the 6.0 mm lesions obtained from different images. (a) Profiles through transverse 2D projections (Figure 2-6(b & c) and Figure 2-7) of planar MBI, MBT Whole Breast Mode (WBM) and MBT Focusing Mode (FM). (b) Profiles through transverse slices at 2 different depths comparing MBT in Whole Breast Mode and in Focusing Mode, from Figure 2-7(b, c)
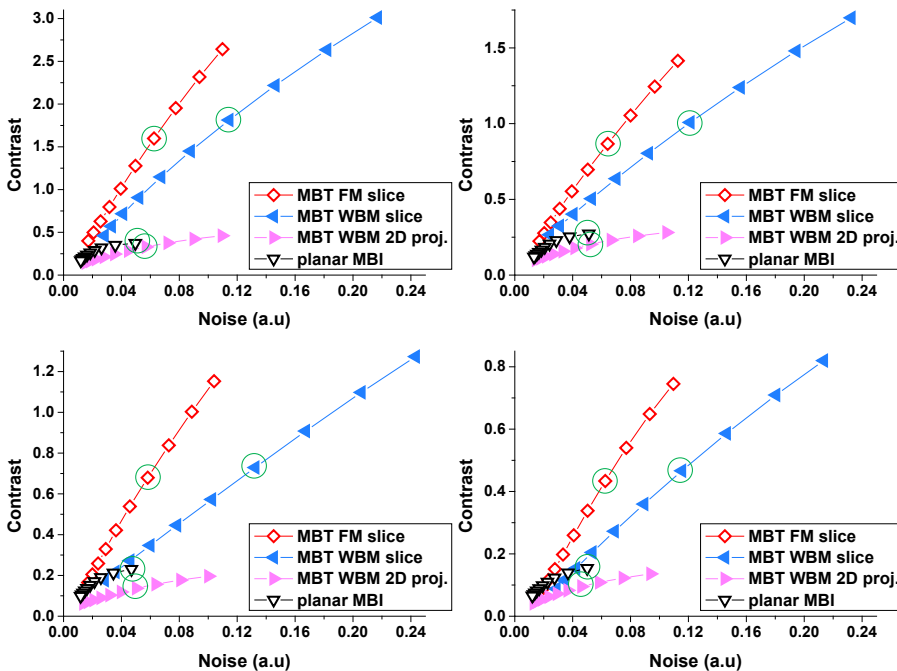
Figure 2-9 A plot of (a) contrast vs noise for 6.0 mm lesion, points represent different FWHM (range 0.0 to 10 mm, steps 1mm) of the Gaussian filter. The same contrast-noise plot as in (a) but for (b) 5.0 mm lesion, (c) 4.5 mm lesion, (d) 4.0 mm lesion. The green circles indicate the filter level used in the comparisons in Table 2-1, and plotted images.

Figure 2-8(b) shows profiles acquired from the MBT slices in Figure 2-7. These profiles show that the availability of different slices does not only allow to obtain depth information but also allows to obtain much better tumour-to-background contrast; in profiles of Figure 2-8(b) tumour signals rise much more above the background than in Figure 2-8(a). From the comparison of profiles from Whole Breast Mode and Focusing Mode in Figure 2-8(b), one can infer that

the Focusing Mode gives a slightly lower contrast as the Whole Breast Mode, but with a much smoother background, which may ease identification of anomalies.

A more quantitative contrast-to-noise analysis was done for all tumour sizes. In Figure 2-9, the contrast of tumours over the background obtained from different images is plotted against the background noise for each lesion size. Different points in the graph represent a series of progressively more Gaussian filtering. This way, the contrast-noise trade-off can be tuned, and the different contrasts can be compared at equal noise levels. We provide contrast and noise obtained from planar MBI images (Figure 2-6 (c)), summed 2D projection images (Figure 2-6(b)) and from slices acquired with MBT (Figure 2-6 and Figure 2-7). This allows analysing if 3D imaging not only offers better tumour localization, but also improves contrast-noise characteristics for tumour scanning.

We see in Figure 2-9, that the line representing the 2D projection for MBT is somewhat below that of planar MBI, i.e. the contrast is lower at an equal noise level as is also clear from the images in Figure 2-6. This changes when tumour-to-background contrast is determined from slices; in that case MBT in Whole Breast Mode has a slightly higher contrast (at equal noise) than planar MBI, while in Focusing Mode the contrast improvement is much larger (typically a factor 2 over planar MBI).

To get an impression of the results that could be obtained for a lower dose, the contrast-noise analysis shown in Figure 2-9 and Table 2-1 were repeated using only 1/4th of the dose used in the paper. Figure A-2 and Table A-1 in the supplementary information[1], which display analogous results to Figure 2-9 and Table 2-1, show that while the CNR is reduced for lower doses both for MBI and MBT the relative performance of MBI and MBT remains similar.

As mentioned above, for the MBT images shown in Figure 2-6 and Figure 2-7, a 4.0 mm FWHM Gaussian was used as the noise in the 2D projections is then close to the noise in unfiltered planar MBI images. Contrast-noise for these filter settings is indicated with the circles in Figure 2-9 and the contrast and CNR are provided in Table 2-1. From the values in this table, it can be seen that if a transverse sum (2D projection) is generated from MBT images in Whole Breast Mode, MBT achieves a 12-40% lower contrast as planar MBI at equal noise level. However, using slices through reconstructed MBT images can significantly enhance the tumour-to-background contrast, e.g. on average (over all lesions) MBT in Whole Breast Mode has 268% better contrast than the planar MBI image, see Table 2-1. This corresponds with the large contrast improvements shown in the profiles of Figure 2-8. Note that the same amount of activity and equal scan time was used for both planar MBI and for MBT.

While the level of filtering used for the images in Figure 2-6 and Figure 2-7, and for the results in Table 2-1, was chosen such that the noise level is equal in 2D projections, slices from the

---

1   The supplementary information is provided with the published paper on which this chapter is based and can be accessed at http://stacks.iop.org/PMB/61/5508/mmedia

MBT reconstructions have different levels of noise than the 2D projections. Therefore, we also provide CNR in Table 2-1. Overall, the slices from MBT provide a significantly higher CNR than planar MBI. In terms of CNR, MBT in Whole Breast Mode performs ~72% better than planar MBI for the larger 5.0 and 6.0 mm lesions, and has no improvement for the smallest 4.0 mm lesions. Here, the use of MBT in Focusing Mode has a very clear advantage as it can significantly improve CNR, with an increase ranging from 92% for the smallest lesion to 241% for the largest lesion compared to planar MBI.

2.4   Discussion

In simulations, we compared MBT to planar MBI. For breast tumour imaging, we found that MBT in Whole Breast Mode has up to 111% higher CNR, while a Focusing Mode achieved up to 241% higher CNR than planar MBI. This large improvement of the contrast-to-noise ratio achieved by focusing on a region containing tumours can be explained by the extra sensitivity it provides in the VOI (see Figure 2-3(b)) which leads to a reduction in the noise while maintaining the contrast. Besides improving tumour CNR over planar MBI, MBT provides information about the depth of a lesion, information that by definition is not available in planar images. Moreover, it may help to better estimate shape and size of the lesion, which is important for determining its possible malignancy. Further evaluation of different imaging scenarios could be of interest for future research.

For this study, we showed MBT images for which the number of MLEM iterations and the Gaussian post filter were tuned such that in the Whole Breast Mode 2D projections (obtained by summing slices from the reconstructed image) have a similar noise level as the planar MBI images. This allows for a comparison between contrast for MBT and planar MBI at the same noise level. Further research will be needed to determine a practical stopping criterion and filter settings for a real patient scanner.

Planar MBI has seen many improvements over the past few years. For the comparison with MBT in this paper, we simulated one of the most recent and best performing system geometries. Although we believe that first results are very promising, this study is only a first introduction of MBT based on multiple pinholes. Even in this stage, MBT already outperforms planar MBI in terms of CNR and depth information. We believe that MBT can certainly be improved with further research to optimize the design-parameters, such as the collimator-to-detector distance, pinhole-opening angles, amount of focusing etc. This could include optimizing the pinhole layout for scanning the chest wall area. Moreover, we work on ways to eliminate the dead edges of the detector, e.g. using side detectors (Salvador *et al.*, 2012). In addition, others have proposed ways to reduce dead edges, e.g. by using maximum likelihood processing, smaller PMTs, or PSPMTs etc. (Milster *et al.*, 1985; Milster *et al.*, 1990; Moore *et al.*, 2007; Barrett *et al.*, 2009).

Furthermore, future research could include investigating alternative collimators (e.g., fan beam collimators), or different detectors, such as CZT detectors which are already successfully applied

Table 2-1 List of contrasts and contrast-to-noise ratios (CNR) obtained for unfiltered planar MBI and images from MBT filtered with 4.0 mm Gaussian (images shown in Figure 2-6 and Figure 2-7), resulting in equal noise for 2D projections.

Lesion diameter (mm)	Planar MBI 2D projection		MBT 2D projection WBM		MBT Slice WBM		MBT Slice FM	
	Contrast	CNR	Contrast	CNR	Contrast	CNR	Contrast	CNR
4.0	0.16 ± 33%	3.6 ± 54%	0.10 ± 58% (-39%)	2.1 ± 65% (-42%)	0.47 ± 51% (+201%)	4.0 ± 57% (+12%)	0.43 ± 19% (+180%)	6.9 ± 28% (+92%)
4.5	0.23 ± 15%	5.7 ± 43%	0.14 ± 40% (-40%)	2.7 ± 46% (-52%)	0.73 ± 36% (+218%)	5.5 ± 44% (-3%)	0.68 ± 18% (+196%)	11.7 ± 29% (+105%)
5.0	0.27 ± 13%	6.3 ± 43%	0.20 ± 27% (-25%)	3.9 ± 34% (-38%)	1.01 ± 24% (+268%)	8.3 ± 35% (+33%)	0.87 ± 12% (+217%)	13.5 ± 23% (+115%)
6.0	0.37 ± 8%	7.5 ± 15%	0.33 ± 17% (-12%)	5.8 ± 32% (-23%)	1.81 ± 16% (+386%)	15.8 ± 33% (+111%)	1.60 ± 8% (+328%)	25.6 ± 32% (+241%)

Note: For all numbers the standard deviation over the 20 noise realizations is given. For MBT the difference in contrast and CNR with respect to planar MBI is indicated.

in planar MBI. Although a preliminary comparison showed limited benefit when using current CZT detectors, these types of detectors are under active development and may deserve further consideration in the near future.

Besides improving MBT's geometry, it might be valuable to investigate if the use of a prior in image reconstruction is beneficial, i.e. to use Maximum-A-Posteriori reconstruction instead of MLEM. This could improve uniformity in the background. However, the selection of an appropriate prior requires extensive research.

An important issue to be considered in molecular breast imaging is the dose administered to the patient. After the first introduction of MBI, extensive optimization studies have been conducted to allow for significant dose reduction. To give an indication of how MBT performs when dose is lowered, in the supplementary data we show how contrast and CNR are affected when only a quarter of the dose assumed in this paper is used. This indicates that MBT is not more severely affected by lowering the dose than MBI. In future work, we plan to study in more detail how performance of MBT is affected by dose and we will conduct optimization studies to optimize MBT's performance for lower dose, e.g. by tuning the resolution-sensitivity trade-off by the choice of pinhole diameter.

In this paper, we ignored the time needed for mechanical movement between positions. The mechanical design allows making the very short movements (6 mm) between positions faster than 0.1 s, resulting in a total dead time below 15 s. For a 10 min scan time, we think that the 2.5 % extra time needed is negligible. In addition, the dead time could be completely removed when acquisition would be performed in list mode.

Although the comparison of tumour imaging using CNR as a figure of merit favours MBT over planar MBI, this does not necessarily mean that MBT offers superior lesion detectability. Determining detectability is a complicated process influenced by many factors, such as the object and background statistics. The CNR is a measure for how strongly the reconstructed signal rises above the background and its fluctuations. This implies that a higher CNR makes it easier to detect whether the signal is present or not. In future research, we plan to investigate which figures of merit predict how well a system is able to detect tumours. Naturally, one could also consider a comparison based on determining and comparing receiver operating characteristic curves for planar MBI and MBT.

2.5   Conclusion

In this paper, we have presented a first MBT design based on multiple pinholes and evaluated its performance in a simulation study. From the simulated images, we conclude that our system attains a higher contrast-to-noise ratio for tumours than a planar imaging system. This might lead to better lesion detection and identification. Furthermore, the ability to recover depth information can be of great additional value.

In addition, MBT can focus on a suspected lesion or region. The focusing mode was shown to reduce background noise compared to whole breast imaging, while maintaining the contrast. This may improve lesion detection, but could also reduce the scan time while producing similar images as with whole breast imaging. We conclude that MBT might be a promising approach that can fill a niche in the breast-imaging field.

2.6   Acknowledgements

Chapter 3

Voxelized ray-tracing simulation dedicated to multi-pinhole molecular breast tomosynthesis

Abstract

Accurate gamma photon transport simulations of emission tomography systems are important to optimise system geometries and for iterative image reconstruction. Monte Carlo simulation (MCS) is widely established for this purpose but has the disadvantage of being prohibitively slow. Voxelized Ray Tracing (VRT) can be used as an alternative but the accuracy of VRT needs to be assessed for each simulation task at hand. The aim of this work is to propose and validate dedicated VRT code for a novel radionuclide-based multi-pinhole molecular breast tomosynthesis (MP-MBT) scanner.

The MP-MBT system images radionuclide distributions in a mildly compressed breast using two opposing gamma cameras, each equipped with a focusing multi-pinhole collimator, that slide along opposite sides of the breast. VRT simulates gamma photon transport by tracing rays efficiently through the voxelized phantom, collimator, and detector volumes using Siddon's ray-tracing algorithm, accelerated by dual-grid methods. To assess its accuracy, we compare point spread functions (PSFs) calculated with VRT for different voxel sizes with those generated by the established MCS toolkit GATE. Furthermore, VRT and MCS-simulated projections of realistic anthropomorphic XCAT phantoms with different compressed breast sizes are compared, as well as reconstructed images obtained from these projections.

With VRT, PSFs for MP-MBT can be simulated accurately when the fine voxel size of VRT's dual-grid is 1/8 mm. Reaching a similar deviation from noiseless PSFs takes 28600 times longer with full MCS than with VRT. Furthermore, XCAT phantom simulations show that VRT-generated projections are very close to MCS-generated low-noise projections when these are corrected for scatter by the Triple Energy Window method. However, we also find that primary gamma photons from the torso may in some cases reach the detector, meaning that torso activity should not be neglected in VRT. Finally, reconstructed images obtained from projections generated by VRT and MCS are visually very similar and have no significant difference in contrast and noise characteristics.

We conclude that VRT can accurately and efficiently simulate MP-MBT even though it neglects scattered photons originating from the torso.

3.1   Introduction

Imaging of radiolabelled molecule distributions is gaining popularity for breast cancer diagnosis. Recently, several breast-specific gamma cameras have been proposed and significant advances in sensitivity of these cameras have been made (Mueller *et al.*, 2003; Coover *et al.*, 2004; Hruska *et al.*, 2008; Hruska *et al.,* 2012a; Hruska *et al.*, 2012b; Siman & Kappadath, 2012; Long *et al.*, 2016). Next to these planar gamma cameras, there is also a growing interest in 3D molecular breast imaging. General purpose single photon emission computed tomography (SPECT) and positron emission tomography (PET) are not ideal for breast imaging because they often pro-

vide no higher diagnostic sensitivity and specificity than planar systems (Fowler, 2014; Hruska & O'Connor, 2013). Therefore, dedicated 3D molecular breast imaging techniques are being investigated (Baghaei *et al.*, 2010; Brzymialkiewicz *et al.* 2005; Gong & Williams, 2015; Gopan *et al.* 2014; MacDonald *et al.*, 2009; Moliner *et al.*, 2012; Raylman *et al.*, 2008; Tornai *et al.*, 2003; Williams *et al.* 2010; Yanagida *et al.*, 2010). In **Chapter 2**, we proposed dedicated molecular breast tomosynthesis based on sliding multi-pinhole collimators, MP-MBT (F.J. Beekman, 2010; van Roosmalen *et al.,* 2016).

To investigate the performance of MP-MBT and to further optimize its design, its acquisition, and its reconstruction parameters, efficient simulation algorithms are useful. To be able to evaluate images that could be acquired with MP-MBT, one has to be able to generate both noisy ensembles of projections of realistic distributions, as well as the virtually noiseless point spread functions (PSFs, the detector's response to a point source of activity) that are used in image reconstruction. Monte Carlo simulation (MCS) is a powerful technique for assessing gamma photon transport (Rogers, 2006) and its accuracy has been extensively validated in the scientific community. However, MCS is also notoriously time-consuming (De Beenhouwer *et al.*, 2007; Gieles, *et al.,* 2002; Haynor *et al.*, 1990).

Several ways to speed up MCS exist, such as applying a large production threshold for secondary particles (Jan *et al.*, 2011; Jan *et al.*, 2004), ignoring some of the physics processes generating secondary particles (Cot *et al.*, 2002, 2004; Devries *et al.*, 1990) or optimizing code for a specific application (Hunter *et al.*, 2013). New implementation strategies based on graphics processing units (GPUs) have also recently become available (Bert *et al.*, 2013; Garcia *et al.*, 2016; Lippuner & Elbakri, 2011). Another class of accelerated MCS uses variance reduction techniques such as forced detection, angular response function modelling or fictitious interaction (F. J. Beekman *et al.,* 1999; de Jong *et al.,* 2001; Descourt *et al.*, 2010; El Bitar *et al.*, 2011; Gieles *et al.*, 2002; Haynor *et al.*, 1990; Ljungberg *et al.*, 2005; Rehfeld *et al.*, 2009; Wang *et al.*, 1993). However, even with modern hardware and advanced acceleration techniques, for certain applications, MSC is still prohibitively slow and complete system simulations often take days (El Bitar *et al.*, 2011; Garcia *et al.*, 2016).

If the effects of scatter are negligible or correctable in a gamma imaging system, a simulation that only models attenuation but ignores scatter is a possible way to reduce calculation time. This can be done using a simple raytracing algorithm, in which the paths from the gamma source to the detector are tracked and attenuation of gamma photons along these paths is calculated. Analytical raytracing software, in which phantom, collimator and detector geometries are described by analytical functions, has been used to generate PSFs for simple imaging systems quickly and noiselessly (Feng *et al.*, 2010; Goorden *et al.*, 2011; X. Li & Furenlid, 2014). For complicated geometries which are difficult to describe analytically, such as irregular phantoms in CT and SPECT, discrete raytracing, in which geometries are represented by a finite number of voxels or layers, is more practical (Funk *et al.*, 2006; Goertzen *et al.*, 2002; Schramm *et al.*, 2003; Siddon, 1985; Smith *et al.* 1997; Tabary *et al.*, 2004). Among these discrete raytracers,

those that use a representation of volumes in cubic voxels (Voxelized Ray Tracing, VRT) are the most straightforward and suitable to represent highly irregular structures.

Voxelization of continuous structures introduces simulation errors since edges are no longer smooth but composed of cubic elements. The use of very fine voxels can reduce the error but puts a strain on memory requirements and slows down computation time. Solutions that have been proposed to circumvent the issue of balancing accuracy and simulation time in volume representation include using hybrid analytical-voxelized representations (Wang *et al.*, 1993), employing non-cubic voxel shapes (Matej & Lewitt, 1996; Zbijewski & Beekman, 2006) or using a spatial subdivision method such as an octree voxel size structure (Glassner, 1984; Meagher, 1982). Octree is a method for describing an object by repeatedly dividing a cubic voxel into eight smaller cubic regions until each region becomes homogeneous. It has been applied in medical imaging simulations (Badal *et al.*, 2009; Hubert-Tremblay *et al.*, 2006; Ogawa & Maeda, 1995; Sarrut & Guigues, 2008; Suganuma & Ogawa, 2000) and is, nowadays, widely used in 3D graphics for representing irregular volumes.

In previous medical imaging instrumentation research in which VRT was applied, only phantoms or detectors were represented by voxels (Siddon 1985, Smith *et al.* 1997, Huesman *et al.* 2000, Goertzen *et al.* 2002, Schramm *et al.* 2003, Tabary *et al.* 2004, Lin *et al.* 2010). In contrast, we developed VRT software in which all volumes (gamma emitter, phantom, collimator and gamma detector) are voxelized. Fixed voxel sizes are used in phantoms and detectors, but in the collimator volume for which precise geometrical knowledge is crucial and through which raytracing is most time-consuming, a form of an octree-like voxel structure with two different voxel sizes is used. Though VRT provides an attractive alternative to MCS in testing system geometries such as MP-MBT, its validity lies in the prerequisite that scatter is negligible or correctable. As tracer uptake in breast imaging is relatively high in organs such as the liver and heart (Maublant *et al.*, 1996; Wackers *et al.*, 1989), a careful assessment of its contribution in our MP-MBT system is required. For other breast gamma imaging geometries, different amounts of scatter contamination were reported and it is thus not a priori clear what the amount of scatter is in MP-MBT (Brzymialkiewicz *et al.*, 2005; Campbell & Peterson, 2014; Gruber *et al.*, 1999; Hruska & O'Connor, 2006, 2008a; Pani *et al.*, 1998; Williams *et al.*, 2003).

The aim of this paper is to propose our specific VRT implementation and to validate the use of VRT for MP-MBT. To this end VRT is compared against the MCS software package GATE (Geant4 Application in Tomographic Emission, (Jan *et al.*, 2011; Jan *et al.*, 2004)) which is considered to be the gold standard. PSFs, projections, and reconstructed images of the anthropomorphic XCAT phantom (Segars & Tsui, 2009) are generated by both software packages and simulation accuracy of VRT and its dependence on collimator volume voxel size settings are analysed.
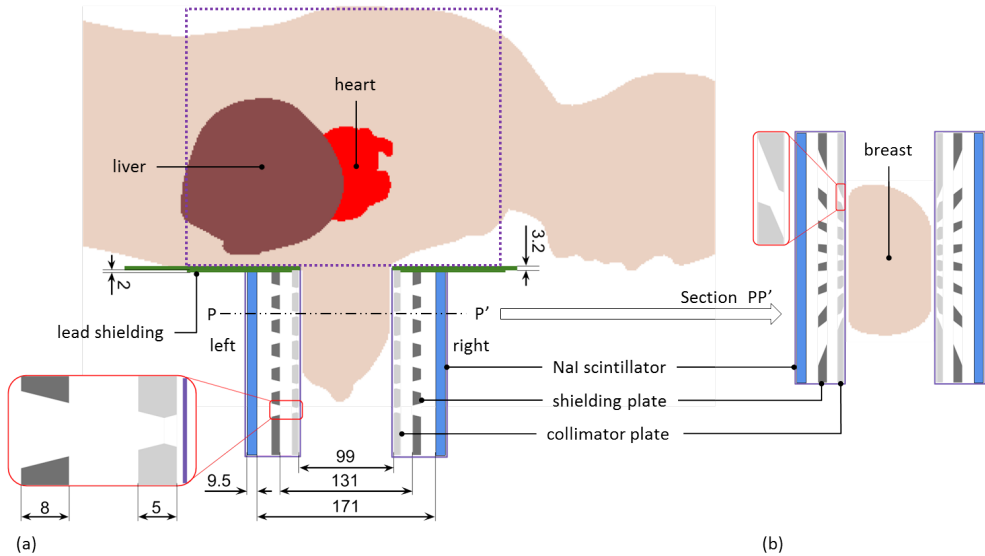
Figure 3-1 (a) Geometry of MP-MBT with the XCAT torso phantom placed in the scanner. The dotted rectangular box indicates the part of the torso phantom included in GATE simulations but not in VRT. The two gamma cameras can slide to different locations (indicated by the arrows) to focus on different parts of the breast. (b) A cross section through the gamma camera geometry (plane PP' in (a)). All dimensions are in millimetre (mm).

3.2 Method

3.2.1 MP-MBT

The novel MP-MBT concept (shown in Figure 3-1) was proposed in F.J. Beekman (2010) and in Chapter 2 of this thesis in which a detailed description can be found. MP-MBT aims to image the distribution of single-gamma emitting tracers in the breast to detect possible malignancies. The breast is pendant through a hole in the patient bed (equipped with 3.2 mm thick lead for shielding) and is mildly compressed at levels similar to planar molecular breast imaging (Hruska *et al.*, 2008) with optically transparent plates, through which optical cameras (not shown in Figure 3-1) view the breast. These optical cameras generate images, from which users can select a volume-of-interest which is to be imaged. Imaging takes place by the two gamma cameras located underneath the patient bed, each equipped with a multi-pinhole collimator focusing on a volume smaller than the whole breast, cf. Figure 3-1(b). The gamma cameras slide to various positions during scanning in order to cover the region designated by the user. Each of the 5 mm thick collimator plates, made of tungsten alloy (97% tungsten, 1.5% nickel, and 1.5% iron), has 42 round knife-edge pinholes. An 8 mm-thick shielding plate made of the same material is located between gamma detector and collimator plate. It has 42 rectangular holes, each of them corresponding to one of the pinholes in the collimator respectively avoiding different pinhole projections from overlapping on the gamma detectors. Gamma detectors are assumed to consist of 250×150×9.5 mm3 NaI(Tl) crystals read out by a PMT array. For 140 keV gamma photons

(from 99mTc-Sestamibi, the most prominent tracer for breast tumour detection), 90% detection efficiency can be achieved by NaI of this thickness. With the projections obtained from the two gamma cameras, the 3D tracer distribution in the breast can be reconstructed using a maximum likelihood expectation maximization algorithm (van Roosmalen *et al.*, 2016; Vastenhouw & Beekman, 2007).

3.2.2   VRT

VRT uses voxelized models of the detectors, collimators, phantoms, and the distribution of single-gamma emitters as its input. Each voxel is assigned a value which corresponds to the linear attenuation coefficient *μ* of its material at the energy of the gamma-emitter. When a gamma photon path crosses a voxel, the path length *L* through this voxel is obtained. Siddon's raytracing algorithm is used to quickly calculate path lengths in voxels (Siddon, 1985). Lambert-Beer's law,

$$P = e^{-\mu L} \tag{3-1}$$

is then used to calculate the transmission probability P through the voxel. During raytracing, the transmission probabilities in the voxels that the ray passes are multiplied giving a total transmission probability. As there is always a finite probability for a gamma photon to pass through phantom and collimator, one could in principle calculate the full transmission probability along every simulated gamma ray path. However, many gamma rays pass through large amounts of collimator material (tungsten alloy), making the transmission probability extremely small and it is computationally inefficient to keep track of all these paths. We, therefore, set a cut-off of 10^{-5} (2.76 mm collimator material) on the transmission probability through phantom and collimator below which ray tracing is stopped.

The surface of the gamma detector is divided into detector pixels and each pixel is subdivided into 4×4 subpixels. For projection image assessment the pixel size is set to 1 mm, while for PSF assessment 0.5 mm is used. Gamma photons from each source position are tracked to the centres of all subpixels. The solid angle of each subpixel is taken into account by multiplying the transmission probability through the collimator of the gamma photons by the geometrical factor

$$P_{\text{geometry}} = \frac{d^2 \sin \theta}{4\pi R^2} \tag{3-2}$$

where *R* is the distance from the voxel centre to the detector subpixel centre, *d* is the detector subpixel size, and θ is the angle of incidence of the gamma photon (see Figure 3-2(a)).

The gamma photon is subsequently tracked through the continuous NaI(Tl) gamma detector which is represented in a voxelized form as well: it is subdivided into rectangular voxels with the length of each voxel being equal to the detector crystal's thickness (9.5 mm) and the area having the size of a detector subpixel. In the gamma detector, Lambert-Beer's law is again used to calculate the absorption probability in each detector voxel. Note that gamma photons that reach the detector under an angle can pass different rectangular voxels and this way the varying depth-of-interaction in the detector is simulated (see Figure 3-2(b)). The attenuation coefficient of the detector is set to 0.217 mm^{-1}. This number is higher than the attenuation coefficient that
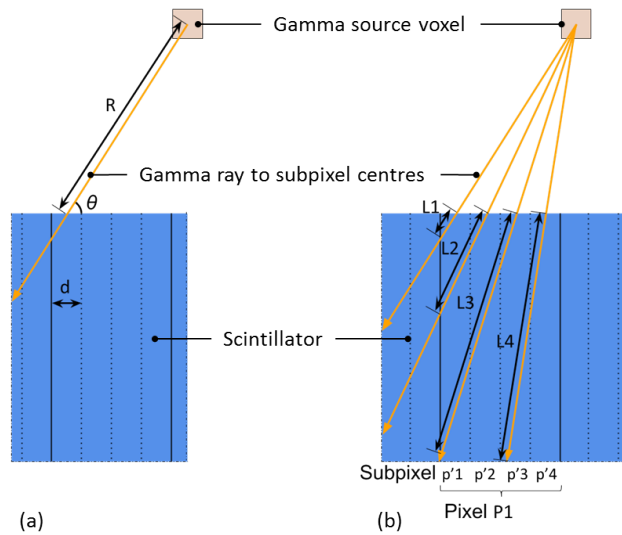
Figure 3-2 (a) The geometrical parameters used in equation (2); (b) Illustration of the detector subpixel approach used in VRT. With the subpixel approach, the detection probability at pixel P1 is the sum of the absorption probabilities of subpixel p'1 – p'4, determined by path length L1 – L4. Discretization errors are reduced by this subpixel approach.

solely includes photoelectric effect but lower than the total attenuation coefficient for 140 keV gammas in NaI (including Compton scatter). In fact, we set the attenuation coefficient such that the number of detected gammas in VRT with this attenuation coefficient is equal to the number of detected gammas found in the ±10% photopeak from GATE simulated PSFs. Thus, the added detector efficiency due to gamma photons undergoing multiple interactions in the scintillator is accounted for in VRT, but the scatter process itself which may impact spatial resolution is not taken into account. Finally, for each source position, absorption probabilities in all 4×4 detector subpixels corresponding to a detector pixel are added. The detector projection image acquired is then blurred with a Gaussian filter with 3.2 mm FWHM in order to simulate the intrinsic detector resolution. The idea of subdividing detector pixels to enhance modelling accuracy has been successfully applied in Huesman *et al.* (2000) and Lin *et al.* (2010) and the usefulness of this approach in MP-MBT will be evaluated in the results section.

The voxel sizes of collimator and shielding plates can have a significant impact on simulation results and they thus have to be chosen carefully. Generally, a small voxel size is preferable because it allows to better approximate the continuous structures in the geometry, but it also puts a strain on memory requirements and simulation time. To circumvent this issue, a dual-grid approach is used based on the idea of octree structure (Badal *et al.*, 2009; Glassner, 1984). Figure 3-3 is a 2D illustration of this approach: two different voxel sizes, a coarse one and a fine one, are used for the collimator/shielding volume. Initially, a photon is traced through the coarse voxel volume. In the coarse voxel volume, each voxel is designated to have one particular linear attenuation coefficient or it is assumed to be 'mixed' (i.e. the coarse voxel contains fine voxels
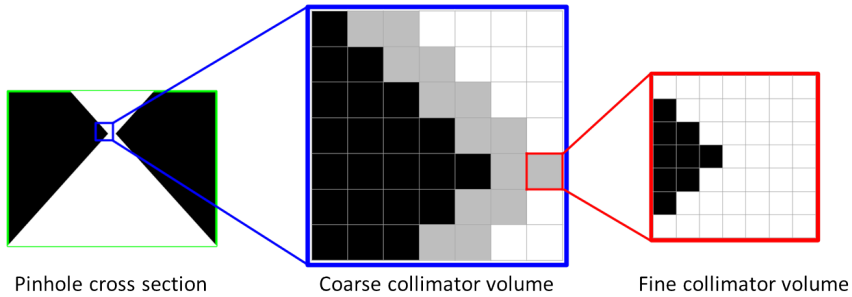
Figure 3-3 Illustration of dual-grid representation of collimator. The pinhole collimator volume consists of two materials: tungsten alloy (black) and vacuum (white). The grey coarse voxels are designated to be 'mixed' material and rays through these voxels are tracked on a finer volume.

with different linear attenuation coefficients). When a gamma ray is tracked through the coarse voxels, cumulative attenuation in the non-'mixed' voxels is calculated. When the ray reaches a 'mixed' voxel, VRT looks for the fine grid of this coarse voxel and continues raytracing in the fine voxels until the ray exits this coarse voxel. VRT checks whether the probability of transmission is lower than the cut-off after every fine/coarse voxel tracing.

With this dual-grid raytracing approach, the voxel size of the fine volume determines the accuracy of simulation while the combination of fine and coarse voxel sizes sets the computational speed. In this paper we first test six fine voxel sizes (1/2 mm, 1/4 mm, 1/8 mm, 1/16 mm, 1/32 mm, 1/40 mm) to determine the accuracy that we can achieve (with coarse voxel size fixed at 1 mm). Then, in order to optimize speed, we check six coarse voxel sizes (1/4 mm, 1/2 mm, 1 mm, 2 mm, 3 mm, 5 mm) to find out which one allows for the highest speed (with the optimal fine voxel size found above).

3.2.3   MCS

To validate VRT, we use the MCS package GATE (Jan *et al.*, 2011; Jan *et al.*, 2004), which is well-validated in gamma-ray imaging, radiation therapy, X-ray imaging, and optical imaging (Assie *et al.*, 2005; Brunner *et al.*, 2009; Chen *et al.*, 2009; Grevillot *et al.*, 2011; Lamare *et al.*, 2006; Schmidtlein *et al.*, 2006; Staelens *et al.*, 2006; van der Laan *et al.*, 2010). GATE 7.0 with Geant4 9.6 running on a CentOS 6.6 cluster is used. Only photoelectric effect, Compton scattering, and Rayleigh scattering are included in the physics list, since other physics processes are not expected to play major roles in our application (Cot *et al.*, 2002, 2004; Devries *et al.*, 1990). The same geometry as simulated with VRT is also built in GATE. As we aim to assess the influence of finite voxel size in VRT, the collimator and shielding plates are generated with analytical shapes (head-to-head cones, trapezoids, and boxes), such that the GATE simulation does not suffer from discretization effects due to the finite voxel size. The adder digitizer is applied to GATE outputs, which automatically records the interaction time, deposited energy, and energy-weighted averaged scintillator interaction position (Jan *et al.*, 2004). Gaussian blurring of energy is applied to each detector pixel to achieve 9% FWHM energy resolution, and Gaussian blurring in the spatial domain is also applied to simulate 3.2 mm FWHM resolution (as is done
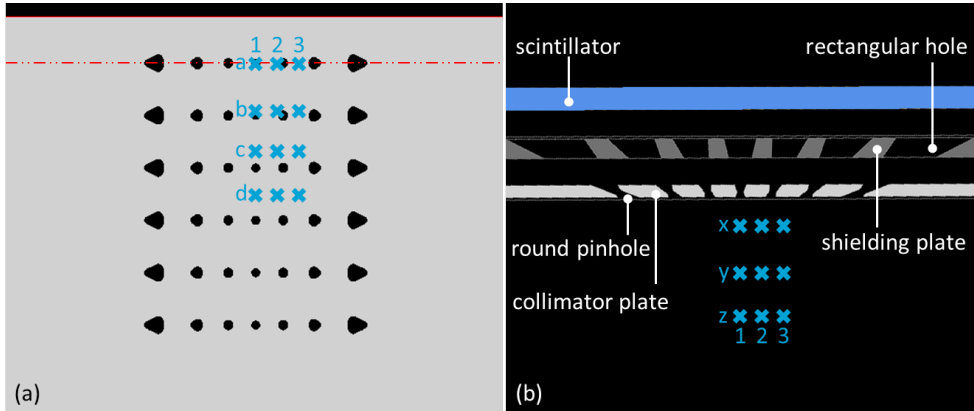
Figure 3-4 The gamma camera geometry used in GATE based on analytical shapes. (a) Front view of collimator; (b) cross section of the plane marked by a red dashed line in (a). The blue crosses indicate the locations where point sources are simulated to obtain the system's PSFs.

in VRT). To note, the blurring in energy and spatial domain acts as an acceleration factor of MCS and reduces noise. As we aim to compare GATE simulations with noiseless VRT, such a noise reduction is desirable. A difference between GATE photon tracking and VRT is that in GATE the gamma photons can be emitted in any possible direction, while in VRT only gamma photon paths from the centres of the gamma source voxels to the centres of the detector subpixels are accounted for. Figure 3-4 shows one of the two gamma cameras in GATE.

3.2.4   VRT's accuracy and fine voxel size optimisation

To study the accuracy of VRT for different voxel sizes (of the fine volume), PSFs are obtained with VRT and GATE from point sources (ideal point source of infinitely small size) placed in the vacuum at 36 locations in front of the gamma camera (the blue crosses in Figure 3-4). The position designated by ax1 is 11.5 mm from the front surface of the collimator plate and right on the axis of the central pinhole. The vertical interval (e.g. a-b distance) between these locations is 20 mm, the horizontal interval (e.g. 1-2 distance) is 10 mm, and the depth interval (e.g. x-y distance) is 20 mm. These 36 positions cover about a quarter of the field of view and are representative of the whole field of view due to the symmetric allocation of the pinholes. Therefore, the voxel sizes optimised for these PSFs should also be the optimal voxel sizes for calculating the whole system matrix (containing all PSFs). To find how the fine voxel size influences accuracy, a sufficiently long GATE simulation of 5×10^{10} isotropic emissions is done to obtain an almost noiseless reference PSF at each source location. The normalised root-mean-square error (NRMSE) between the PSFs obtained by VRT simulations with different fine voxel sizes (see section 3.2.2) and the reference PSFs is calculated. It is defined by

$$NRMSE_{\text{GATE,VRT}} = \frac{\sqrt{\dfrac{\sum\limits_{x=1}^{X} \sum\limits_{y=1}^{Y} \left(n_{\text{GATE}}(x, y) - n_{\text{VRT}}(x, y)\right)^2}{XY}}}{n_{\text{GATE,max}} - n_{\text{GATE,min}}} \tag{3-3}$$

where x and y are detector pixel indices. There are $X \times Y$ pixels in the PSF image and $n_{\text{GATE}}(x, y)$ and $n_{\text{VRT}}(x, y)$ are the number of counts in detector pixel (x,y) obtained with GATE and VRT respectively. $n_{\text{GATE,max}} - n_{\text{GATE,min}}$ is the range of counts in the PSF obtained by GATE. The average NRMSE over PSFs from all 12 positions (referred to as a PSF-set) is calculated for each of the fine voxel sizes tested for VRT. In this comparison, the voxel size of the coarse volume, which does not influence simulation accuracy but only affects simulation time, is fixed to be 1 mm. The detector pixel size is fixed at 0.5 mm for all PSF simulations.

3.2.5   *VRT time-efficiency and coarse voxel size optimisation*

To optimize the time-efficiency of VRT, the same PSFs as described in section 3.2.4 are again simulated with the optimized fine voxel size for 6 different VRT coarse voxel sizes (see section 3.2.2) and the simulation times are recorded. This way the coarse voxel size which resulted in the fasted simulation could be determined.

Subsequently, we compare the time-efficiency of VRT with optimized voxel settings to that of GATE. For a comparison, one has to choose a setting for the number of photons tracked in GATE. For the validation study, we track 5×10^{10} photons at each point source position as this results in almost noiseless PSFs and can thus serve as a gold standard. If fewer photons are tracked, PSFs become noisier and thus starts to deviate from the gold standard. Although this deviation from the gold standard is due to different reasons than the deviation obtained with VRT (which can be due to neglect of physics processes, due to scatter, or due to discretization effects) we choose to determine the relative time-efficiency of VRT compared to GATE, by comparing the time it takes for GATE to arrive at the same difference level from the gold standard as VRT (again characterized by "NRMSE"). To this end, PSF-sets from GATE simulations with a series of different numbers of emissions are generated and "NRMSE" from the gold standard is calculated for each of them. Moreover, as is mentioned in section 3.2.3, GATE simulation results are blurred in energy and spatial domain with Gaussian kernels in order to mimic the desired energy and spatial resolution. The use of a kernel-based way of simulating resolution instead of picking a random detector position and energy value from the detector response function (a full MCS) is a way of accelerating MCS and it is very useful in case one is interested in noiseless PSFs. Throughout this paper, we use accelerated MCS to avoid too lengthy simulations, but in the time-efficiency comparison, we also provide acceleration factors of VRT with respect to full MCS, in which the interaction energy and position are, instead of blurred, randomised according to a 9%-FWHM and 3.2 mm-FWHM Gaussian distribution respectively. In our time comparison study, all simulations are executed on the same multi-CPU computer cluster, and 25 CPUs are used.

3.2.6   *Projection image comparison*

In MP-MBT, the scattered gamma photons from torso and breast can be detected by the gamma detector and if the energy of these scattered photons is within the photopeak window, they will usually add a rather continuous background to the projection image. As tracer uptake in organs is rather high in breast imaging, scatter is a topic of concern in molecular breast imaging and

Table 3-1 Tracer uptake in different tissues

Tissue	Uptake
Breast	3.7 kBq/ml
Torso	3.7 kBq/ml
Heart	55.5 kBq/ml
Liver	55.5 kBq/ml

in some designs high energy resolution gamma detectors are used (Mueller *et al.*, 2003; Hruska *et al.* 2012a, 2012b). The amount of scatter that will be detected depends on the exact system's geometry and different studies have reported very different numbers (Pani *et al.*, 1998; Gruber *et al.*, 1999; Williams *et al.*, 2003; Brzymialkiewicz *et al.*, 2005; Hruska & O'Connor, 2006, 2008a; Campbell & Peterson, 2014).

It is thus important to evaluate the influence of scatter in MP-MBT with a realistic anthropomorphic phantom. For this reason, we implement the well-known XCAT phantom with heart, liver, torso, and deformable breasts in the GATE simulation, see Figure 3-1 (C. M. Li *et al.* 2009; Segars *et al.*, 2010; Segars & Tsui, 2009). Instead of using dual-grid voxels, the voxel sizes of the XCAT phantom are fixed: the torso, including the heart and the liver, is voxelized to a 3.2 mm grid, and the breast is voxelized to a 0.8 mm grid. Two breast sizes are checked: a 400 mL breast compressed to a thickness of 55 mm (a common B-cup breast), and a 1300 mL breast compressed to a thickness of 85 mm (a common D-cup breast). The latter breast is shown in Figure 3-1. To note, the distance between the two collimators is larger than the thickness of the breast because of the 7 mm thick compression plate. The tracer uptake that we assumed in different organs is listed in Table 3-1. These are typical numbers found in practice if 925 MBq 99mTc-Sestamibi is injected to the patient (Wackers *et al.*, 1989; Maublant *et al.*, 1996; Wang *et al.*, 1997; Brzymialkiewicz *et al.*, 2005; Hruska & O'Connor, 2008a, 2008b; Perez *et al.*, 2010).

In GATE, the detected photons are categorised according to their origin and interactions they have undergone: they are listed to be either breast-emitted or torso-emitted, and scattered or non-scattered. This way we are able to divide the total energy spectrum into different categories in order to better pinpoint which photons cause possible differences with VRT. Moreover, we apply the widely acknowledged Triple-Energy Window (TEW) scatter correction method to GATE simulated projections, in order to check if the scatter can be estimated this way (Ogawa *et al.*, 1991). We set a ±10% photopeak window (126 – 154 keV), a 14 keV wide left side window (119 – 133 keV), and a 14 keV wide right side window (148 – 161 keV). For a certain detector pixel with N_L counts in the left side window and N_R counts in the right side window, scatter is then estimated to be

$$N_S = \frac{N_L + N_R}{2} \frac{28\text{keV}}{14\text{keV}} \cdot 0.6 \tag{3-4}$$

Note there is a factor 0.6 in (3-4), which aims to make the total counts after TEW correction the same as acquired with VRT. In reality, when the number of scattered photons is not known one may base this number either on simulations or different values may be tested in an optimization study. We subtract this scatter estimate from the simulated projections to obtain TEW-corrected projections. The occurrence of negative values in the projections is prevented by setting them to zero. Note that the comparison of VRT images with scatter-corrected GATE images is relevant to assess bias as in real scanners a TEW-based scatter correction method is commonly applied.

Full projection images (with scatter), scatter-free GATE projections, TEW-corrected GATE projections, and VRT projections of the same phantom scan are compared. To note, in the VRT simulations, only the compressed breast phantom is included while the torso phantom is neglected. Additionally, in generating projections, VRT only tracks the rays through the breast phantom (single grid). The subsequent raytracing through the collimator (dual-grid) is done using previously acquired PSFs that were stored on disk. The transmission probability obtained from raytracing through the phantom is then multiplied by the corresponding collimator raytracing transmission factor. This gives exactly the same results as a complete raytracing simulation from each activity containing voxel in the phantom through the collimator to the detector but is more efficient.

3.2.7   *Image reconstruction*

The comparison of PSFs and projection images allows to estimate how accurate VRT is in the noiseless case and to which extent the TEW method corrects for the bias caused by scattered photons. However, when simulating reconstructed images with realistic noise levels, neglecting scatter may also lead to an underestimation of noise in images as detector images of scattered photons are noisy themselves. To better investigate the impact of this, we also simulated a full scan of the 400 mL breast phantom with a 6.0 mm diameter spherical lesion inside (see Figure 3-5) using both GATE and VRT to obtain projection images. For normal breast tissue and organs we assume the realistic activity levels provided in Table 3-1 while the lesion uptake is taken to be 37 kBq/mL, 10 times as high in normal breast tissue. The total scan time is assumed to be 10 minutes. In case GATE is used to simulate projection images, the number of gamma emissions corresponding to the given activity levels and scan time are simulated. When VRT is used, noiseless projection images are generated (similar as described in section 3.2.6) after which Poisson noise is applied. In order to be able to acquire 3D reconstructions, projection images are acquired for a total of 170 different positions of the sliding gamma detectors. Precise information on the positions used and other scan details can be found in van Roosmalen *et al.* (2016).
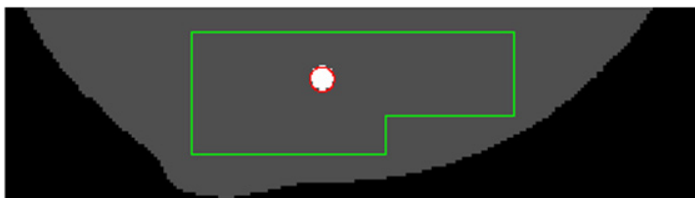

Figure 3-5 A slice of the XCAT breast phantom with a 6 mm diameter lesion inside. The red circle labels the lesion, and the green polygon marks the background.

The projections generated by either GATE or VRT are used as the input of a maximum likelihood estimation maximisation (MLEM) reconstruction algorithm, while the system matrix used in MLEM in both cases is generated by VRT. Data acquired from different gamma detector positions are all simultaneously taken into account in image reconstruction (Vastenhouw & Beekman, 2007). In case GATE-generated projections are used, TEW scatter correction is applied to compensate for scatter from the breast and torso. In that case, scatter images are obtained in the same way as in section 2.6 but an additional Gaussian filter with 11.8 mm FWHM is applied to smooth them. The reason to blur the scatter images is to limit the noise amplification due to TEW correction as is usually done (Ichihara *et al.* 1993, Hashimoto *et al.* 1997). The scatter images are then added to the simulated projections in the denominator of the MLEM algorithm similar as summarised in Hutton *et al.* (2011). Note that the size of the smoothing filter and the side windows chosen are not optimised in this study. While voxel size of the phantom in VRT and GATE simulations was set to 0.8 mm, voxel size of reconstructed images was 1.6 mm, in order to mimic a realistic continuous activity distribution.

Ten GATE simulations and ten noise realisations of VRT-simulated projections are used to generate reconstructed images. Besides visually comparing reconstructed images, we also compared the mean contrast of the lesion over the background, as well as the noise as standard deviation in the background. Figure 3-5 shows how we defined the regions used; the area inside the 6 mm diameter red circle is considered to be lesion area, while the area > 3 mm outside the red circle but still inside the green polygon is considered to be background area.

3.3   Results

3.3.1   VRT accuracy for generating PSFs

In Figure 3-6, an example PSF profile is shown for collimators parametrized by different fine volume voxel sizes. From this image, one can see that the setting of the fine voxel size influ-
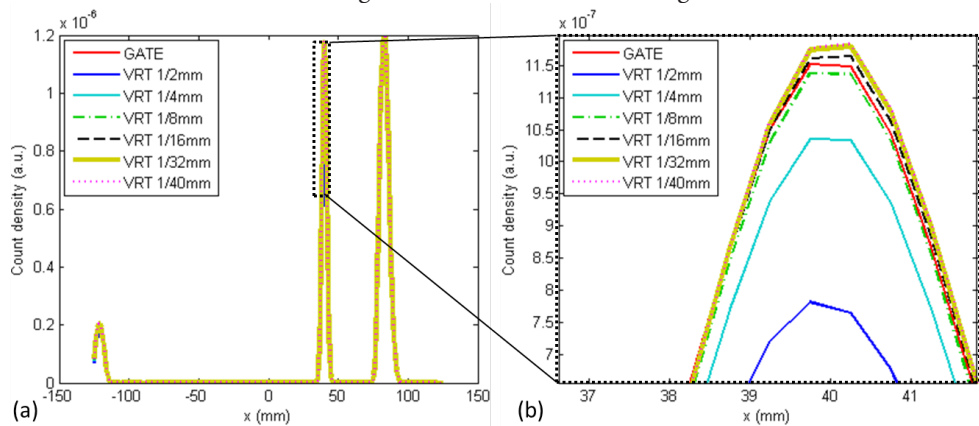

Figure 3-6 (a) Simulated PSF profiles for the c3 location (see Figure 3-4). GATE generated PSFs and VRT generated PSFs using different fine collimator volume voxel sizes are shown; (b) is the enlarged view of the part of (a) in the black dotted box.

Table 3-2 Comparison of simulation accuracy for different fine volume voxel sizes (coarse volume voxel fixed at 1 mm)

Fine volume voxel size	Difference from reference	
	NRMSE	Max. Diff.
1/2 mm	0.601%	33.13%
1/4 mm	0.234%	11.21%
1/8 mm	0.143%	5.07%
1/16 mm	0.140%	5.32%
1/32 mm	0.150%	6.34%
1/40 mm	0.151%	6.18%

ences the accuracy of generating PSFs, especially near the PSF's maximum. The counts of the GATE-generated PSF (considered to be the ground truth) are normalised to the total number of emissions of the point source (5×10^{10}) so that the total counts in a PSF represent the sensitivity of the scanner. No scaling factor needs to be applied to VRT-generated PSFs as solid angle is taken into account.. As explained in the method section, photons that scatter in the collimator or scintillator and end up being detected in the photopeak are included in GATE-generated PSFs.

In Table 3-2, the differences between VRT-simulated PSFs and GATE-simulated reference PSFs are quantified by means of the NRMSE, averaged over the 12 point source positions. The maximum difference over the 12 positions is also provided. From the table, we can infer that the differences between VRT and reference PSFs become smaller when the fine volume voxel size is decreased from 1/2 mm to 1/8 mm. Therefore we choose 1/8 mm to be the fine voxel size in subsequent simulations. For smaller voxel sizes the error does not decrease anymore and even slightly increases. This slight unexpected increase will be discussed later. In the current VRT simulation, every detector pixel is divided into 4×4 subpixels in the simulation. Without this subpixel approach, the NRMSE and maximum difference for the 1/8 mm fine voxel size increase to 0.230% and 11.83% respectively. Therefore, the subpixel approach does improve the accuracy of VRT and is also applied in the subsequent comparison.

Figure 3-7 shows several PSFs at different locations in the field of view obtained with GATE (reference) and VRT with the 1/8 mm fine voxel size setting. The profiles are shown on both linear and semi-logarithmic scale. These profiles confirm that GATE and VRT give very similar PSFs as could also be assessed from the numbers in Table 3-2.

It is worth noting that in the semi-log scale graphs (Figure 3-7 (b), (e), and (h)), the amplitude of VRT-generated PSFs goes to zero at locations in between pinholes while GATE-generated PSFs do not. The reason that there is zero signal for VRT is the result of the applied cut-off described in section 3.2.2, that results in ray-tracing being stopped when traversing more than 2.76 mm of collimator material. In GATE, such a cut-off is not applied and as scattered photons
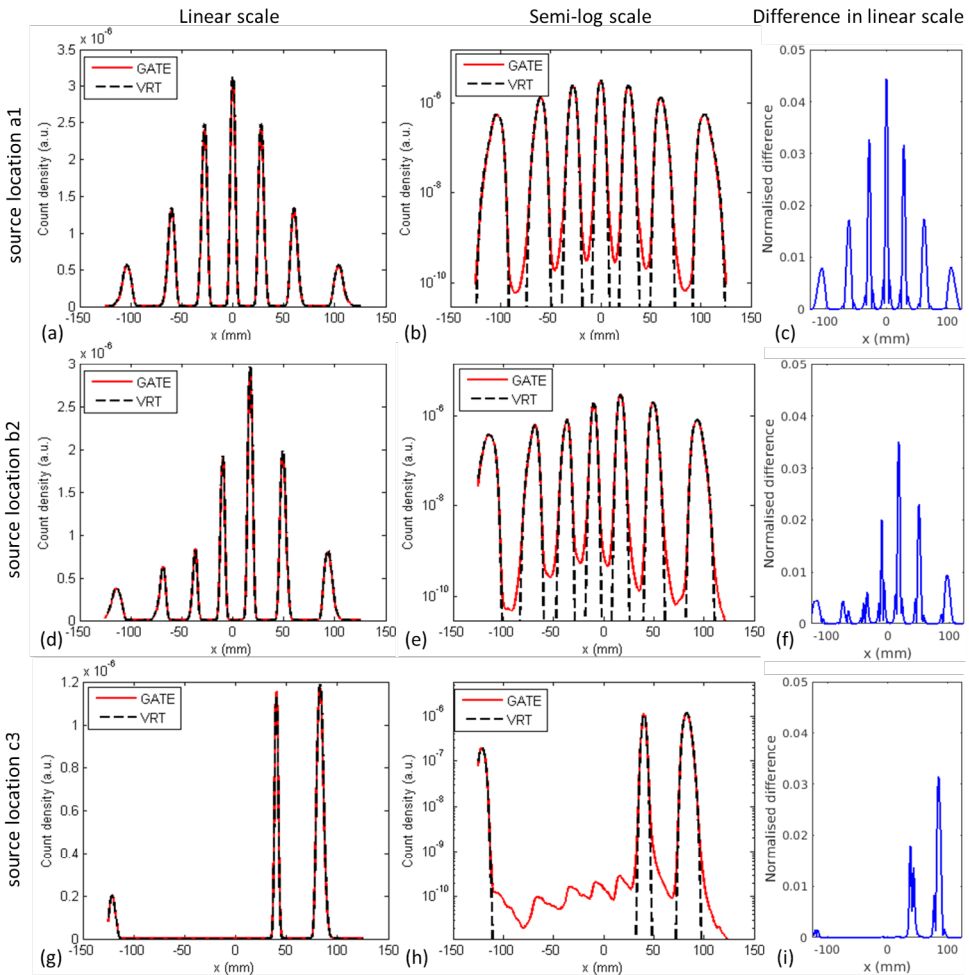
Figure 3-7 Central PSF profiles obtained with GATE and VRT for optimised fine voxel size of 1/8 mm. Gamma source is at location a1 (a-c), b2 (d-f), and c3 (g-i) in Figure 3-4. PSFs on linear scale and semi-log scale are shown, as well as the difference plots between VRT and GATE normalized to the maxima of GATE-simulated PSFs.

are included there can be a signal in any detector pixel. By analysing the simulation results, we found that the signal in between pinholes is mainly caused by gamma photons that undergo multiple interactions in the scintillator. In this situation, the total energy deposition can still be within the ±10% photopeak meaning that these photons are included, and the interaction position is estimated at the centroid of different interaction positions. Note that the signal in between pinholes is extremely small showing that all though VRT only includes detector scatter by adapting the NaI attenuation coefficient, it is well able to simulate MP-MBT including resolution degradation due to multiple scatter in the scintillator.

Table 3-3 Comparison of simulation accuracy for different fine volume voxel sizes (coarse volume voxel fixed at 1 mm)

Coarse volume voxel size	Time in VRT	Diff. from reference NRMSE
1/4 mm	122 s	0.143%
1/2 mm	67 s	0.143%
1 mm	38 s	0.143%
2 mm	24 s	0.143%
3 mm	41 s	0.143%
5 mm	65 s	0.143%

3.3.2   *VRT time-efficiency optimisation*

While the accuracy of VRT is only determined by the fine voxel size, the time-efficiency also depends on the coarse voxel size. In Table 3-3, the simulation time of VRT (total time required for obtaining the 12 PSFs) for different settings of the coarse volume voxel size is listed. A coarse voxel size of 2 mm is optimal in terms of computational speed and we therefore choose 2 mm as the coarse voxel size for this scanner in subsequent simulations. Table 3-3 also confirms that the accuracy of VRT remains the same once the fine voxel size is fixed.

To determine the relative speed of VRT compared to GATE, one has to set the number of emissions that has to be simulated in GATE. If the number of emissions decreases, PSFs become noisier and there is a difference to the reference (almost) noiseless PSFs with 5×10^{10} emissions simulated. The number of emissions that have to be simulated by accelerated (blurred) and full GATE to obtain the same difference level from the gold standard as VRT is 1.5×10^7 and 1.3×10^9 emissions respectively. For this number of emissions, VRT with optimized coarse voxel size is 330 times faster than accelerated GATE and 28600 times faster than full GATE. However, one should note that the sources of the deviation from the reference PSF are different: in GATE deviations are caused by stochastic noise, while in VRT they are due to the minor residual mismodelling of the system.
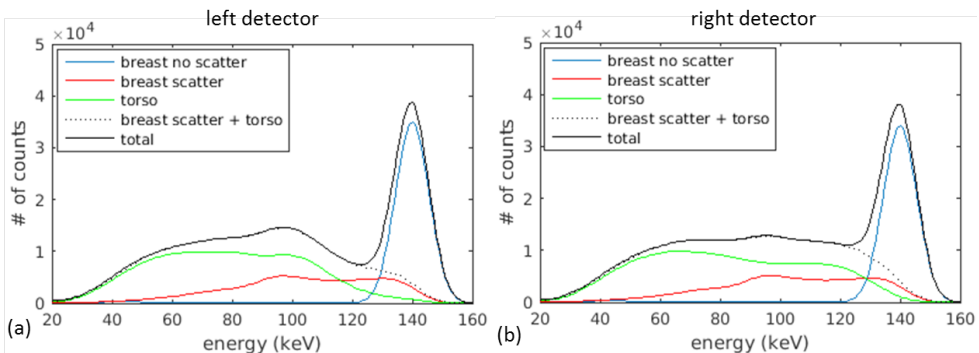
Figure 3-8 Energy spectra for the MP-MBT detectors obtained from GATE simulations of the 400 mL-breast.

3.3.3   *Projection image comparison*

3.3.3.1   *Phantom representing 400 mL breast*

Figure 3-8 shows energies of detected photons for the XCAT phantom simulation. Energy spectra are separated into different parts determined by the origin of the gamma photons ('breast' or 'torso') and the types of interactions they undergo before being detected ('scatter' or 'no scatter'). Here 'scatter' refers to both Compton and Rayleigh scatter in the phantom and collimator, while single scatter and multiple interactions in the scintillator are always included in all simulations. We did not distinguish between 'torso scatter' and 'torso no scatter' in the figures because the 'torso no scatter' fraction is too small to be visible in the whole detector spectrum. Figure 3-8(a) corresponds to the left detector (i.e. the detector closest to the liver, see Figure 3-1), and Figure

Figure 3-9 Left detector projection images of the GATE simulated XCAT phantom with the 400 mL-breast. (a) Full projection with scatter and torso signal; (b) projection without scatter (treated as ground truth for photons scattered in the phantom and collimator); (c) scatter-corrected projection using the TEW method; (d) the projection obtained with VRT (only breast phantom); (e) difference between VRT-generated projection and scatter-corrected projection. (f) and (g) are the horizontal and vertical profiles marked in white in (a) – (d).

Figure 3-10 Right detector projection images of the GATE simulated XCAT phantom with 400 mL-breast. (a) Full projection with scatter and torso signal; (b) projection without scatter (treated as ground truth for photons scattered in the phantom and collimator); (c) scatter-corrected projection using the TEW method; (d) the projection obtained with VRT (only breast phantom); (e) difference between VRT-generated projection and scatter-corrected projection. (f) and (g) are the horizontal and vertical profiles marked in white in (a) – (d).

3-8(b) corresponds to the right detector. The scatter fraction (the amount of gamma photons scattered in the phantom or collimator that get detected in the ±10% photopeak window) is about 20% on both detectors. The torso fractions (the amount of gamma photons originating from the torso) are 4% and 9% in the photopeak on the left and right detector respectively.

Projection images obtained by GATE and by VRT for the same phantom are shown in Figure 3-9 and Figure 3-10, as well as the profiles marked in white. In these images, a scatter-free projection (by simply ignoring photons that scattered in phantom and collimator) and a TEW-corrected projection are shown as well. The projection pattern from the pinholes can clearly be distinguished. These pinhole projections are non-overlapping, because of the design of the shielding

plate in between the multi-pinhole collimator and detector. Note that in these projection images only part of the detectors is used because these images are for the smaller (400 ml) breast. The projections from VRT are very similar to those from the scatter-corrected GATE projections and, as expected, scatter-free GATE projections. Since the TEW-corrected projections and the VRT-generated projections are very similar, the difference is hardly visible on the same colour scale. Therefore, we provide the same difference images shown in different colour scale in the supplementary material.

3.3.3.2   Phantom representing 1300 mL breast

In Figure 3-11, the same energy spectra as in Figure 3-8 are shown for the larger (1300 ml) breast. Corresponding projections and profiles can be found in Figure 3-12 and Figure 3-13. Like for the 400 ml breast, the scatter fraction in the ±10% photopeak window is about 20% on both detectors. The torso fractions are 4% and 7% in the photopeak on the left and right detectors respectively.

In contrast to the projections for the smaller breast shown in Figure 3-9 and Figure 3-10, in Figure 3-13 there is a discrepancy between the GATE projections and the projections simulated by VRT. To understand the cause of the difference, it is important to note that the TEW-corrected GATE projection is very close to the scatter-free GATE projections. Apparently, scatter can be well corrected for with the TEW method and the photons missed by VRT are not scattered photons but primary (non-scattered) photons. We come back to this issue in the discussion session. In Table 3-4, the differences between the TEW-corrected projection image and the VRT projection image are quantified in terms of NRMSE for both breast sizes. The maximum differences are listed as well. The NRMSE and maximum difference in the 1300 mL right breast are especially large, which reflects the discrepancy in Figure 13.

3.3.4   Reconstructed images

Figure 3-14 shows the same slice (3.2 mm thick) through reconstructed images obtained from (a) GATE-simulated projections, and (b) VRT-generated noisy projections. TEW scatter correction is applied in case GATE-simulated projections were used.. These images are post-filtered by a 3D
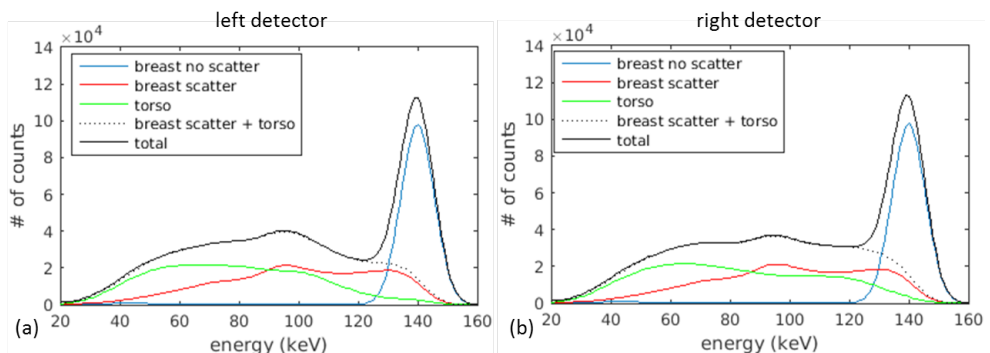
Figure 3-11 Energy spectrum of the MP-MBT detectors obtained from GATE simulations of the 1300 mL breast.
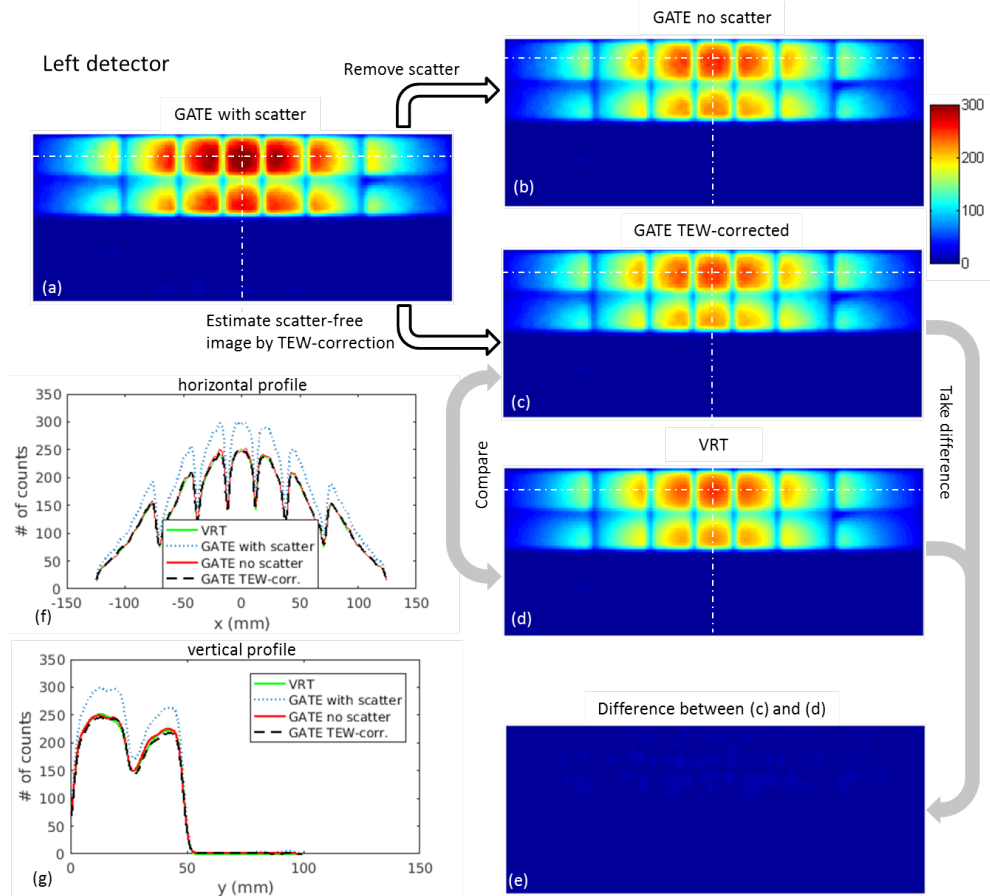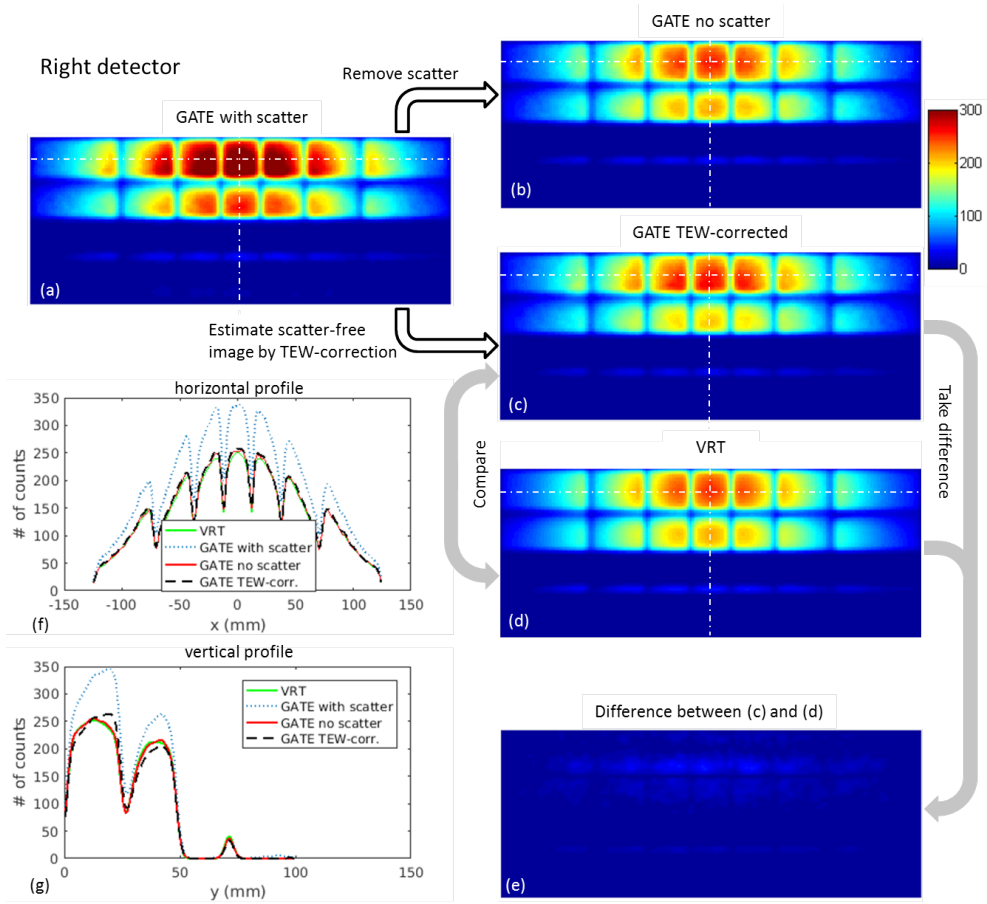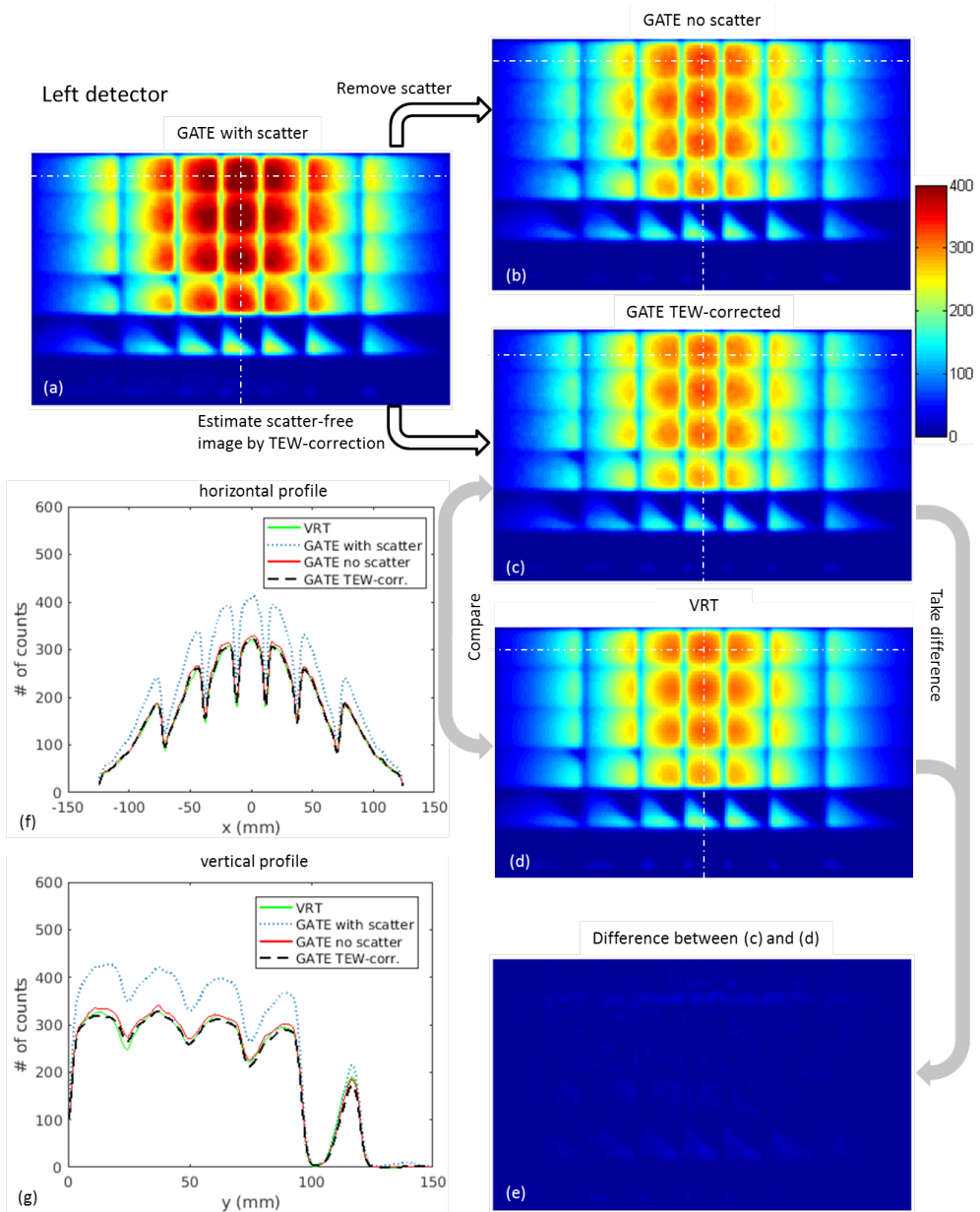
Figure 3-12 Left detector projection images of the GATE simulated XCAT phantom with 1300 mL-breast. (a) Full projection with scatter and torso signal; (b) projection without scatter (treated as ground truth for photons scattered in the phantom and collimator); (c) scatter-corrected projection using the TEW method; (d) the projection obtained with VRT (only breast phantom); (e) difference between VRT-generated projection and scatter-corrected projection. (f) and (g) are the horizontal and vertical profiles marked in white in (a) – (d).
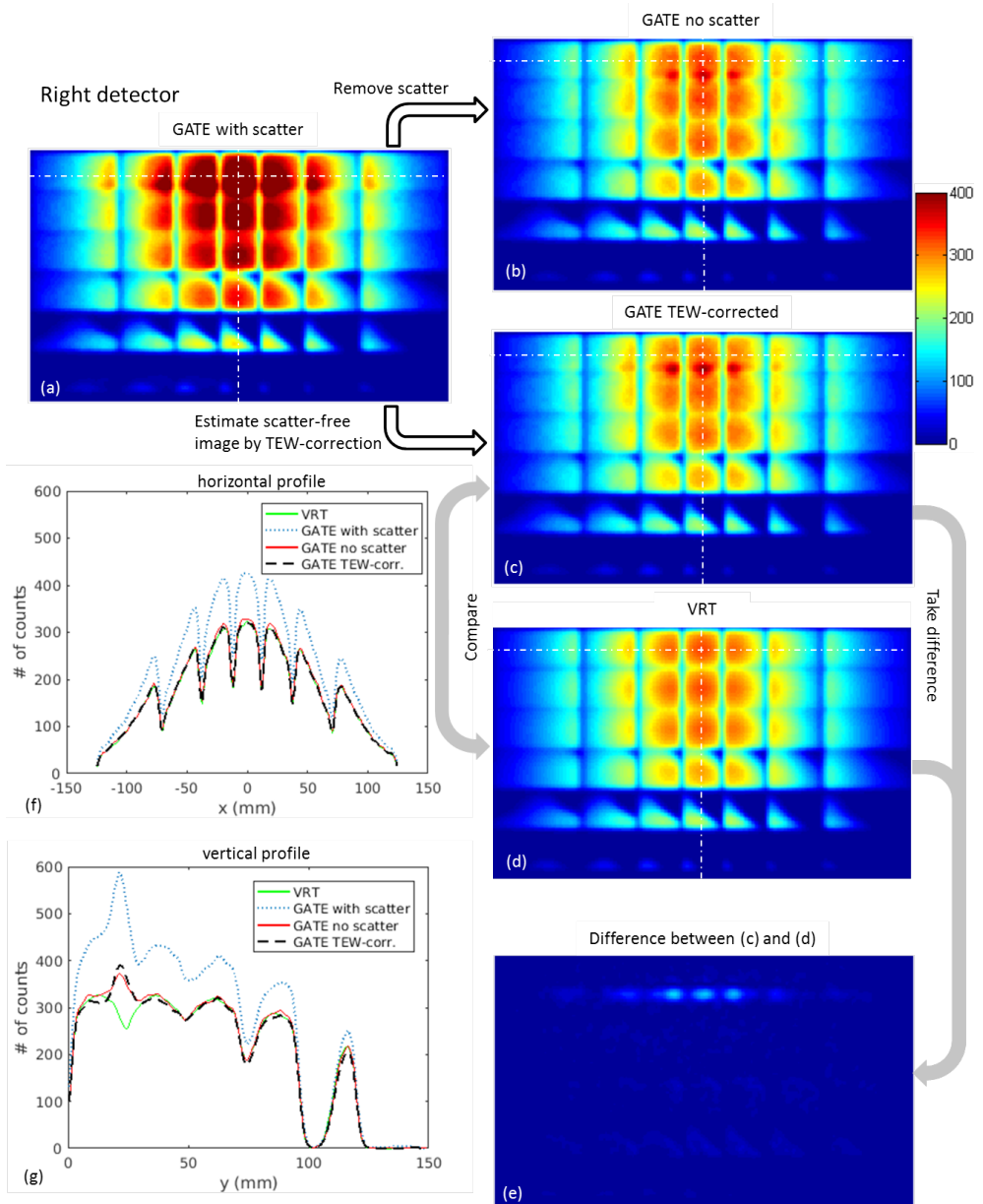
Figure 3-13 Right detector projection images of the GATE simulated XCAT phantom with 1300 mL-breast. (a) Full projection with scatter and torso signal; (b) projection without scatter (treated as ground truth for photons scattered in the phantom and collimator); (c) scatter-corrected projection using the TEW method; (d) the projection obtained with VRT (only breast phantom); (e) difference between VRT-generated projection and scatter-corrected projection. (f) and (g) are the horizontal and vertical profiles marked in white in (a) – (d).

Table 3-4 Comparison of projection images

Projection image	Difference	
	NRMSE	Max. Diff.
400 mL left	1.08 %	5.26 %
400 mL right	2.44 %	15.08 %
1300 mL left	1.37 %	8.53 %
1300 mL right	2.43 %	32.85 %

Gaussian filter of 3 mm FWHM. Visually, reconstructions from GATE-simulated projections with TEW correction applied and from VRT-generated noisy projections appear very similar. The profiles between the two green lines in (a) and (b) are shown and compared in (c). Similar images from different noise realizations can be found in the appendix in Figure 3-A1.

As noisy images cannot be directly compared as was done for noiseless projections, we also assess noise and contrast in reconstructed images for ten sets of GATE-simulated projections with TEW-correction and ten noise realisations of VRT-simulated projections. The average contrast and noise of the lesions and backgrounds are provided in Table 3-5, as well as the standard deviation over different noise realizations. There is no significant difference in the numbers for the different methods.

3.4   Discussion

From the PSF profiles in Figure 3-6 and Figure 3-7 and the differences displayed in Table 3-2, it is clear that the PSFs from GATE and VRT (at 1/8 mm fine voxel) agree very closely. Note that initially when the fine voxel size in VRT is decreased, the PSFs acquired by GATE and VRT become more similar as one would expect. However, for voxel sizes below 1/8 mm the difference goes up slightly. From this, we conclude that for such very small voxel sizes the difference between GATE and VRT is not dominated by the discretization effect anymore and thus we deemed a fine voxel size of 1/8 mm to be sufficiently small. We do not have an exact explanation

Table 3-5 Reconstructed image comparison

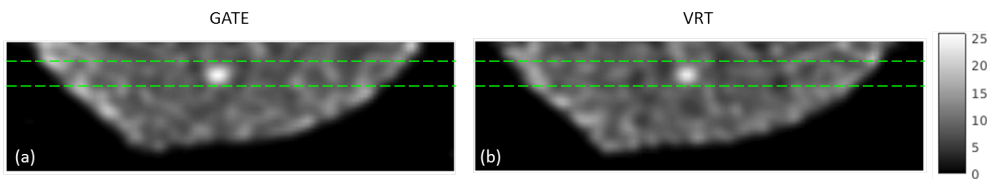|	GATE	VRT
contrast	1.40±0.24	1.36±0.19
noise	0.244±0.011	0.203±0.016

Figure 3-14 Slices through MLEM reconstructed images with 20 iterations used obtained with the two methods. Images are obtained from (a) GATE-simulated projections with TEW scatter correction used in reconstruction, (b) VRT-generated noisy projections.

for the increasing difference between GATE and VRT for smaller voxel sizes. The small residue differences (on average 0.14%) may be caused by (i) the reference GATE simulation not being completely noiseless, or (ii) photons that scattered in collimator or detector.

Together with the 1/8 mm fine voxel size which is necessary for simulation accuracy, we find that a coarse voxel size of 2 mm led to the highest simulation speed. The optimal coarse voxel size strikes a good balance between two extremes. When it is too large, the number of mixed voxels increases and thus much more rays have to be tracked on the fine collimator grid: in the extreme situation in which the whole collimator plate is made out of a single coarse voxel, VRT will have to look into the fine volume for every photon path and the dual-grid method is actually not used. On the other hand, if the coarse voxel size is very small, raytracing on the coarse voxel grid itself is already slow and completely dominates simulation time. We have shown that with the optimal coarse voxel size, VRT could reach the same difference level from the reference PSFs 330 times faster than accelerated GATE or 28600 times faster than a full GATE MCS.

Note that the VRT voxel size combination of 1/8 mm and 2 mm is 'optimal' for the current collimator and detector geometry. For a different collimator or scanner, there might be better combinations. However, from our experience, as long as the thickness of the collimator/shielding plate is an integer multiple of the coarse voxel size, and the pinhole diameter does not change very much, the optimal dual grid setting should stay the same. Furthermore, up to now, we have only tried a dual-grid collimator representation. It is possible to use full octree-structure grids to represent the collimator which may lead to higher time-efficiencies. However, finding the optimal setting for a multi-grid approach is beyond the scope of this research, since the time-efficiency for VRT with the current setting is already good enough for us as with these settings, as noiseless system matrices could be generated in minutes. Compared with other raytracing SPECT simulators in which collimators are defined by analytical shapes (Feng *et al.*, 2010; Goorden *et al.*, 2011; C. M. Li *et al.*, 2009; Schramm *et al.*, 2003; Smith *et al.*, 1997), the advantage of VRT is that geometries that are hard to describe analytically can be easily implemented. Furthermore, a design drawing of a collimator can be directly voxelized to a volume that can be used in raytracing. The disadvantage is that it requires some trial and error to determine the voxel size (combination) that provides a satisfactory discretization error and acceptable computational speed.

While the PSF simulations show that in principle VRT is an accurate and fast simulator, they do not consider scattered gamma photons from the human body which can play a major role in clinical imaging and is ignored in VRT. In real scanners, projection images contain scattered photons which are usually corrected for prior to reconstruction or in the iterative reconstruction process. The TEW method is a simple and popular scatter estimation method. Thus, to accurately predict the performance of a real MP-MBT system, the projection images from VRT are supposed to closely resemble TEW-corrected images. In the projection images and profiles in Figure 9 and Figure 10, we show that for the 400 mL-breast, TEW-corrected GATE projections and VRT projections are very similar, and an NRMSE of about 1% is found. However, for the 1300 mL-breast, a discrepancy is encountered. A comparison with scatter-free GATE projections

reveals that the discrepancy is not due to scatter (as TEW-corrected GATE images very closely resemble scatter-free GATE images). In Figure 3-15(a), a zoom-in view of Figure 3-1, it can be seen that some gamma photons from the liver directly reach the right detector through the first row of pinholes. We checked this by removing the torso phantom and acquiring the same projection image as in Figure 3-13. In the vertical profile of this projection, shown in Figure 3-15(b), the VRT generated profile agrees very well with the scatter-corrected GATE-generated profile. On the left detector, such an issue is not observed as there is no organ on the cranial side of the body that has 99mTc-Sestamibi uptake as high as the liver. Note that in principle VRT can simulate direct activity from the torso so this finding does not disqualify VRT as an accurate simulator of MP-MBT. However, in this paper we only simulate photons originating from the breast. Thus, the lesson learnt is that when designing such a system one has to consider direct paths from the torso to the detector, and these have either to be taken into account in the simulator or the geometry has to be adapted as to avoid these paths.

As stated above, neglecting Compton scattering in VRT is acceptable with our specified MP-MBT geometry as Compton-scattered photons can be corrected for with a TEW method even though we use a conventional NaI(Tl) gamma detector with a moderate energy resolution of 9%. This minor contribution of Compton scattering to breast images agrees with an earlier work on planar compressed breast imaging with a parallel hole collimator (Hruska & O'Connor, 2008a) although other papers have indicated different results (Pani *et al.*, 1998; Williams *et al.*, 2003). The reason for the rather small ratio of scattered photons in the photopeak despite the high tracer uptake in the heart and liver probably lies in the fact that gamma photons from the torso have to be scattered by a rather large angle in order to be redirected in the direction of the gamma detector. Large-angle scatter is generally associated with a large energy loss and thus the majority of these scattered photons can be rejected because they are detected outside the photopeak window. Although in many studies nowadays semiconductor detectors are used, it is shown here that the energy resolution of NaI(Tl) is sufficient for this application.
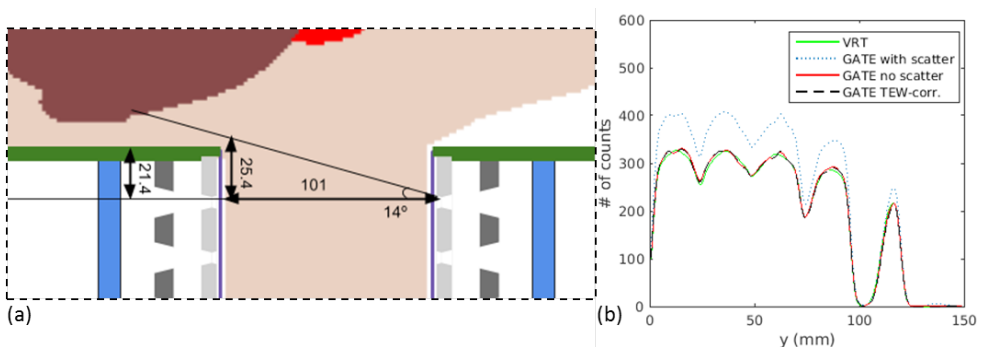
Figure 3-15 (a) An enlarged view of the MP-MBT system for the 1300 mL breast phantom (see Figure 3-1); through the first row of pinholes, gamma photons from part of the liver can directly be detected by the right detector. (b) A vertical profile of the right detector projection (the same as Figure 3-13(g)) in which the torso phantom is removed from GATE simulation; the mismatch in VRT and the scatter-corrected GATE projections disappears.

Note that the fact that VRT can accurately simulate TEW-corrected projections means that we can correct for the bias caused by scatter. However, there is another aspect to scatter that VRT cannot correct for which is the added noise level due to the scattered photons. Therefore, we also simulated reconstructed images based on either GATE-simulated projection or VRT-generated images. Visual inspection as well as contrast-noise characteristics show that images obtained with both methods were very similar, further indicating that VRT can be used to predict the quality of simulated images. As computation time for such images is considerable we only simulated reconstructed images for the 400 ml breast size, but as the scatter fraction is similar for the larger breast our results indicate that the neglect of scatter in VRT is also acceptable for these larger breast sizes. However, in the case larger breast simulation, direct paths from liver to detector either have to be modelled in image reconstruction or prevented by a slight change in design. Note that on the left side of the reconstructed breast images from GATE, there is a slight increase of signal compared to VRT images. We believe that such bias can be removed by tuning the size of the scatter windows and the amount of blurring of the scatter projections. This, however, is beyond the scope of this paper because we have just tested one setting of these parameters, but may be the subject of future research. We chose TEW for scatter correction because of its simplicity and because it is one of the most commonly used approaches in the clinic (Zaidi et al 2004, Hutton et al 2011). There are of course other more advanced scatter estimation techniques (Hutton et al 2011), which can also be implemented in practice. However, in this paper, we focus on proving that VRT can be used to generate realistic simulated images and testing out different scatter correction techniques is beyond the scope of this paper.

3.5   Conclusion

VRT can accurately simulate the proposed MP-MBT system with more than four orders of magnitude better time-efficiency than full MCS. Ignoring scatter in VRT is feasible because the amount of scatter in the photopeak is limited in our pinhole collimator-based MP-MBT geometry and can thus be corrected. However, direct gamma photon paths between liver and gamma detector can exist for large breast sizes and have to be carefully considered in design and simulation. VRT can be very useful in evaluating geometries for MP-MBT.

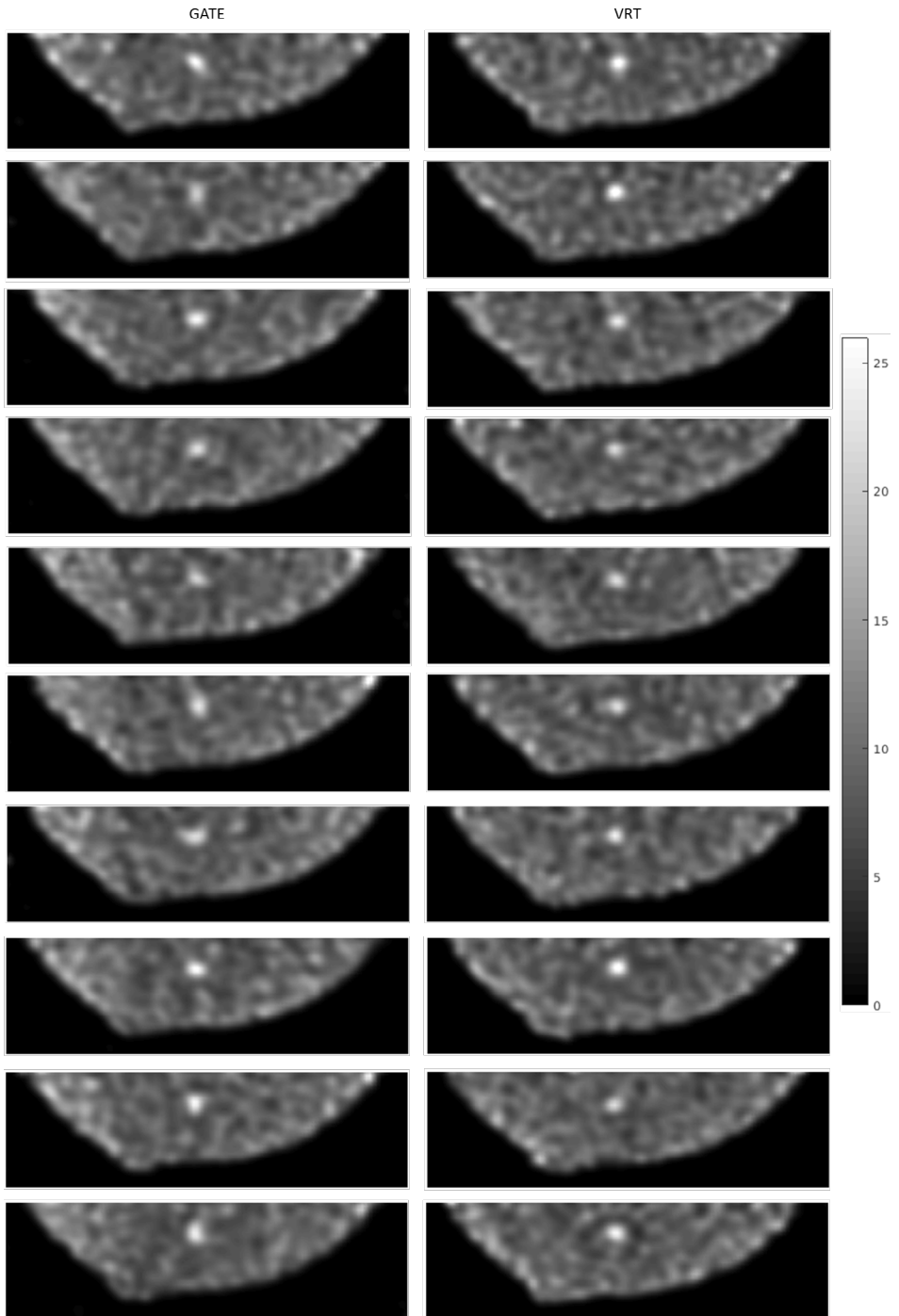## 3.6   Acknowledgement

Appendix 3.A Figure

Figure 3-A1 Reconstructed images similar as in Figure 3-14 for all simulated noise realisations.

Chapter 4

Non-diverging analytical expression for the sensitivity of converging SPECT collimators

Abstract

Accurate analytical expressions for collimator resolution and sensitivity are important tools in the optimization of SPECT systems. However, presently known expressions for the sensitivity of converging collimators either diverge near the focal point or focal line(s), or are only valid on the collimator axis. As a result, these expressions are unsuitable to calculate volumetric sensitivity for e.g. short-focal length collimators that focus inside the object to enhance sensitivity. To also enable collimator optimization for these geometries, we here present non-diverging sensitivity formulas for astigmatic, cone beam and fan beam collimators that are applicable over the full collimator's field-of-view. The sensitivity was calculated by integrating previously derived collimator response functions over the full detector surface. Contrary to common approximations, the varying solid angle subtended by different detector pixels was fully taken into account which results in a closed-form non-diverging formula for the sensitivity. We validated these expressions using ray-tracing simulations of a fan beam and an astigmatic cone beam collimator and found close agreement between the simulations and the sensitivity expression. The largest differences with the simulation were found close to the collimator, where sensitivity depends on the exact placement of holes and septa, while our expression represents an average over all possible placements as is common practice for analytical sensitivity expressions. We checked that average differences between the analytical expression and simulations reduced to less than 1% of the maximum sensitivity when we averaged our simulations over different septa locations. Moreover, we found that our new expression reduced to the traditional diverging formula under certain assumptions. Therefore, the newly derived sensitivity expression may enable the optimization of converging collimators for a wide range of applications, in particular when the focal area is close to, or in, the object of interest.

4.1   Introduction

The use of converging collimators in Single Photon Emission Computed Tomography (SPECT) has already been proposed since the 1980s (Jaszczak *et al.*, 1979; Tsui *et al.*, 1986; Jaszczak *et al.*, 1986, 1988; Gullberg *et al.*, 1991a; Gullberg *et al.*, 1991b). Such converging collimators, in which the hole's axes converge to a focal line (fan beam), a focal point (cone beam), or multiple focal lines (astigmatic), are advantageous for increasing photon yield or sensitivity over that of parallel hole collimators if the dimensions of the target object or organ are smaller than those of the gamma detector. Additionally, combinations of different converging collimators, e.g. combined half-cone beam and fan beam collimation have been investigated for high-sensitivity SPECT (Li *et al.*, 1996; Kamphuis and Beekman, 1998; Beekman *et al.*, 1998; Ter-Antonyan *et al.*, 2009). Because the sensitivity of converging collimators is highest near the focal line(s) or point, various researchers have proposed to use short focal length cone beam collimators with focus inside the object of interest, e.g. Hawman and Haines (1994); Walrand *et al.* (2002); Park *et al.* (2003,

2005); van Roosmalen *et al.* (2015); **Chapter 2**. The increased sensitivity due to focusing inside the object may also reduce noise in reconstructed images induced by attenuation as was shown by Kijewski *et al.* (1997) and may benefit SPECT systems equipped with transmission sources (SPECT/Transmission Computed Tomography (TCT) systems) by increasing the number of transmission counts. These systems based on fan beam collimators can have transmission line or point sources at the focal line (Kemp *et al.*, 1995; Beekman *et al.*, 1998), or use virtual point sources at the focal point of a cone beam collimator (Manglos *et al.*, 1992; Beekman, 2001).

An important tool in SPECT and SPECT/TCT system design is the use of accurate analytical expressions for collimator resolution and sensitivity. However, common expressions for the sensitivity of converging collimators (Metz *et al.*, 1980; Tsui and Gullberg, 1990) inappropriately diverge near the collimator's focus. Moreover, the divergence scales with $1/r^n$, with r being the distance from the focus and $n = 1$ for fan beam and $n = 2$ for cone beam collimators, making the expressions non-integrable around the focus. Thus, when calculating volumetric collimator sensitivity over a region containing the focus, one cannot circumvent the singularity at the focus by taking points just outside of the focus location. This is particularly problematic for designing systems that exploit the increased sensitivity near the focus such as the short-focal-length collimator geometries mentioned above.

To circumvent the issue of diverging analytical expressions, other methods for determining the sensitivity have been used in optimization studies. For example measurements on physical collimators (Jaszczak *et al.*, 1988; Li *et al.*, 1996), extensive Monte Carlo or raytracing simulations (Jaszczak *et al.*, 1986) can give accurate estimates. However, these methods are computationally expensive, and do thus not allow for quick evaluation of a large number of design parameters, or fast analytical optimization based on the expressions themselves. At the same time, analytical expressions have often been used for optimizing other collimator types, e.g. Lowe *et al.* (2002); Gunter (2004); Rentmeester *et al.* (2007); Goorden *et al.* (2008); Weinmann *et al.* (2009), and for an overview see Van Audenhaege *et al.* (2015). Therefore, the availability of accurate non-diverging expressions is expected to enable easier and faster optimization of converging collimators for a wide range of geometries.

Non-diverging expressions were previously derived by Accorsi and Metzler (2006), but only for the on-axis sensitivity of converging collimators. In this work, we present new sensitivity formulas that are valid over the whole field-of view, and we validate these using raytracing software.

4.2   Methods

4.2.1   General collimator theory
We start here with introducing the parameters and with repeating the standard collimator theory on which our derivation is based. The collimator model and some of the parameters describing it are shown in Figure 4-1. Assuming the z-axis to be perpendicular to the detector, we define F_x, F_y, d_x, d_y, t_x, and t_y to be the focal lengths, hole widths and septal thickness in x- and y-directions
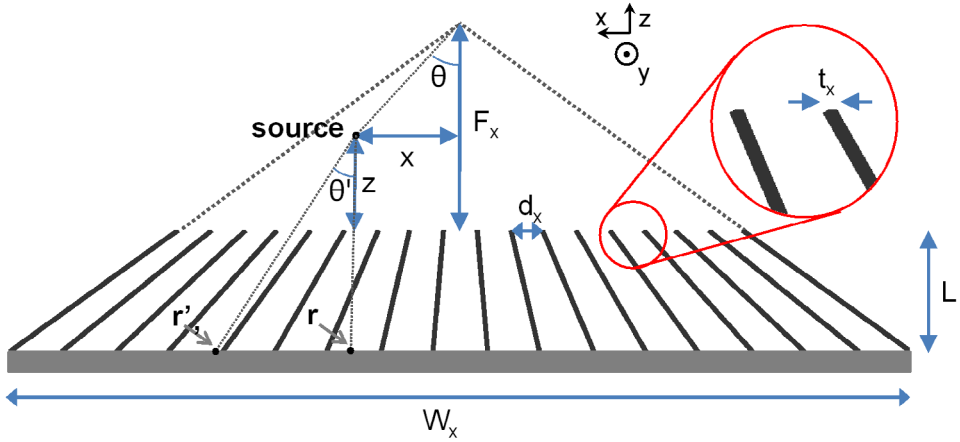
Figure 4-1 Schematic cross-section through a converging collimator with parameters used in this paper indicated.

respectively while L is the collimator thickness. Both the hole widths and septal widths are defined at the object side of the collimator. Along the z-direction they both increase by the same factor which depends on the amount of focusing. We assume that the detector has a rectangular shape and that it extends from $x = -W_x/2$ to $x = W_x/2$ and from $y = -W_y/2$ to $y = W_y/2$.

Our derivation starts from the general collimator theory described in Metz *et al.* (1980) for parallel holes, which was extended in Tsui and Gullberg (1990) to cone beam collimators. Here we adopt the notation of the latter paper while throughout our expression we also allow for fan beam and astigmatic collimators.

We look at the response to a point source located at (x, y, z). The perpendicular projection of the source on the detector plane is represented by $\mathbf{r} = (x, y)$. Note that this is a two-dimensional coordinate as it represents a point on the detector. The following equation describes the fluence ϕ [m^{-2}] of photons detected at point r' = (x', y') on the detector,

$$\phi(\mathbf{r'}, \mathbf{r}, z) = \frac{k}{4\pi(z+L)^2} \cos^3 \theta' A(\mathbf{r'}, \mathbf{r}, z) \qquad (4\text{-}1)$$

where k [m^{-2}] is a proportionality factor which will be discussed later and $A(\mathbf{r'}, \mathbf{r}, z)$ [m^2] is the aperture function of the collimator at point $\mathbf{r'}$ on the detector. Moreover, in this expression, θ' is the angle between the z-axis and the vector connecting the point source with the point $\mathbf{r'}$ on the detector as indicated in Figure 4-1. It can thus be written as

$$\cos \theta' = \frac{z+L}{\sqrt{(z+L)^2 + |\mathbf{r'} - \mathbf{r}|^2}}. \qquad (4\text{-}2)$$

The collimator aperture function $A(\mathbf{r'}, \mathbf{r}, z)$ is determined from the aperture functions of a single hole $a_f(\mathbf{r''})$ and $a_b(\mathbf{r''})$ respectively at the front and at the back of the collimator, which are one for lateral positions $\mathbf{r''} = (x'', y'')$ inside the collimator hole and zero outside of the hole. If one projects the front and back apertures from the source position onto the detector then the

size of the overlap between these projections determines the fraction of photons that can pass through the collimator hole. Now the common way to calculate the sensitivity, is to continuously translate a single hole over the detector to arrive at an average sensitivity which does not depend on the exact position of the septa. For the general case of astigmatic collimators with holes on a lattice it was shown that $A(\mathbf{r}', \mathbf{r}, z)$ can be written in the following way (Tsui and Gullberg, 1990; Formiconi, 1998)

$$A(\mathbf{r}', \mathbf{r}, z) = \int_{-\infty}^{\infty} a_f(-\boldsymbol{\sigma}) a_f\left(\mathbf{r}_T(\mathbf{r}', \mathbf{r}, z) - \boldsymbol{\sigma}\right) d\boldsymbol{\sigma}, \tag{4-3}$$

where $\boldsymbol{\sigma} = (\sigma_x, \sigma_y)$, $\mathbf{r}_T(\mathbf{r}', \mathbf{r}, z) = \left(x_T(x, x', z), y_T(y, y', z)\right)$ and

$$x_T(x, x', z) = \frac{L(F_x - z)}{(F_x + L)(z + L)} x' - \frac{L}{z + L} x, \tag{4-4}$$

$$y_T(y, y', z) = \frac{L(F_y - z)}{(F_y + L)(z + L)} y' - \frac{L}{z + L} y. \tag{4-5}$$

Note that these equations thus average out the details of the exact location of the individual septa and holes (Tsui and Gullberg, 1990; Formiconi, 1998). Here σ represents a shift of the hole parallel to the detector plane, to average the response over all possible hole locations. Moreover, $\mathbf{r}_T$ represents the vector on the collimator surface between the line from the focus to the point $\mathbf{r}'$ on the detector and the line from the source to $\mathbf{r}'$ (see Figure 4-A1 in the appendix for an illustration).

In our derivation we assume rectangular holes (in the discussion we come back to other hole shapes) and one thus has an aperture function $a_f(\boldsymbol{\sigma}) = 1$ if $|\sigma_x| < d_x/2$ and $|\sigma_y| < d_y/2$. The collimator's aperture function can then be calculated and it reads

$$A(\mathbf{r}', \mathbf{r}, z) = \left(d_x - |x_T|\right)\left(d_y - |y_T|\right), \tag{4-6}$$

for $|x_T| < d_x$ and $|y_T| < d_y$ and 0 otherwise. To determine the sensitivity, the flux has to be integrated over the detector plane. One can show that in order to arrive at a physically meaningful sensitivity, one has to set the proportionality constant $k^{-1} = (d_x + t_x)(d_y + t_y)$ (Tsui and Gullberg, 1990). With these definitions, the flux in (4-1) is fully defined, and the sensitivity is given by

$$\begin{aligned} S &= \int_{-W_x/2}^{W_x/2} \int_{-W_y/2}^{W_y/2} dx' dy' \phi(\mathbf{r}', \mathbf{r}, z) \\ &= \frac{F_x + L}{|F_x - z|} \frac{F_y + L}{|F_y - z|} \frac{1}{L^2 \, 4\pi(d_x + t_x)(d_y + t_y)} \cdot \\ &\quad \int_{\chi_{-1}}^{\chi_1} \int_{\xi_{-1}}^{\xi_1} dx_T \, dy_T \, (d_x - |x_T|)(d_y - |y_T|) \cos^3 \theta' \end{aligned} \tag{4-7}$$

Here, the integration limits χ_{-1}, χ_1, ξ_{-1} and ξ_1 can be calculated by

$$\chi_i = \min\left\{ \max\left[-d_x, -\frac{L|x|}{L+z} + \frac{1}{2} i W_x \left| \frac{L(F_x - z)}{(F_x + L)(L + z)} \right| \right], d_x \right\}, \tag{4-8}$$

$$\xi_i = \min\left\{\max\left[-d_y, -\frac{L|y|}{L+z} + \frac{1}{2}iW_y\left|\frac{L(F_y - z)}{(F_y + L)(L+z)}\right|\right], d_y\right\}. \tag{4-9}$$

Note that the integration limits are coordinates defined on the front surface of the collimator, where $\mathbf{r}_T$ was defined (see Figure 4-A1). The response that is being integrated is for a single moving hole. Therefore, the limits in (4-8) and (4-9) are usually from $-d_x$ to d_x (or $-d_y$ to d_y), except when the hole is partly over the edge of the finite detector, then the integration range becomes smaller.

4.2.2   Conventional diverging expression

Now the usual approach is to approximate θ' with θ (the angle between the z-axis and the line from the focus to $\mathbf{r}$, see Figure 4-1). This approximation is based on the assumption that the detector response to a point source is narrow, i.e. gamma photons from the source can only reach the detector through a few holes. In this case the $\cos^3\theta'$ can be approximated by $\cos^3\theta$ in (4-7) and taken out of the integral as it is now a constant. Furthermore, in these traditional derivations the finite detector size is not taken into account. Under these assumptions, the integral is straightforward to perform and one finds the usual diverging formula for sensitivity, c.f. Moyer (1974); Jaszczak *et al.* (1986) or Formiconi (1998)

$$S_{\text{div}} = \cos^3\theta \frac{1}{4\pi} \frac{F_x + L}{|F_x - z|} \frac{F_y + L}{|F_y - z|} \frac{d_x^2 d_y^2}{L^2(d_x + t_x)(d_y + t_y)}. \tag{4-10}$$

Using basic trigonometry one can write $\cos\theta = 1/\sqrt{1 + x^2/(F_x - z)^2 + y^2/(F_y - z)^2}$

4.2.3   Non-diverging expression

The reason that the common sensitivity expressions diverge near the focal point / lines is due to the fact that the assumptions stated in section 4.2.2 do not hold close to the focal point, as close to the focal point many holes "see" the source and the response is not narrow, see Figure 4-2.
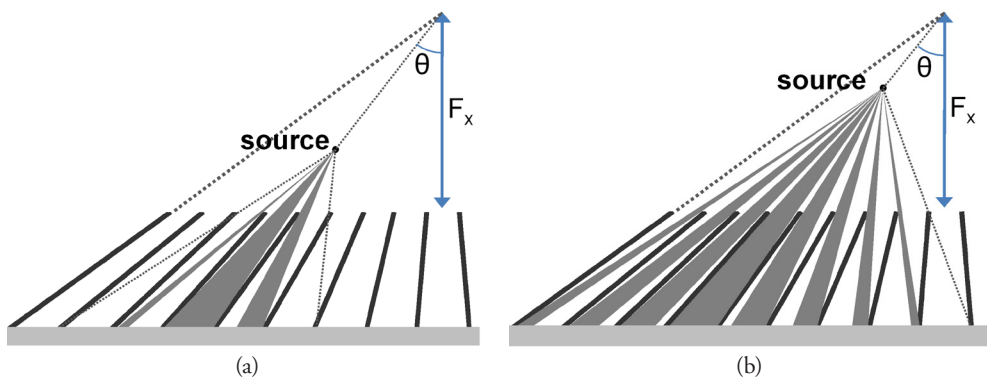
Figure 4-2 Schematic representation of the holes that contribute to the sensitivity for two different point source locations. Dotted lines illustrate paths that are blocked by the collimator. (a) Point source located away from the focus resulting in a narrow detector response to which only a few holes contribute. (b) Point source located close to the focus having a wide detector response as paths from the source can reach the detector through many holes.

Thus, for these non-narrow responses one cannot approximate θ' with θ and the $\cos^3 \theta'$ term has to be included inside the integral as it varies over the detector. In (4-2) we already provided an exact expression for $\cos \theta'$ in terms of $\mathbf{r}$ and $\mathbf{r'}$, which can be substituted in (4-7).

Moreover, near the focal point or line the finite detector size starts to play a role; when a source is placed in the focal point all holes transmit gamma photons from the source and thus the sensitivity reduces to the solid angle subtended by the detector plane, corrected for the fact that no signal is detected underneath the septa. As the solid angle of a finite detector is usually significantly different from that of an infinite detector, the detector size should play a role for all points in a region around the focus.

Therefore, to arrive at a realistic expression for sensitivity which is also valid near the collimator's focus, we have to evaluate the full integral of (4-7) without any approximation. In principle, this evaluation consists of performing standard integrals, that can e.g. be found in textbooks like Gradshteyn and Ryzhik (2014). Note that the integration limits in (4-7) are complicated expressions given in (4-8) and (4-9), so especially the second integration is quite complex involving many terms. Therefore, the resulting expression becomes very complicated and very lengthy and we had to perform extensive simplification in order to arrive at a tractable form that can be presented in a paper and that other researchers can incorporate into their collimator optimization code. In the supplementary information[1] we provide the results of the first integration and the simplification applied to this intermediate result. The mentioned simplifications consisted of exact algebraic manipulation of the (intermediate) expressions, in order to arrive at a representable formula, but they did not involve any approximations. For example, we identified several frequently occurring sub-expressions which could be replaced by a single variable or function. All algebraic manipulations of expressions were supported by the computer program Mathematica (Wolfram Research Inc.). The Mathematica file is available in the supplementary information.

4.2.4 Validation

We validate the results using our raytracing software that we developed and validated with Monte Carlo simulations (Wang *et al.*, 2017; **Chapter 3**). This raytracing code uses a voxel based model (0.05 mm voxels in this paper) of the collimator, where each voxel consists of either air, or collimator material. The voxel size was chosen to be sufficiently small to accurately model the septa, i.e. a small test gave sensitivity differences of a few percent compared to results with much smaller voxels. The software determines the path length through materials from the source to each of the 36 million detector pixels with a Siddon-like raytracing algorithm. The algorithm follows a ray from source to a detector pixel through the collimator. In every voxel the path length of the ray through the voxel is calculated and multiplied by the linear attenuation coefficient. We use Siddon's efficient algorithm to compute this path length (Siddon, 1985). The accumulated probability that the ray is attenuated in the collimator combined with a geometrical factor gives the final probability that a photon emitted from the source is detected at this specific pixel. The

1   The supplementary information is provided with the published paper on which this chapter is based and can be accessed at https://doi.org/10.1088/1361-6560/aa6646

geometrical factor is the solid angle of the pixel extended towards the source (i.e. the probability that the pixel would detect gamma photons from the source if no collimator would be present). We modelled the detector with 0.05 x 0.05 mm pixels, to accurately describe the exact response of the holes, without suffering from discretization errors.

For testing our expression, modelling of the detector response has been turned off as is common. To validate the collimator response formula, the geometrical response of the collimator was calculated without modelling penetration of gamma rays through the septa. Therefore, this is initially also turned off in our raytracing software to first test for agreement in this ideal case. As in our derivation, holes are assumed to be rectangular in the simulation. We consider two collimators in our validation. The first is a fan beam collimator with $d_x = d_y = 1.4$ mm, $t_x = t_y = 0.2$ mm, $L = 27$ mm, $F_x = 45$ mm. For fan beam collimators, F_y is set to ∞. The second collimator we use for validation is an astigmatic cone beam collimator with $d_x = 1.4$ mm, $d_y = 1.1$ mm, $t_x = 0.2$ mm, $t_y = 0.3$ mm, $L = 27$ mm, $F_x = 45$ mm and $F_y = 60$ mm. In both cases the detector is assumed to be 300 mm by 300 mm.

It is expected that close to the collimator the sensitivity will strongly depend on the precise location of the septa and holes. However, as it is generally undesirable to have complicated sensitivity expressions containing the exact locations of the septa, we based the analytical derivation on averaging over all possible configurations, as is common to do. To be able to validate the expression against this assumption, we shifted the septa in our voxelized collimator model in 10 steps of 0.16 mm, for both x and y directions for the fan beam example. For the cone beam example we use steps of 0.16 and 0.14 mm for x and y respectively. This results in 100 unique collimator configurations, which were each simulated using our raytracer. The average sensitivity is then reported, as are the results of a single configuration to illustrate the difference.

Moreover, we investigated if we can use the usual approach of incorporating septal penetration by an effective hole length, $L_e = L - 2/\mu$ (Mather, 1957; Moyer, 1974). To test how accurate this approximation is, we replace L by L_e in our formulas and include penetration in our raytracing code for the same collimators as described above. We assume tungsten septa with $\mu = 3.39$ mm^{-1} for 140 keV gamma rays.

4.2.4.1   *Volumetric Sensitivity*
To see the importance of the new expressions for volumetric sensitivity calculations we test an example loosely based on the brain SPECT system of Park *et al.* (2005). We assume a 300 mm by 300 mm detector with a collimator with $L = 24$ mm, $d_x = d_y = 1.1$ mm and $t_x = t_y = 0.16$ mm. The mean sensitivity is calculated for a sphere with a diameter of 200 mm, located 50 mm from the collimator surface (mimicking a 150 mm radius of rotation). We will evaluate the sensitivity for a range of focal lengths from 150 mm (focus in the centre of the sphere) till 400 mm (focus outside sphere).

4.3 Results

4.3.1 Analytical expression

After integrating (4-7) and extensive simplification, we arrived at the following closed-form expression for the sensitivity

$$S = \frac{L^2}{4\pi} \frac{1}{d_x + t_x} \frac{1}{d_y + t_y} \frac{|F_x - z|}{F_x + L} \frac{|F_y - z|}{F_y + L} \sum_{i=-1}^{1} \sum_{j=-1}^{1} S_{i,j} \tag{4-11}$$

The term $S_{i,j}$ is given by

$$S_{i,j} = (-1)^{i+j} \left(2 - |i|\right)\left(2 - |j|\right)\left(i - (1+i)U\left(\chi_1\right)\right)\left(j - (1+j)U(\xi_1)\right)$$

$$\left[-\sqrt{1 + b_x^2(i) + b_y^2(j)} + a_x(i)a_y(j)\arctan\left(\frac{b_x(i)b_y(j)}{\sqrt{1 + b_x^2(i) + b_y^2(j)}}\right) \right.$$

$$-a_x(i)\ln\left(-b_x(i) + \sqrt{1 + b_x^2(i) + b_y^2(j)}\right)$$

$$\left. -a_y(j)\ln\left(-b_y(j) + \sqrt{1 + b_x^2(i) + b_y^2(j)}\right)\right] \tag{4-12}$$

where U denotes the unit step function ($U(x) = 1$ for $x > 0$ and $U(x) = 0$ for $x \le 0$). Furthermore, the constants a_x, a_y, b_x and b_y read (for $i = -1, 1$ and $j = -1, 1$)

$$a_x(i) = \frac{F_x + L}{F_x - z} \frac{d_x}{L} \text{sign}(\chi_i) + \frac{|x|}{F_x - z}, \quad a_y(j) = \frac{F_y + L}{F_y - z} \frac{d_y}{L} \text{sign}(\xi_j) + \frac{|y|}{F_y - z}, \tag{4-13}$$

$$b_x(i) = \frac{F_x + L}{F_x - z} \frac{\chi_i}{L} + \frac{|x|}{F_x - z}, \qquad b_y(j) = \frac{F_y + L}{F_y - z} \frac{\xi_j}{L} + \frac{|y|}{F_y - z} \tag{4-14}$$

while for $i = 0$ respectively $j = 0$, we have

$$a_x(0) = b_x(0) = |x|/(F_x - z), \qquad a_y(0) = b_y(0) = |y|/(F_y - z). \tag{4-15}$$

The finite detector size is incorporated in χ_i and ξ_j which were defined previously in (4-8) and (4-9). Although this is still a rather complicated expression, it can easily be incorporated in a computer program to quickly calculate the sensitivity for different collimators in e.g. an optimization study.

4.3.2 Special cases

It is important to show that under the right assumptions the well known and previously published formulas can be recovered. The traditional diverging formula was derived under the assumption that the detector has an infinite size and that $\theta' \approx \theta$ (i.e. the detector response is narrow, see Figure 4-2 and section 4.2.3). For an infinite detector, $W_x = W_y = 1$ and this gives $\chi_i = id_x$ and $\chi_i = id_y$. Furthermore, we assume that $|F_x - z| \gg d_x(F_x + L)/L$ and $|F_y - z| \gg d_y(F_y + L)/L$ This corresponds to assuming that the vertical distance from the focal point/line ($|F_x-z|$), is much larger than the back projected size of a hole ($d_x(F_x + L)/L$) along the same vertical axis. First order expansion in $d_x(F_x + L)/(L|F_x - z|)$ and $d_y(F_y + L)/(L|F_y - z|)$ of (4-11) gives

$$S \approx \frac{1}{4\pi} \frac{F_x + L}{|F_x - z|} \frac{F_y + L}{|F_y - z|} \frac{d_x^2 d_y^2}{L^2 (d_x + t_x)(d_y + t_y)} \left(\left(\frac{x}{F_x - z} \right)^2 + \left(\frac{y}{F_y - z} \right)^2 + 1 \right)^{-\frac{3}{2}}. \quad (4\text{-}16)$$

Using the expression for cos θ, defined in section 4.2.2 we can rewrite this as (4-10) (duplicated here for convenience)

$$S_{\text{div}} = \cos^3 \theta \frac{1}{4\pi} \frac{F_x + L}{|F_x - z|} \frac{F_y + L}{|F_y - z|} \frac{d_x^2 d_y^2}{L^2 (d_x + t_x)(d_y + t_y)}.$$

It is also of interest to consider sensitivity at the focal point of a cone beam collimator. This is done by first setting $x = y = 0$, and $F_y = F_x$ and then taking the limit $z \to F_x$. Setting $x = y = 0$ means the first term with $|x|$ and $|y|$ respectively in χ_i and ξ_i drops, and the second term drops out of $a_x(i)$, $a_y(j)$, $b_x(i)$ and $b_y(j)$ in (4-13), (4-14) and $a_x(0) = a_y(0) = b_x(0) = b_y(0) = 0$. The $a_x(i)$, $a_y(j)$, $b_x(i)$ and $b_y(j)$ terms diverge for $i, j \neq 0$ in the limit $F_x - z \to 0$, but the divergence is cancelled by the $|F_x - z|$ from the pre-factor in (4-11). All the terms with either $i = 0$ or $j = 0$ are 0 in (4-12), leaving us with 4 equal terms that add up to

$$S_{\text{foc}} = \frac{d_x d_y}{\pi (d_x + t_x)(d_y + t_y)} \arctan \left(\frac{W_x W_y}{2 (F_x + L) \sqrt{4 (F_x + L)^2 + W_x^2 + W_y^2}} \right), \quad (4\text{-}17)$$

which is just the solid angle of the detector corrected for the presence of septa (cf. (29) from Accorsi and Metzler (2006)). Note that for an infinite detector the arctan term becomes arctan(∞) = $\pi/2$ and so the sensitivity reduces to $d_x d_y /(2(d_x + t_x)(d_y + t_y))$ which in the limit of septal thickness going to 0, reduces to 1/2 as expected for a single infinite detector.
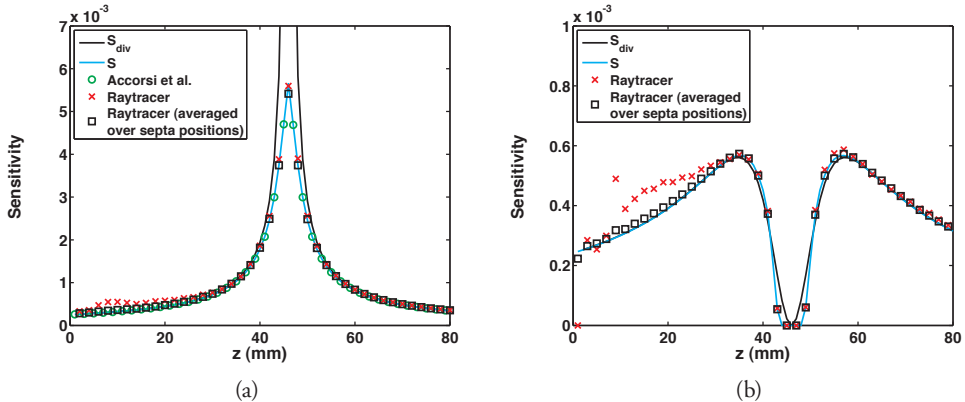
Figure 4-3 Comparison of analytically calculated sensitivity (cyan solid line) for fan beam collimator with raytracing simulations. Simulation results for one particular position of the septa (red crosses) and an average over 100 different septa positions (black squares) are provided. Sensitivity given by the traditional diverging formula (black solid line) and a previously derived on-axis non-diverging formula of Accorsi and Metzler (2006) (green circles) are shown as well. (a) For x = 0 mm and y = 0 mm, (b) idem for sensitivity at x = 8 mm, y = 0 mm.

4.3.3   *Validation by raytracing*

In Figure 4-3 and Figure 4-4 we compared the sensitivity given by (4-11) with raytracing sim-ulations for the fan beam and cone beam example respectively. As explained in section 4.2.4, in our raytracing simulation we generated 100 different collimator configurations in which the location of the septa and holes was slightly different. Figure 4-3 shows the sensitivity averaged over these 100 configurations (black squares) and the sensitivity of one of these configurations (red crosses). The single configuration chosen is the one where a septum touches the collimator axis (one side of septum at $x = 0$, $y = 0$). As a reference we also plotted the conventional diverging expression provided in (4-10) and we showed the results of the earlier derived on-axis formula from Accorsi and Metzler (2006) for the on-axis plots.

Figure 4-3(a) and Figure 4-4(a) show the sensitivity profiles along the collimator axis (i.e. x = 0 and y = 0 mm), where the earlier expression derived by Accorsi *et al.* should also be valid. We indeed find very close agreement among S from (4-11), the ray-tracing simulation average over different septa locations and Accorsi's expression. We reported all differences between the analytical expressions and the simulations (averaged over the plotted profiles) as percentages of the maximum sensitivity obtained with that collimator in the simulation. For the fan beam collimator, the average and the maximum absolute difference between (4-11) and the averaged raytracing simulation are 0.5% and 4.3% respectively, as tabulated in Table 4-1. For the cone beam collimator, the average absolute difference between (4-11) and the averaged raytracer result is 0.7% of the maximum. The expression from Accorsi and Metzler (2006) was only derived on the collimator axis, where it agrees very well with (4-11). For both collimators the relative difference is everywhere less than 1/10 000th. The divergence of the traditional expression at the focal line is also clear from the image. In fact we see that in a region of 8 mm at either side of the focus,

Table 4-1 Mean/Max (over z = 0 to z = 80 mm) absolute differences for sensitivity expressions (S from (4-11), S_{div} from (4-10), and the previously derived non-diverging expression from Accorsi and Metzler (2006)) compared to raytracing simulation, and expressed as percentage of maximum sensitivity along each line in the simulation.

Mean/Max Difference (%)	S		S_{div}		Accorsi *et al.*	
Location(mm)	Fixed septa	Averaged over septa	Fixed septa	Averaged over septa	Fixed septa	Averaged over septa
Fan Beam						
$x = 0, y = 0$	1.4 / 4.3	0.5 / 4.3	∞ / ∞	∞ / ∞	1.4 / 4.3	0.5 / 4.3
$x = 8, y = 0$	0.6 / 4.4	0.1 / 0.5	0.7 / 3.5	0.3 / 4.1	N/A	N/A
Cone Beam						
$x = 0, y = 0$	0.9 / 6.0	0.7 / 5.6	∞ / ∞	∞ / ∞	0.9 / 6.0	0.7 / 5.6
$x = 8, y = 0$	0.4 / 5.5	0.3 / 5.4	∞ / ∞	∞ / ∞	N/A	N/A
$x = 0, y = 8$	0.3 / 3.4	0.2 / 3.7	∞ / ∞	∞ / ∞	N/A	N/A
$x = 8, y = 8$	0.1 / 1.1	0.1 / 0.4	0.4 / 3.4	0.4 / 3.4	N/A	N/A

the error of (4-10) is more than 5%. This corresponds with the condition found in section 4.3.2 for the divergent formula to be valid, i.e. $|F_x - z| \gg d_x(F_x + L)/L = 3.7$ mm.

In Figure 4-3(b) and Figure 4-4(b-d), we plotted sensitivity obtained from the same expressions but now along lines off the collimator axis ($x = 8$ mm and $y = 0$ mm, $x = 0$ mm and $y = 8$ mm, and $x = y = 8$ mm respectively). Note that for the fan beam collimator in total only two images are shown due to symmetry considerations. As the cone beam collimator is astigmatic, no symmetry is expected. Along the off-axis lines in Figure 4-3(b) and Figure 4-4(d) (note that in Figure 4-4(b) and Figure 4-4(c) there is still a diverging point), the traditional sensitivity formula does not diverge and is better able to describe the sensitivity than on-axis. Like in the on-axis case, we found close agreement between our sensitivity expression and the averaged raytracing results for all cases, see Table 4-1.
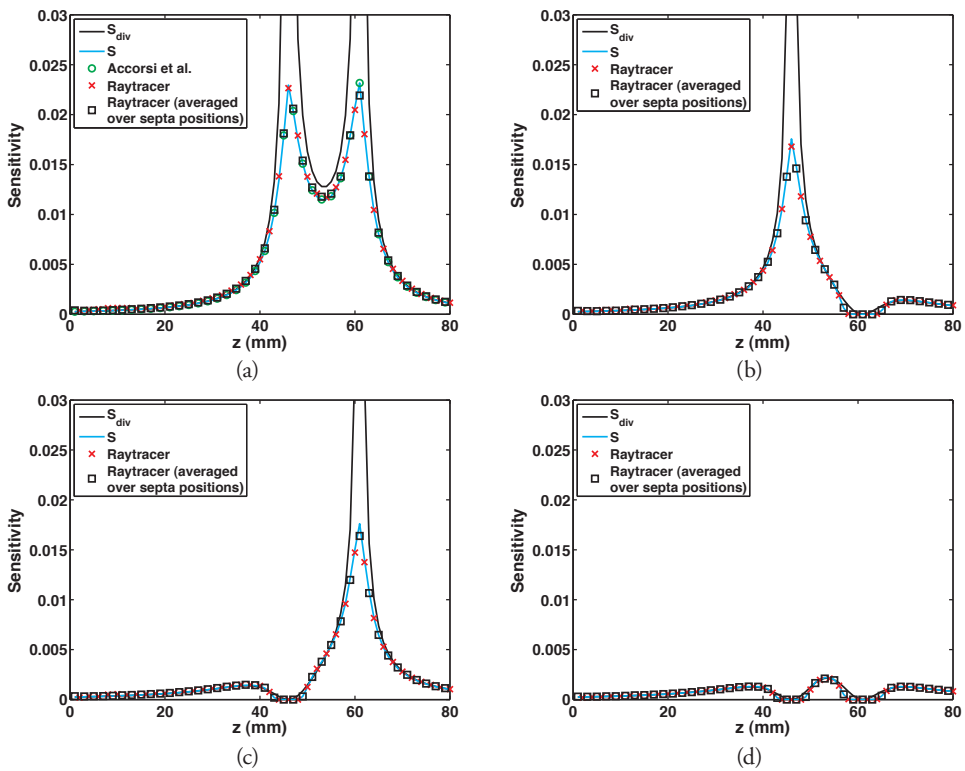
Figure 4-4 Comparison of analytically calculated sensitivity (cyan solid line) for astigmatic cone beam collimator with raytracing simulations. Simulations results for one particular position of the septa (red crosses), and an average over 100 different septa positions (black squares) are provided, as is the sensitivity given by the traditional diverging formula (black solid line). For on-axis results a previously derived on-axis non-diverging formula of Accorsi and Metzler (2006) (green circles) is shown. (a) For x =0 and y = 0, (b) idem for sensitivity at x = 8 mm, y = 0 mm, (c) idem for x = 0 mm, y = 8 mm (d) idem for x = 8 mm, y = 8 mm

Table 4-2 Mean/Max (over z = 0 to z = 80 mm) absolute difference between raytracing simulation with modelling of septa penetration and either (4-11) with the actual collimator length L or (4-11) with L replaced by the effective collimator length L_e expressed as percentage of maximum sensitivity along each line in the simulation.

Mean/Max Difference (%)	S with L		S with L_e	
Location(mm)	Fixed septa	Averaged over septa	Fixed septa	Averaged over septa
Fan Beam				
$x = 0, y = 0$	2.5 / 6.5	1.5 / 3.8	2.0 / 4.7	0.9 / 3.3
$x = 8, y = 0$	1.1 / 4.0	0.7 / 1.0	0.9 / 3.8	0.4 / 0.7
Cone Beam				
$x = 0, y = 0$	2.8 / 8.1	2.6 / 7.8	2.3 / 6.5	2.0 / 6.2
$x = 8, y = 0$	1.2 / 4.7	1.1 / 4.8	1.0 / 3.6	0.9 / 3.6
$x = 0, y = 8$	1.3 / 5.3	1.2 / 5.3	1.0 / 4.1	1.0 / 4.1
$x = 8, y = 8$	0.4 / 1.0	0.5 / 1.0	0.3 / 0.8	0.3 / 0.7

From Figure 4-3b it is clear that there are significant differences between the sensitivity of a single fixed collimator set-up and the average over 100 configurations. This is most pronounced close to the collimator, i.e. $z < 35$ mm in Figure 4-3b. This confirmed that the precise location of the septa can have a clear influence on the sensitivity especially close to the collimator as one might expect. We can see from table 1 that for the fan beam collimator the maximum difference increased from 0.5% for the average over 100 configurations to 4.4% for a single configuration for the off axis line. For the cone beam example (see Figure 4-4), the difference is less.

4.3.4 Septa penetration
As mentioned, in our derivation penetration of collimator septa was not considered as it was neither in the traditional derivation. Usually penetration is then included by replacing the collimator length L by an effective collimator length that depends on the attenuation coefficient of the collimator material at the gamma photon's energy (see section 4.2.4). For an initial analysis of the effect of penetration, we reran the raytracing simulation to include modelling of septa penetration. We calculated the difference between the raytracing simulation and the expression using either the physical length L, or the effective length L_e in (4-11). From the results in Table 4-2, we see that using an effective length reduces the differences between the averaged raytracing simulations and the analytical expression, but the differences are still larger than for the case without penetration (c.f. Table 4-1). For example the mean difference in the on-axis sensitivity of the fan beam collimator improves from 1.5% to 0.9% when L_e is used instead of L, while without penetration modelling in the raytracer the difference is 0.5%.

4.3.4.1 Volumetric Sensitivity
To analyse the conditions for which the old diverging formula is still a good approximation for calculating volumetric sensitivity, we looked at an example for volumetric sensitivity as described

Table 4-3 Volumetric (average) sensitivity for a brain SPECT cone beam example (see section 4.2.4.1). Comparing (4-11), with the traditional diverging formula (4-10)

Focal length (mm)	Sensitivity from (4-11) (%)	Sensitivity from (4-10) (%)	Difference (%)
150 mm	0.048	∞	∞
200 mm	0.057	∞	∞
250 mm	0.062	0.160	158
300 mm	0.063	0.100	60
350 mm	0.061	0.075	24
400 mm	0.057	0.062	9.8

in section 4.2.4.1. The sensitivity was calculated on a grid with voxel size of 1 mm, and then averaged over a spherical volume-of-interest (VOI) with diameter of 200 mm . The results are listed in Table 4-3. If the focal point is in the centre of the VOI (focal length 150 mm), the diverging expression does not produce a finite answer. On the other hand, when the focal point is outside the VOI, i.e. the focal length is larger than 250 mm, there is no singularity in the VOI and a finite answer is produced also with the traditional diverging expression. However, it is clear from Table 4-3 that although the traditional formula produces a finite answer, it can still be significantly off when the focus is outside the volume, e.g. for a focal length of 350 mm, which is 100 mm beyond the VOI, we still find an error of 24% in the average sensitivity in the VOI.

4.4   Discussion

We derived a non-diverging expression for the sensitivity of converging collimators which is valid over the whole field-of-view, contrary to earlier derived expressions. Our expression shows good agreement with raytracing simulation data. We showed that it agrees well (mean difference from 0.1% to 0.7 % and maximum difference from 0.4 to 5.6 %) with a raytracing simulation that was averaged over different configurations (different exact locations of the septa). Note that our sensitivity formula does not depend on the exact placement of the septa and from its derivation it is clear that it corresponds to a sensitivity averaged over different septa locations. As shown in Figure 4-3, Figure 4-4, and Table 4-1, the sensitivity can be significantly influenced by the exact location of the septa and holes when the source is placed close to the collimator; for a source right above a hole more photons are detected than when the source is just above a septum. This is true not only for cone and fan beam, but also for the parallel hole collimators. One could in principle derive a formula in which the exact location of the septa is contained but this would become very complicated. Therefore, all analytical sensitivity expressions represent an average over slightly different geometries. One should however be aware that in the case an exact collimator response is required (e.g. in iterative image reconstruction) the exact septa/ hole location may need to be considered (Formiconi, 1998).

In our derivation, penetration of collimator septa is neglected. Including septal penetration into the collimator's response function would make the derivation tremendously more complex and we are not aware of any sensitivity calculation into which this is fully taken into account, even not for the simpler case of parallel hole collimators . The common way to include penetration is to replace the actual physical collimator length by an effective hole length as we have also done.

In the derivation the only approximations made are the averaging step over the septa positions, and the mentioned neglected septal penetration. No other approximations were used as we evaluated the integral fully. The fact that on the collimator axis the numerical agreement is within 1/10000th of the separately derived and differently formulated expression from Accorsi and Metzler (2006), and the fact that in special cases it reduces to other previously known formulas makes us confident that we didn't make any mistakes in our calculation. Therefore, we believe the remaining differences between our expression and the raytracing simulations can be explained by discretization errors in the simulation. Firstly, the collimator volume in our raytracer is represented with finite voxels. Especially for thin septa, the continuous septa are challenging to accurately represent with cubic voxels. In our simulations we assume a voxel size of 0.05 mm while septa had a thickness of 0.2 and 0.3 mm. Smaller voxels would lead to prohibitively large collimator volumes, as the collimator volumes used in this paper took already 19 GiB to store. Secondly, the detector is modelled with finite pixels, which can be partially covered by septa while the raytracer only traces to the centre of a pixel. Lastly the averaging over the different septa locations was done using 100 configurations. Although, one expects the effect on sensitivity to be relatively smooth as function of the septa locations, and 10 samples in each direction should suffice, a small error is introduced here as well.

The traditional sensitivity formula for parallel hole collimators, on which the first fan and cone beam expressions are based, contain a factor describing effects of different hole shapes and patterns. This factor is usually denoted with k or K (Anger, 1967; Cherry *et al.*, 2003). The traditional diverging expressions for converging collimators include the same factor. In their paper about the non-diverging axial formula for converging collimators, Accorsi and Metzler (2006) provide a more extensive description of the effect of hole shape and they derived additional correction factors that can be used to convert sensitivity formulas of square holes to other hole shapes, such as round or hexagonal holes. Such factors can also be included in our expressions although it is besides the scope of this paper to test their accuracy.

In literature, different definitions of the parameters for converging hole collimators can be found. We decided to keep the hole area constant at the object side of the collimator as is commonly done (Tsui and Gullberg, 1990; Accorsi and Metzler, 2006), while others like Formiconi (1998) kept the bore width (the distance between septa measured perpendicular to each hole's axis) constant at the object side of the collimator, thereby making the areas of the holes at the collimator surface larger towards the collimator edges, as in the edges in the x and y directions.

Note that precise manufacturing of converging collimators is a difficult process which has caused constraints in collimator design, as for example thin septa are very hard to produce. In recent years new technologies like 3D printing have emerged that allow more challenging designs to be manufactured (Van Audenhaege *et al.*, 2015; Pato *et al.*, 2015) that may better exploit the advantages of strongly focusing collimators. Therefore, a new look at the possibilities of converging collimators might be worthwhile and correct sensitivity expressions for such collimators are then desirable.

4.5 Conclusions

We derived a new expression for the sensitivity of converging collimators. Contrary to known sensitivity formulas, our formula is valid over the full field-of-view and does not diverge near the focus. It can thus be applied to accurately determine sensitivity near the focus of converging collimators.

4.6 Acknowledgement

Appendix 4.A Figure
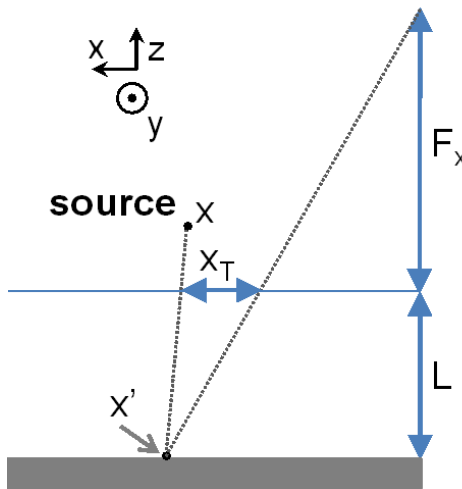
Figure 4-A1 Schematic overview of the definition of $\mathbf{r}_T = (x_T, y_T)$. Illustrated are dashed lines from the source to the current integration point x', from the focus to the current integration point x', the distance between these two lines on the collimator surface x_T. While this illustration is in two dimensions, y_T can be illustrated likewise.

Chapter 5

System geometry optimization for Molecular Breast Tomosynthesis with focusing multi-pinhole collimators

Abstract

Imaging of 99mTc labelled tracers is gaining popularity for detecting breast tumours. Recently, we proposed a novel design for molecular breast tomosynthesis (MBT) based on two sliding focusing multi-pinhole collimators that scan a modestly compressed breast. Simulation studies indicate that MBT has the potential to improve the tumour-to-background contrast-to-noise ratio significantly over state-of-the-art planar molecular breast imaging. The aim of the present paper is to optimize the collimator-detector geometry of MBT. Using analytical models, we first optimized sensitivity at different fixed system resolutions (ranging from 5 to 12 mm) by tuning the pinhole diameters and the distance between breast and detector for a whole series of automatically generated multi-pinhole designs. We evaluated both MBT with a conventional continuous crystal detector with 3.2 mm intrinsic resolution and with a pixelated detector with 1.6 mm pixels. Subsequently, full system simulations of a breast phantom containing several lesions were performed for the optimized geometry at each system resolution for both types of detector. From these simulations we found that tumour-to-background contrast-to-noise ratio was highest for systems in the 7 mm to 10 mm system resolution range over which it hardly varied. No significant differences between the two detector types were found.

5.1   Introduction

The most common type of cancer affecting women is breast cancer; it constitutes 25 percent of all new female cancer cases worldwide and causes 15 % of all cancer related deaths in women (Ferlay et al., 2015; Torre et al., 2015). Breast cancer detection is being improved by advances in imaging technology. While X-ray mammography is still the most widely used modality, other breast imaging modalities that are being used include ultrasound, molecular breast imaging (MBI) with planar gamma cameras, magnetic resonance imaging, positron emission tomography, and digital breast tomosynthesis based on x-rays. An overview can be found in Hruska and O'Connor (2013) and Fowler (2014).

In **Chapter 2,** our group proposed a design for a novel Molecular Breast Tomosynthesis (MBT) scanner dedicated to imaging distributions of single-gamma emitting tracers in the breast (Beekman, 2014; van Roosmalen et al., 2016). In the design, the patient lies prone on a bed with an opening for the breast, which is mildly compressed. Two scanning gamma cameras equipped with focusing multi-pinhole collimators acquire projections of the breast in a sequence of camera positions. The focusing collimator geometry combined with the possibility to confine the scan area enables to increase the signal from a suspected region of interest. The simulation study (van Roosmalen et al., 2016) indicated that multi-pinhole MBT offers 3D localization of increased tracer uptake and may have the potential to increase tumour-to-background contrast-to-noise ratio (CNR) compared to planar MBI. As the pinhole geometry has a range of viewing angles of less than 180 degrees resulting in incomplete sampling, the term molecular tomosynthesis is

used instead of SPECT. We introduced MBT in the earlier paper, but the system has not been optimized yet.

The first MBT design was based on conventional gamma detectors with a continuous NaI(Tl) scintillator read out by an array of photo-multiplier tubes (PMTs). Due to their cost effectiveness, these are still the most widely used detector types in SPECT and planar scintigraphy. However, there are more options (Peterson and Furenlid, 2011) as several new scintillation detectors are being investigated, e.g. those based on pixelated crystals, new light sensors and better detection algorithms. Moreover, semi-conductor detectors like CZT, which can provide both high spatial and energy resolution, have become commercially available. As high-resolution detectors are typically much more expensive than conventional NaI(Tl) detectors, it is important to make a detector choice based on a thorough understanding of its ultimate impact on images.

As imaging characteristics depend on many properties such as sensitivity, system resolution, size of the field-of-view (FOV) and angular sampling over the FOV, it is not straightforward to de-sign optimized multi-pinhole geometries. One of the complications is the way each of these properties depends on the many tuneable parameters. To fully consider their interdependence, optimization should be done on a complete system comprised of collimators and detectors, which can be done by performing time-consuming full system simulations. However, this is not feasible for simulating a whole range of designs covering the entire parameter space. Therefore, we here take the approach of initially using analytical models to optimize sensitivity of MBT at a fixed system resolution. This optimization is repeated for a range of system resolutions (from 5 to 12 mm). After this analytical optimization, we evaluate optimized configurations with different system resolutions by complete system simulations of breast phantom images.

5.2 Methods

In this section, we describe the basic design of MBT, the geometry optimization process and how we evaluate simulated images.

5.2.1 Molecular Breast Tomosynthesis

In the in **Chapter-2** proposed MBT scanner (Beekman, 2014; van Roosmalen et al., 2016), the patient lies prone on a specially designed bed, with the scanner underneath as detailed in Figure 5-1. In our initial design, two Tungsten plates containing 63 pinholes each serve as collimators. They project the tracer distribution in the breast on conventional gamma detectors equipped with continuous 250 x 150 x 9.5 NaI(Tl) crystals (3.2 mm intrinsic resolution) placed 40 mm from the breast (parameter L in Figure 5-2(a)). The pinholes in each of these collimator plates focus to a line at 40 mm distance from the collimator face (F_x=40 mm in Figure 5-2(a)) and thus view a part of the breast. Such a focused design gives the MBT scanner the unique ability to focus on a user-defined volume-of-interest (VOI), which is beneficial because it can in-crease the count yield from the VOI (Beekman et al., 2005; van der Have et al., 2009). The VOI can be selected by the user on a graphical interface, which uses images taken by optical cameras
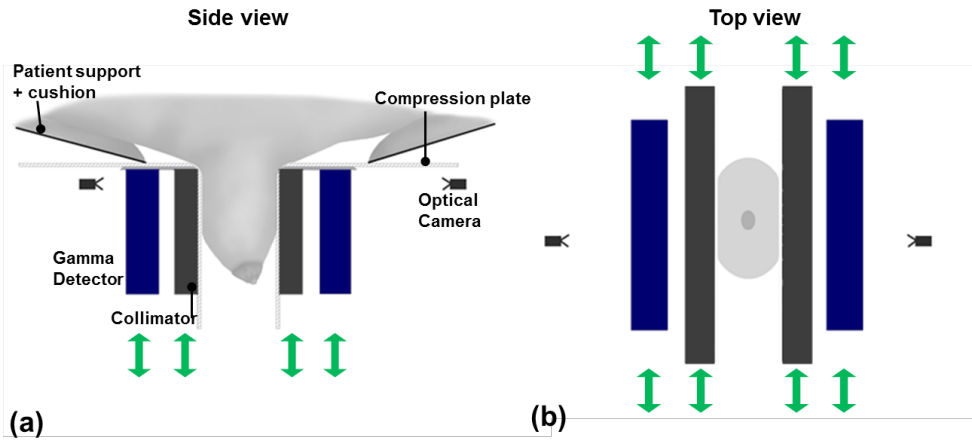
Figure 5-1 Schematic illustration of the geometry of the MBT scanner including compression plates, collimators, and gamma detectors. The green arrows indicate the directions into which the collimators and detectors can move. a) Side view showing breast of a woman lying prone on the scanner table. The breast is placed in the opening in the bed and slightly compressed. b) Top view of the breast between the transparent compression plates (artist impression).

that view the breast through the compression plates (Branderhorst et al., 2011; Beekman, 2012). To image any volume, the FOV should be translated over the breast such that the desired scan volume is viewed over a range of angles (Vastenhouw and Beekman, 2007; Vaissier et al., 2012). In MBT this is done by synchronized step-and-shoot movement of the collimators and detectors. For image reconstruction, all available information is taken into account, as the projection data from all positions is used simultaneously (Vastenhouw and Beekman, 2007)

5.2.2   *System design*
In this paper, we investigate the optimal collimator-detector set-up for MBT. In all designs, we assume that a lightly compressed breast is imaged with two focusing multi-pinhole collimators that each project onto a gamma detector. The collimator-detector geometry and the type of gamma detector are varied as explained below, and illustrated in Figure 5-2(a&b)

5.2.2.1   *Considerations for collimator design.*
All parameters that together uniquely define a multi-pinhole collimator are listed in table 1. In principle, an infinite number of pinhole collimators can be considered when optimizing the designs, but we restrict ourselves by the following design principles.

a)   To account for the 4 mm thick compression plates and 2 mm between collimator surface and pinhole centre, a total distance is assumed between pinhole centre and breast of 6 mm.

b)   b) To prevent multiplexing related artefacts (Vunckx et al., 2008; Mok et al., 2009) we eliminate overlapping of projections by using a shielding plate in between collimator and detector (Beekman et al., 2005; van Roosmalen et al., 2016), see Figure 5-2(a&b). Figure 5-3 shows how the opening angle γ and axis direction of the prismatoidic holes in the plate
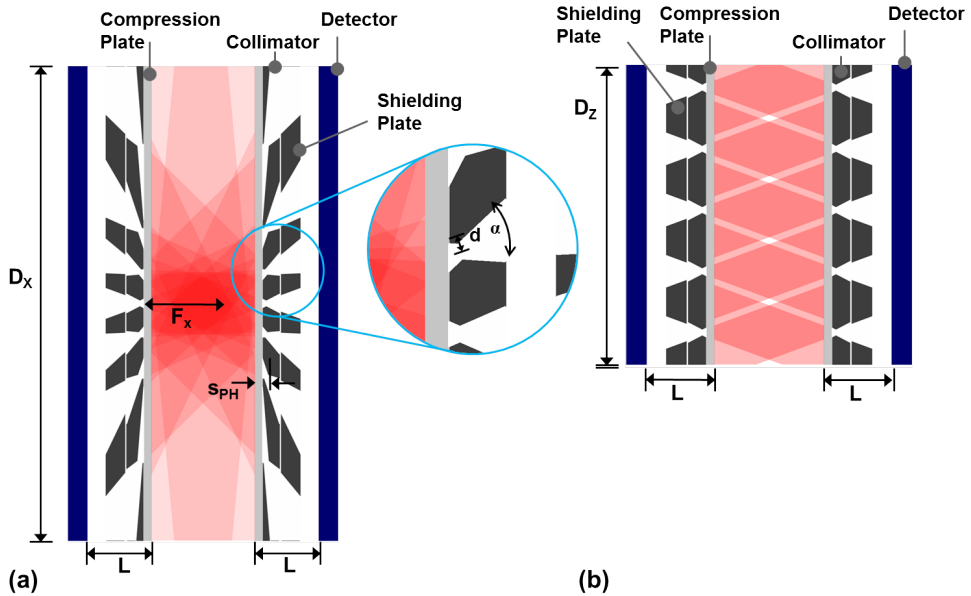
Figure 5-2 General design for MBT. The dark blue box represents the gamma detector, red shows the field-of-view, light grey the transparent compression plates, and dark grey the collimator and shielding plate. The different parameters are indicated in the figure. Two views are shown: (a) a coronal plane cross section and (b) a sagittal plane cross section

      are linked to each of the pinholes. Each pinhole illuminates the entire rectangular hole in the shielding tube. The flood source projection in Figure 5-4 shows that this results in tiled projections.

c)   We control the amount of focusing by fixing the distance from the collimator face to the line all pinhole axes point to (see Figure 5-2 & Figure 5-4) by setting the focal length Fx=40 mm (see Figure 5-2(a)). This way all tested designs have a similarly sized FOV. We found that much stronger amounts of focusing were prohibited because in that case the outer pinholes were angulated so much that they started to overlap. On the other hand, if the focal length is too large, the benefits of focusing (described in section 5.2.1) are lost.

d)   The sizes of the pinhole projections on the detector depend on the choice of pinhole opening angle α (as pinhole opening angle and dimensions of holes in the shielding tube are directly linked, see point 2). Generally, increasing α will allow for less non-overlapping pinholes to be used but will also lead to a larger volume sensitivity per pinhole. Initial simulations showed that these effects cancel out meaning that the choice of opening angle does not have a large influence on the resolution-sensitivity trade-off. Thus, we decided to fix α for all pinholes in a configuration, such that the central upper pinhole's projection (de-fined below) on the detector always has the same dimensions (25x25 mm).

Considering the design considerations described above, the pinhole diameter and the distance L between breast and detector are left as parameters to optimize the resolution-sensitivity trade-off.

Table 5-1 List of parameters determining a pinhole collimator

Parameter	Description	Value	Varied/Fixed
L	Detector-breast distance		Free
D_x, D_y	Lateral dimensions of the detector	250, 150 mm	Fixed
R_i	Intrinsic spatial resolution of detector	1.6, 3.2 mm	We consider 2 detectors
R_t	Targeted system resolution	5, 6, 7, 8, 9, 10, 11, 12 mm	We optimize sensitivity at several values
d	Pinhole diameter		Calculated to reach the target system resolution
α	Pinhole opening angle		Calculated to keep number of pinholes constant
S_{PH}	Distance between breast and pinhole centre	6 mm	Fixed at minimal feasible value
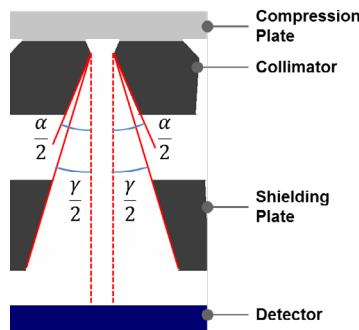
Figure 5-3 Schematic representation of cross section through a pinhole and the shielding plate. Indicated are the pinhole opening angle α and the opening angle for the hole in the shielding plate γ. Axis of pinhole and shielding plate hole are aligned.

An important design aspect for a multi-pinhole collimator is the placement of the pinholes. The requirement to fill the detector with non-overlapping projections means that all pinholes must be repositioned when e.g. L is varied. As we need to evaluate many configurations, we created an algorithm for automatic pinhole placement. The procedure used, as illustrated in Figure 5-4, reads:

a. Place a pinhole at the top centre of the collimator (i.e. closest to the breast and in the middle horizontally) such that its projection touches the edge of the detector (Figure 5-4(a))
b. Place the next pinhole to one side horizontally (using a line search) in such a position that the projection from the pinhole is separated by exactly 3 mm from the first pinhole's projection (Figure 5-4(b)).
c. Repeat step b) on both sides until the side of the detector is reached. Then, start from the next row below (Figure 5-4(c)).
d. Repeat step b) and c) until the whole detector is filled (Figure 5-4(d)).

Flood source projection   Coronal cross section   Sagittal cross section

(a)

(b)

(c)

(d)
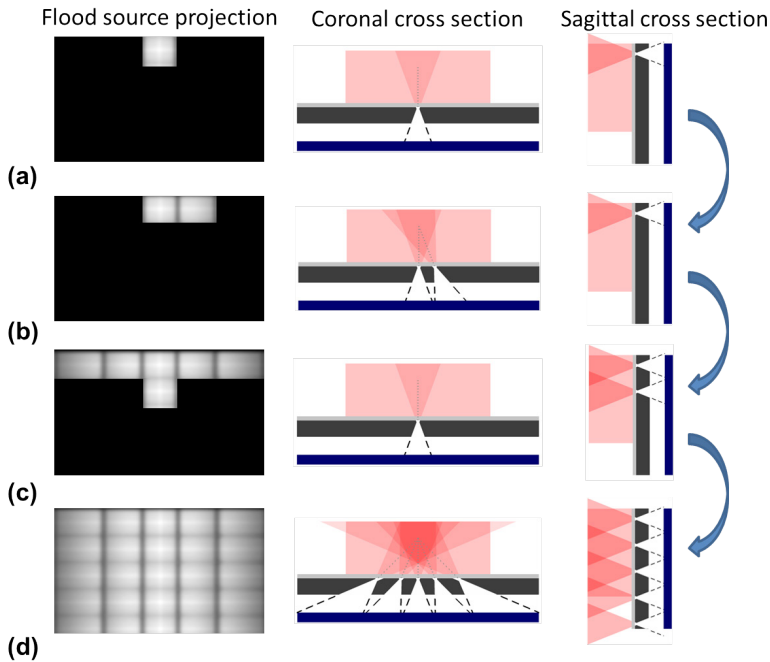
Figure 5-4 Schematic overview of the automatic pinhole placement. Flood source projection on the detector is shown as well as coronal and sagittal cross-section through collimator and detector. (a) The first pinhole is placed. (b) A subsequent pinhole is placed next to the first pinhole such that projection is adjacent and non-overlapping (c) After filling one row, a pinhole is placed in the centre of the next row. (d) This process continuous until the whole detector is filled with pinhole projections.

5.2.2.2   Considerations for detector choice

Detectors with continuous NaI(Tl) crystals read out by PMTs, as used in the initial MBT design, have the advantage of being cost effective and having a high detection efficiency (~90% for 140 keV photons). We assumed an intrinsic resolution of these detectors of 3.2 mm. In this paper, we will additionally evaluate the usefulness of high resolution pixelated detectors with 1.6 mm pixel size and a detection efficiency of ~70% for 140 keV photons. This corresponds to for example CZT detectors as applied in planar MBI (Hruska et al., 2012) or pixelated NaI(Tl) crystals with PMT's. In the latter case the reflective material between the pixels reduces the efficiency (Rozler et al., 2012). The two detectors types will henceforth be referred to as continuous and pixelated detector.

For breast imaging, it is important and challenging to also image breast tissue close to the chest wall. As in our earlier paper, we assume a dead edge of 5 mm for all detectors, which is achievable even with NaI(Tl) detectors read out by PMTs by using Maximum Likelihood processing (Milster et al., 1990; Moore et al., 2007; Barrett et al., 2009). For all reported results, the appropriate detector efficiency for each detector type is taken into account, i.e. both in the analytical resolution-sensitivity calculations as in the full system simulations.

5.2.3   Analysis of different collimators and detectors based on sensitivity-resolution trade-off and simulation

In the analytical optimization study, the sensitivity is maximized at a fixed system resolution, as generally, when other characteristics are kept equal, more detected counts lead to an improved signal-to-noise ratio. We do this for a range of different target system resolutions from 5 to 12 mm. For each system resolution, the design with the highest sensitivity is selected for full system simulations.

We report sensitivity averaged over the breast shaped region described in section 5.2.5.1. In our design in which the detector and collimator are translated over a sequence of positions, sensitivity depends on the sequence chosen, which is provided in section 5.2.4. A sensitivity-weighted averaged resolution is determined over the same region, and the pinhole diameter is iteratively adjusted until the desired target system resolution is reached.

5.2.3.1   Resolution & Sensitivity formulas.

We quickly estimate resolution and sensitivity by using the following formula (Metzler et al., 2001) for the sensitivity g of a single knife-edge pinhole

$$g = \frac{d^2 \sin^3 \theta}{16h^2} + \frac{\sin^5 \theta \tan^2 \frac{\alpha}{2}}{8h^2\mu^2} \left(1 - \frac{\cot^2 \theta}{\tan^2 \frac{\alpha}{2}}\right)\left(1 - \frac{\cot^2 \theta}{\tan^2 \frac{\alpha}{2}} + \mu d \csc \theta \cot \frac{\alpha}{2}\right) \qquad (5\text{-}1)$$

Here θ is the angle between the plane perpendicular to the pinhole axis and the line from the pinhole centre to the source, μ the linear attenuation coefficient of the collimator (3.38 mm^{-1} for 140 keV photons in Tungsten) and h the perpendicular height of the source above the pinhole, other parameters were defined in Table 5-1.

For system resolution, defined as the full with at half maximum (FWHM) of the point spread function, we use

$$R_p = \sqrt{d_e^2\left(1 + \frac{1}{M}\right)^2 + \left(\frac{R_i}{M}\right)^2} \qquad (5\text{-}2)$$

where M is the magnification factor of the pinhole (i.e. the ratio between distance from source to pinhole, and pinhole to detector), de the effective pinhole diameter, and R_i the intrinsic detector resolution. Accorsi and Metzler (2004) derived effective diameters d_{e1} and d_{e2} for the directions parallel and perpendicular to line of incidence on the detector, which are given by

$$d_{e1} \approx d + \frac{\ln 2}{\mu}\left(\tan^2 \frac{\alpha}{2} - \cot^2 \theta\right)\cot \frac{\alpha}{2} \sin \theta,$$

$$d_{e2} \approx \sqrt{\left(d + \frac{\ln 2}{\mu}\tan \frac{\alpha}{2}\sin \theta\right)^2 - \left(\frac{ln2}{\mu}\right)^2 \cos^2 \theta.} \qquad (5\text{-}3)$$

To arrive at one value for resolution we use the average of the two resolutions obtained by substituting the effective diameters in (5-2), as the effective resolution.

As mentioned above, we fix the size of the projection of the centre pinhole in the first row on the detector, by adjusting the opening angle to

$$\alpha = 2 \arctan\left(\frac{25mm \, / \, 2}{L - 6mm}\right). \tag{5-4}$$

For the continuous detector a value of 3.2 mm is used for R_i, while a value of 1.6 mm is used for the pixelated detector. Note that in our analytical formulas we do not distinguish between continuous or pixelated crystals. As explained below, our full system simulations do take into account detector pixilation for the higher resolution detector.

5.2.4 *Sampling* & *scan positions.*

As mentioned above, the selected volume is imaged by moving the collimators in a sequence of steps. Movement takes place in the plane defined by the compression plates, i.e. either left-right (Figure 5-1(b), or up/down (Figure 5-1(a)). In this paper, we use a sequence that covers the whole breast.

Ideally, one optimizes the scan sequence for a specific collimator. However, as we compare many designs and need to be sure we compare them equally, we use a single sequence with many closely spaced positions. This way we always get a uniform sensitivity regardless of the designs specific FOV pattern. For a single specific collimator one can design a scan sequence with a realistic number of positions, as we did in van Roosmalen et al. (2016).

The sequence we use consists of the collimators and detectors moving in the anterior direction in 2 mm steps for a total distance of 20 mm and from left to right in 8 mm steps from position -76 mm to 76 mm, where 0 mm denotes a collimator centred on the breast.

5.2.5 *Validation by simulations of breast phantom scans*

To validate the results from our analytical analysis and further analyse the most promising de-signs, we performed simulations for a few selected configurations. In these simulations, we accurately simulated gamma photon transport through our collimator, using a ray-tracing simulator (Wang et al., 2017) (**Chapter 3**), which was used to both generate simulated projections and a system matrix for image reconstruction. This simulator uses the collimator modelled as a voxelized volume with a voxel size of 0.0625 mm as its input. The depth-of-interaction in the scintillator crystal is modelled by also raytracing the gamma photon through the scintillator, similarly as was de-scribed in (Goorden et al., 2016). Consequently, the detector efficiency is automatically taken into account. For the continuous detector, we assumed 1.072 mm pixels in a 234x140 pixel grid and the intrinsic detector resolution was incorporated by modelling detector response with a 3.2 mm FWHM Gaussian. For the simulated pixelated detector systems, the detector was modelled using 1.6 mm pixels in a 156x94 pixel grid and no additional filter was applied.

To calculate phantom projections, we represented the phantoms on a regular grid with a source voxel size of 0.5 mm. The raytracer uses a threshold for ignoring small contributions which we set to 1% (Wang et al., 2017). Moreover, the attenuation in the phantom was modelled using a uniform attenuation coefficient of 0.0151 mm^{-1} valid for 140 keV photons in water. We then generated phantom projections for each of the positions in the scan sequence accounting for the scanning time in each position and added Poisson distributed noise to each projection. Earlier phantom studies for a similar geometry showed that scatter from the torso is not a significant problem for ^{99m}Tc-based tracers (Wang et al., 1996; Hruska and O'Connor, 2006), which was confirmed in a simulation study for our MBT geometry (Wang et al., 2017). Therefore, the use of a raytracer that models attenuation but ignores scatter is justified for this geometry.

For the tomographic reconstruction of the projection data, we used Maximum Likelihood Expectation Maximization (MLEM). The system matrix used in MLEM was determined at a 1.0 mm source voxel grid and a threshold of 2%. The discrepancy in grid size between phantom and reconstruction, and between cut off thresholds is to mimic a continuous activity distribution. Moreover, at this stage we decided not to apply an attenuation correction, as no method for accurately determining of the entire contour of the breast is yet established.

For the systems selected for full system simulations, the automatically generated designs were slightly tuned if needed to prevent pinholes at the edge to only have a small fraction of their projection on the detector, by adjusting the opening angle of all pinholes up to 5%. We checked that these small tunings resulted in changes in the analytically calculated resolution and sensitivities that were within 2.5 % of the unadjusted values.

5.2.5.1 *Breast phantom*

In this paper, we use the same phantom as in our earlier work (van Roosmalen et al., 2016). The breast is modelled as half an elliptically shaped disk (Dong et al., 2011), with a 110 mm chest-to-nipple distance, a width of 150 mm, and a thickness of 55 mm. The phantom is placed such that the top of the activity is at the same place as the start of the useful field of view of the detector. To assess how differently sized lesions are imaged, we placed four sets with three lesions each in the phantom (6.0, 5.0, 4.5, 4.0 mm diameter), see Figure 5-5(a). Within each set the central lesion was placed at a depth of 22 mm, with the other two lesions at a depth of 33 mm,
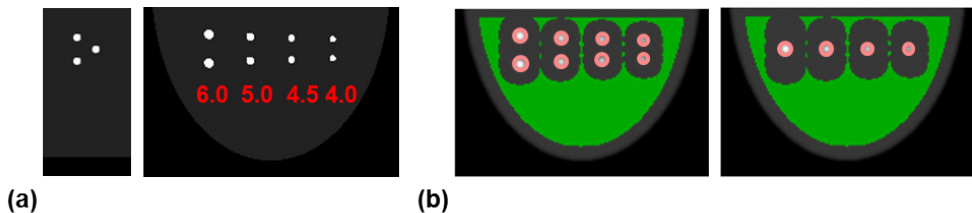

(a) **(b)**

Figure 5-5 Slices through the breast phantom (a) left: slice parallel to sagittal plane through the 6.0 mm lesions, right: transverse slice at depth of two lesions. Lesion sizes indicated. (b). Transverse slices with red circles indicate the regions-of-interest used to determine the tumour signal while the green area denotes the background region.

making a triangular arrangement. We assumed a background activity concentration of 3.7 kBq/mL, consistent with an injection of 925 MBq 99mTc-Sestamibi (Hruska et al., 2012; Mann et al., 2012). We assume a concentration of 37 kBq/ml in the lesions to give a tumour-background uptake ratio of 10:1 (Maublant et al., 1996; Lee et al., 2004; Hruska and O'Connor, 2008; Sullivan et al., 2012). We set scan time of 10 minutes.

5.2.5.2 *Analysis of images*

Besides visually inspecting different images, we compared different breast phantom images by calculating the tumour-to-background contrast-to-noise ratio (CNR) of the lesions given by

$$CNR = \frac{\bar{S} - \bar{B}}{\sigma_B} \qquad (5\text{-}5)$$

Here S is the average signal taken in a spherical region placed on top of the lesion, $\bar{B}$ is the average signal in a background region, and is σ_B the standard deviation in the background region and serves as measure of the noise. The regions used are indicated in Figure 5-5(b). All simulations are repeated for 20 different noise realizations, and the average of the CNR values is reported.

5.3   Results

5.3.1   *Analytical optimization*

Results of the analytical optimization are shown in Figure 5-6 in which sensitivity is shown as function of detector-breast distance for different fixed system resolutions (achieved by tuning the pinhole diameter). Note that every point in this graph represents the sensitivity of a different multi-pinhole geometry that was automatically generated by our script. Sensitivities for fixed system resolutions of 5 to 12 mm are shown for each detector. From the plots one can infer that, depending on the chosen system resolution, there is an optimal detector-breast distance at which sensitivity is maximal. The exact position of the optimum is determined by the relative
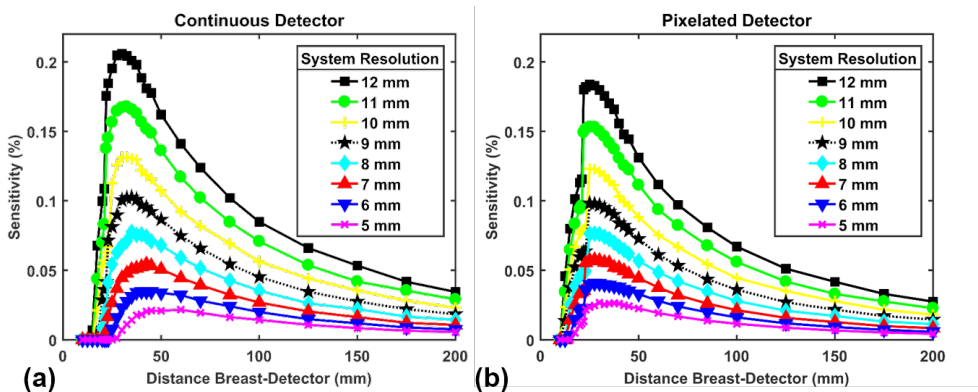

(a)   **(b)**

Figure 5-6 Volumetric sensitivity (averaged over the breast) as function of distance between detector and breast for (a) continuous detector, (b) pixelated detector. The lines indicate different fixed system resolutions R_t (5, 6, 7, 8, 9, 10, 11 and 12 mm).

contribution of two opposing effects. On one hand, placing the detector further away allows for larger pinhole magnification factors meaning that larger pinhole diameters can achieve the same fixed system resolution, thus increasing the sensitivity. On the other hand, placing the detectors closer to the breast increases the solid angle at which detection can take place which also enhances sensitivity. The sensitivity drops rapidly at short detector-breast distances, as for these short distances the projections from the activity distribution on the detectors are not magnified anymore but minified and as a result the pinhole diameter is quickly shrinking to maintain resolution.

As expected, the curves in Figure 5-6 indicate that the maximum sensitivity that can be obtained decreases as targeted system resolution improves. This dependence is shown in Figure 5-7 in which maximum sensitivity for different fixed system resolutions is shown for the two different detectors. The characteristics of the systems that obtain the maximum sensitivity at each system resolution are reported in Table 5-2 and Table 5-3. Although the higher resolution pixelated detector leads to collimators with higher sensitivities this is offset by its lower detection efficiency. Overall a small improvement in sensitivity is reached with pixelated detectors if the targeted system resolution is 5 or 6 mm, while the continuous detector provides slightly higher sensitivity for the 9 to 12 mm target system resolutions.

5.3.2   *Simulation results*

Full system simulations were performed for each of the optimal configurations (maximum in Figure 5-6, and geometries summarized in Table 5-2 and Table 5-3). We checked that sensitivities extracted from system matrices that were generated in these simulations were close to those predicted by the analytical expressions (<4% difference) which partly validates our analytical analysis.

The appearance of breast phantom images resulting from these simulations depends on the number of iterations used and the FWHM of the Gaussian filter applied. The optimal combination of
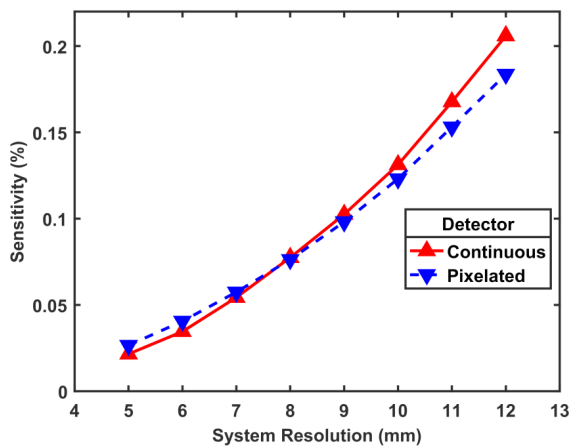

Figure 5-7 Plot of maximum reachable sensitivity as function of system resolution for both detector types. For each resolution, the breast detector distance that gives the highest sensitivity at that fixed resolution is used (maximum in Figure 5-6).

Table 5-2 Details of simulated systems with 3.2 mm intrinsic resolution continuous detector. Parameters of geometries that maximize sensitivity (and are thus simulated) are provided for each system resolution. The iteration number and filter size to reach the maximal CNR for the 6.0 mm lesion in reconstructed images are provided.

System Resolution (mm)	5.0	6.0	7.0	8.0	9.0	10.0	11.0	12.0
Detector-breast distance (mm)	47.5	40	40	35	35	32.5	32.5	30
Pinhole diameter (mm)	1.98	2.21	2.75	3.01	3.49	3.72	4.13	4.27
Pinhole opening angle (degree)	29	35	35	39	39	42	42	45
Volumetric Sensitivity over whole breast (%)	0.022	0.035	0.054	0.077	0.102	0.131	0.168	0.206
Sensitivity in focus (%)	0.087	0.129	0.191	0.259	0.346	0.424	0.520	0.601
Optimal Iteration	11	14	16	17	17	19	20	21
Optimal filter FWHM (mm)	5	4	4	3	2	1	1	0
Optimal CNR	8.5	9.8	10.5	10.6	10.3	10.6	9.9	9.1

Table 5-3 Details of simulated systems with 1.6 mm pixelated detector. Parameters of geometries that maximize sensitivity (and are thus simulated) are provided for each system resolution. The iteration number and filter size to reach the maximal CNR for the 6.0 mm lesion in reconstructed images are provided.

System Resolution (mm)	5.0	6.0	7.0	8.0	9.0	10.0	11.0	12.0
Detector-breast distance (mm)	30	27.5	27.5	27.5	25	25	25	25
Pinhole diameter (mm)	1.67	1.92	2.32	2.71	2.84	3.21	3.56	3.91
Pinhole opening angle (degree)	45	49	49	49	53	53	53	53
Volumetric Sensitivity over whole breast (%)	0.027	0.041	0.057	0.076	0.098	0.123	0.153	0.184
Sensitivity in focus (%)	0.083	0.119	0.171	0.227	0.273	0.341	0.184	0.487
Optimal Iteration	12	14	15	16	17	17	19	19
Optimal filter FWHM (mm)	4	4	4	3	3	2	2	2
Optimal CNR	9.2	9.4	10.4	10.4	10.5	10.0	9.8	9.2

these parameters can strongly depend on system resolution and sensitivity. For a fair comparison, we determined an optimal combination of iteration number and filter level in the following way: Gaussian filters with FWHM ranging from 0 to 8 mm (in 1 mm steps) were applied to all images and the iteration number and filter combination that lead to the highest CNR in the 6.0 mm lesions (on average over the noise realizations) was determined, requiring at least 5 iterations to ensure a minimum level of convergence. This optimal number of iterations and filter and the achieved optimal CNR for 6.0 mm lesions are also provided in Table 5-2 and Table 5-3.

Figure 5-8 shows images at three filter levels with the most optimal filter level marked with a red boundary. Each image is shown with the optimal number of iterations for that filter level. From these images, it is difficult to distil any clear differences in performance for the different systems. In the higher resolution systems, the spheres are slightly less elongated between the two
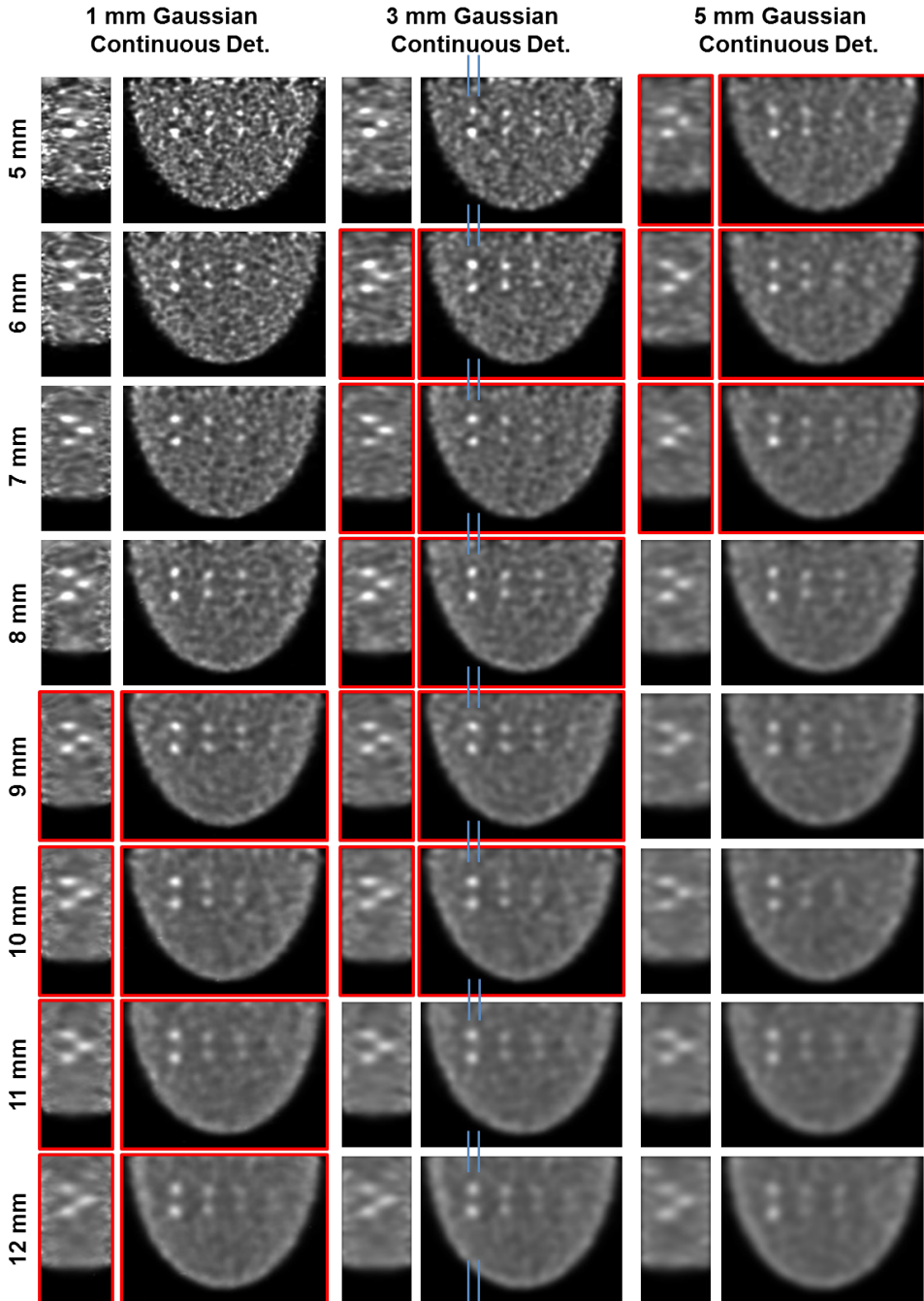
Figure 5-8 Simulated images of a breast shaped phantom containing lesions of 4.0, 4.5, 5.0 and 6.0 mm. Alternating images show slices parallel to sagittal plane through the lesions, transverse slice at depth of two lesions. Each row represents a different target system resolutions, while different columns show different filter levels (1.0, 3.0 and 5.0 mm FWHM Gaussian filter) and different detector types (Continuous or

**1 mm Gaussian
Pixelated Det.**   **3 mm Gaussian
Pixelated Det.**   **5 mm Gaussian
Pixelated Det.**
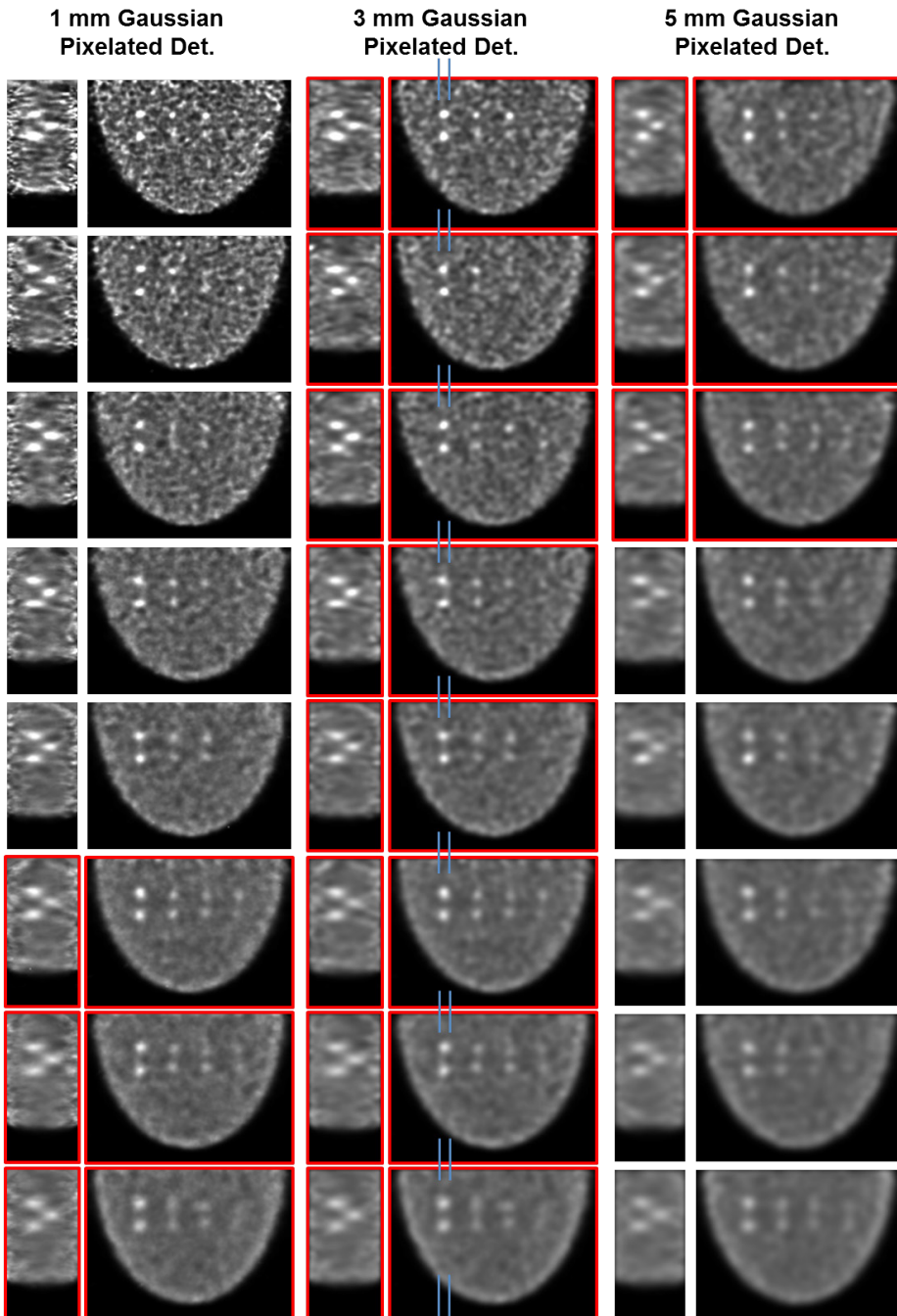
Pixelated). The number of iterations for each image is as listed in tables 2 and 3. The red boxes in each row indicate the filter levels that result in the highest CNR for the 6.0 mm lesions for that system. Blue lines indicate location of profiles shown in Figure 5-10.
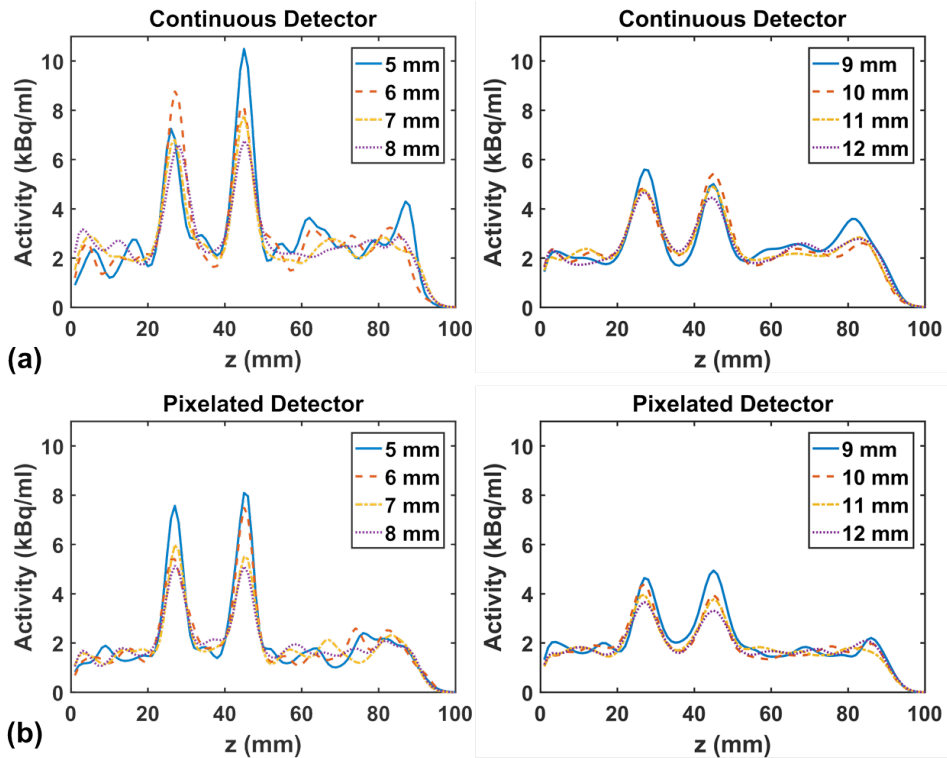
Figure 5-9 Profiles through the 6.0 mm lesions, with position as indicated in Figure 5-8, for 3.0 mm FWHM Gaussian filter. Different lines indicate different targeted system resolutions. (a) Profiles obtained with 3.2 mm intrinsic resolution continuous NaI(Tl) detector, (b) for 1.6 mm pixelated CZT detector.
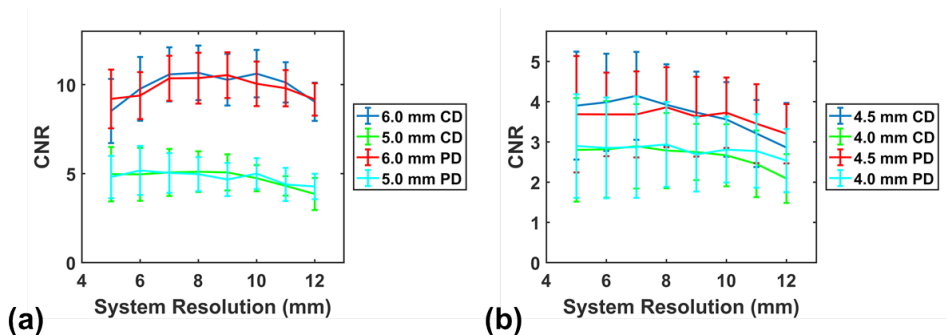
Figure 5-10 Plot of best CNR for each system resolution for (a) the 6.0 and 5.0 mm lesions and (b) the 4.5 and 4.0 mm lesions. Maximum taken over iterations 5 to 32 and filters from 0 to 10 mm FWHM, as indicated in table 2 and 3. The different lines represent the different lesion sizes and detector types (Continuous Detector (CD) and Pixelated Detector (PD)) and the error bars are the standard deviation in CNR for the 20 noise realisations.

collimator plates, but the background also contains more noise, especially close to the collima-tor. The shown images for each system are for the noise realisation with CNR closest to the me-dian for that system. Profiles through the 6.0 mm lesions are shown in Figure 5-9 for a fixed 3 mm filter and the 50th percentile noise realization, i.e. the image shown in Figure 5-8. When the targeted system resolution is worse, contrast recovery is lower as can be expected. Figure 5-10 shows the optimum CNR for each simulated system. We infer from Figure 5-10 that for the 6.0 mm lesion, the highest CNR is achieved by the 7 mm to 10 mm system resolution systems. Moreover, we see for none of the lesions sizes any clear difference between the continuous and pixelated detector systems. Note that 5.0 mm lesions have CNR values close to the detection limit (CNR of 4-5 as given by the Rose- criterion (Currie, 1968; Rose, 1973; Cherry et al., 2012)), while the smallest lesions score clearly below the limit for all systems.

5.4   Discussion

In this paper, we optimized focusing multi-pinhole configurations in order to find the geometry that achieves the highest spatial resolution-sensitivity trade-off.

Ideally, one would like to choose the system that is best suited for the imaging task at hand, which in this case is tumour detection. To determine detectability a numerical observer like the channelized Hotelling observer that mimics human observers is often used. However, a proper evaluation requires a huge number of noise realizations per system, making such a comparison computationally very expensive. A preliminary test indicated several hundreds of noise realiza-tions per system would be required for MBT. We estimate that using 40 processor cores, this would take at least several years of simulations, which is prohibitively long for the scope of the current research project.

The tumour-to-background contrast-to-noise (CNR) ratio that we used is also linked to de-tectability via the Rose-criterion (Currie, 1968; Rose, 1973; Cherry et al., 2012) and a relevant indicator for the possibility to use quantification to find heightened uptake regions. Moreover, CNR does not require many noise realizations and can quickly be calculated for many systems, iterations and filter levels. Therefore, we compare the CNR for optimized geometries with dif-ferent fixed system resolutions.

In this paper, we only maximised sensitivity for a whole breast imaging sequence. In our earlier work, we showed that focusing on a lesion can significantly improve the CNR. Ideally one would like to focus on each lesion in the optimization study. However, this would require 4 times more simulations than for the whole breast optimization. The computational time required for all the simulations for this paper was already very high (i.e. almost 2 months on several multi-CPU systems totalling 80 cores), so more simulations were deemed infeasible for now. We do report the sensitivity that can be achieved in focusing mode in Table 5-2 and Table 5-3. These sensitivities are as reached by the optimal system for whole breast imaging.

The design used in our earlier work (van Roosmalen et al., 2016), was not optimized. The initial design was based on a system resolution of 5.8 mm and had a sensitivity of 0.033%, which is very similar to the 6.0 mm system resolution system from this paper. We here see that by trading a bit of resolution for sensitivity a higher CNR can be reached.

Overall, the different systems for the system resolutions of 7 to 10 mm show minor differences in performance in terms of CNR. One notes that for 7 mm system resolution optimal CNR is obtained with a filter of 4 mm FWHM, and for 10 mm system resolution a filter of 1 mm or 2 mm is preferable for the continuous and pixelated detectors respectively. So, it seems that one can choose between higher resolution systems with more post-filtering or lower resolution system with a smaller post filter, within this range. The two detector types give very similar results, but as continuous detectors are much cost effective, the continuous NaI(Tl) based detector seems to be the best choice.

We think that in future work it may be worth to compare other focusing collimators such as fan beam or slit-slat collimators (Daekwang and Metzler, 2012) with the focusing pinhole geometries considered in this work.

5.5   Conclusion

We found that the optimal pinhole collimator for molecular breast tomosynthesis for the detection of 6.0 mm lesions uses a system resolution in the 7 to 10 mm range. Use of either a 3.2 mm intrinsic resolution continuous detector or a 1.6 mm pixels pixelated detector did barely influence the results.

5.6   Acknowledgements

Chapter 6

Comparison of fan beam, slit-slat and multi-pinhole collimators for Molecular Breast Tomosynthesis

Abstract

Recently, we proposed and optimized dedicated multi-pinhole molecular breast tomosynthesis (MBT) that images a lightly compressed breast. As MBT may also be performed with other types of collimators, the aim of this paper is to optimize MBT with fan beam and slit-slat collimators and to compare its performance to that of multi-pinhole MBT to arrive at a truly optimized design. Using analytical expressions, we first optimized fan beam and slit-slat collimator parameters to reach maximum sensitivity at a series of given system resolutions. Additionally, we performed full system simulations of a breast phantom containing several tumours for the optimized designs. We found that at equal system resolution the maximum achievable sensitivity increases from pinhole to slit-slat to fan beam collimation with fan beam and slit-slat MBT having on average a 48% and 20% higher sensitivity than multi-pinhole MBT. Furthermore, by inspecting simulated images and applying a tumour-to-background contrast-to-noise (CNR) analysis, we found that slit-slat collimators underperform with respect to the other collimator types. The fan beam collimators obtained a similar CNR as the pinhole collimators, but the optimum was reached at different system resolutions. For fan beam collimators, a 6 to 8 mm system resolution was optimal in terms of CNR, while with pinhole collimation highest CNR was reached in the 7 to 10 mm range.

6.1   Introduction

Several molecular imaging systems dedicated to breast imaging have recently emerged that can detect sub-centimetre lesions with high sensitivities (Abreu et al., 2006; Brem et al., 2008; Hruska et al., 2008; Raymond et al., 2008; Luo et al., 2010). Clinical studies have already shown that molecular breast imaging may play a role as supplemental screening modality in addition to mammography (Rhodes et al., 2015; Shermis et al., 2016; Brem et al., 2016) and in monitoring the response to chemotherapy (Mankoff et al., 2002; Mitchell et al., 2013). (Hruska and O'Connor, 2013) and Fowler (2014) provide comprehensive overviews of molecular breast imaging modalities and Hruska (2016) gives an outlook into current and future developments.

In our group, we are investigating and optimizing a scanner to perform 3D imaging of single-gamma emitting tracer distributions in the breast (van Roosmalen et al., 2016; van Roosmalen et al., 2017) (**Chapters 2 & 5**). We showed that the proposed Molecular Breast Tomosynthesis (MBT) scanner equipped with multi-pinhole collimators could significantly improve tumour-to-background contrast-to-noise ratios (CNR) over those of planar systems that also image mildly compressed breasts (van Roosmalen et al., 2016). We subsequently optimized sensitivity of multi-pinhole geometries for a range of fixed system resolutions (van Roosmalen et al., 2017). We found that the geometries with system resolutions in the 7.0 mm to 10.0 mm range gave best results in terms of TB-CNR for small lesions (4.0 to 6.0 mm) in a breast shaped phantom.

Moreover, the simulations showed no significant differences for the scanner's performance when it was equipped with either a continuous NaI(Tl) based detector or a pixelated CZT detector.

Although the use of pinholes in MBT gave promising results, pinhole collimation is not the only option available. For situations in which the imaging field-of-view (FOV) is smaller than the detector size –which is the case for MBT- a converging collimator geometry such as a fan beam or cone beam is also often used (Moore et al., 1992; Formiconi et al., 2004; Weinmann et al., 2009; Capote et al., 2013). Compared to parallel-hole collimation, converging collimators can improve the sensitivity by utilizing the whole detector surface. Moreover, the slanting of the holes allows for the object to be seen from multiple angles which is necessary if one wants to extract 3D information. For MBT, the appropriate converging collimator would be a fan beam collimator, as in the anterior direction the detector is not larger than the largest breast the scanner should accommodate. A second type of collimator that may be of interest for MBT is the slit-slat collimator as it combines properties of both pinhole and fan beam or parallel hole collimators (Daekwang and Metzler, 2012).

The aim of this paper is to compare performance of multi-pinhole, fan beam and slit-slat collimation for MBT. To this end, we first analytically optimize sensitivity of fan beam and slit-slat collimators at a range of fixed system resolution (5 – 11 mm). We subsequently compare the performance of these optimized geometries in full system simulations with the earlier optimized multi-pinhole designs.

6.2 Methods

In this section, we describe the basic design of MBT, the optimization process and how we evaluate the results. In general, we follow the same methodology as in our earlier pinhole optimization study (**Chapter 5**) in which more details can be found.

6.2.1 Molecular Breast Tomosynthesis

In the recently proposed MBT scanner (Beekman, 2014; van Roosmalen et al., 2016), the patient lies prone on a specially designed bed with the mildly compressed breast pendant through a hole and with the scanner underneath as schematically shown in Figure 6-1. In our initial MBT design, two Tungsten plates served as collimators each containing 63 pin-holes in a focused arrangement. The focused design gives the MBT scanner the unique ability to scan a user-defined volume-of-interest (VOI), which is beneficial as it increases the count yield from the VOI (Beekman et al., 2005; van der Have et al., 2009). To image any volume, the FOV has to be translated over the breast such that the desired scan volume is viewed over a range of angles (Vastenhouw and Beekman, 2007; Vaissier et al., 2012). In MBT this FOV translation is done by synchronized step-and-shoot movement of the collimators and detectors in a plane parallel to the compression plates, i.e. the collimators and detector are translated along both the anterior-posterior and the left-right axes to form a grid of scanning positions. During iterative

image reconstruction, all available projection data from all positions is used to reconstruct the 3D MBT image (Vastenhouw and Beekman, 2007).

6.2.2 *Previous pinhole optimization*

In a recent work, we optimized sensitivity of multi-pinhole designs for a range of fixed system resolutions and compared simulated images of a tumour-containing digital breast phantom for these optimized designs (van Roosmalen et al., 2017). We found that the geometries with system resolution in the range of 7.0 mm to 10.0 mm gave optimal results in terms of TB-CNR. This was true both for MBT with conventional gamma detectors based on a continuous NaI(Tl) scintillator read out by PMTs (3.2 mm intrinsic resolution) and pixelated detectors (1.6 mm pixels), with no significant differences between them. Therefore, in this work we only evaluate MBT using continuous NaI(Tl) detectors, as these are much more cost effective than pixelated detectors. In the results section of this work we present results from the previous pinhole optimization study in order to compare multi-pinhole with fan beam and slit-slat collimation.

6.2.3 *System design for fan beam and slit-slat collimators*

We restrict the collimator-detector geometries in our optimization such that they fit into the previously presented MBT concept in which a lightly compressed breast is imaged with two focusing collimators that each project onto a gamma detector.

6.2.3.1 *General considerations for collimator design.*

For both fan beam and slit-slat collimation, we restrict ourselves by the following design principles:
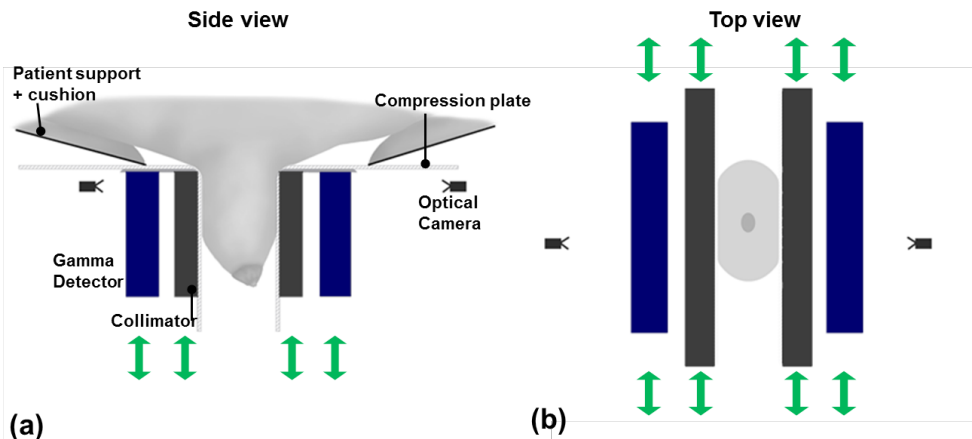
Figure 6-1 Schematic illustration of the geometry of the MBT scanner including compression plates, collimators, and gamma detectors. a) Side view showing breast of a woman lying prone on the scanner table. The breast is placed in the opening in the bed and slightly compressed. b) Top view of the breast between the transparent compression plates (artist impression). Note that details on collimator geometry are not shown here as we will investigate different types of collimators in this work.

1.   Due to the light compression of the breast used in MBT, we account for a minimal distance of 4 mm between the breast and the collimator face to accommodate the 4 mm thick compression plates.

2.   We assume a conventional gamma camera based on a NaI(Tl) scintillator and PMT readout (3.2 mm intrinsic resolution) with fixed detector size of 250 x 150 mm.

3.   We compare focused collimator designs that enable scanning of VOIs smaller than the whole breast as targeted imaging allows increasing the local count yield. We control the amount of focusing such that the FOV is comparable to that of the earlier pinhole collimators. Below we explain for each collimator type how this is achieved.

4.   The septal thickness must be sufficiently large to prevent septa penetration by the 140 keV gamma photons as emitted by [99m]Tc. For this, we use the rule provided by (Gunter, 1996). To make sure that the collimators are manufacturable we impose a minimum septal thickness of 0.3 mm.

6.2.3.2 Fan beam specific considerations for collimator design.

In the anterior direction, our detector is not much larger than the average breast (110 mm, see section 2.5.1), and smaller than the size of the largest breasts (at least up to 200 mm (Scopinaro *et al.*, 1999)). Therefore we do not focus in the sagittal plane but only in the coronal plane, which means that we use a fan beam collimator rather than a cone beam geometry. A fan beam collimator can be fully characterised by a small set of parameters, listed in Table 6-1 and depicted in Figure 6-2. We control the amount of focusing by fixing the focal length of the fan beam
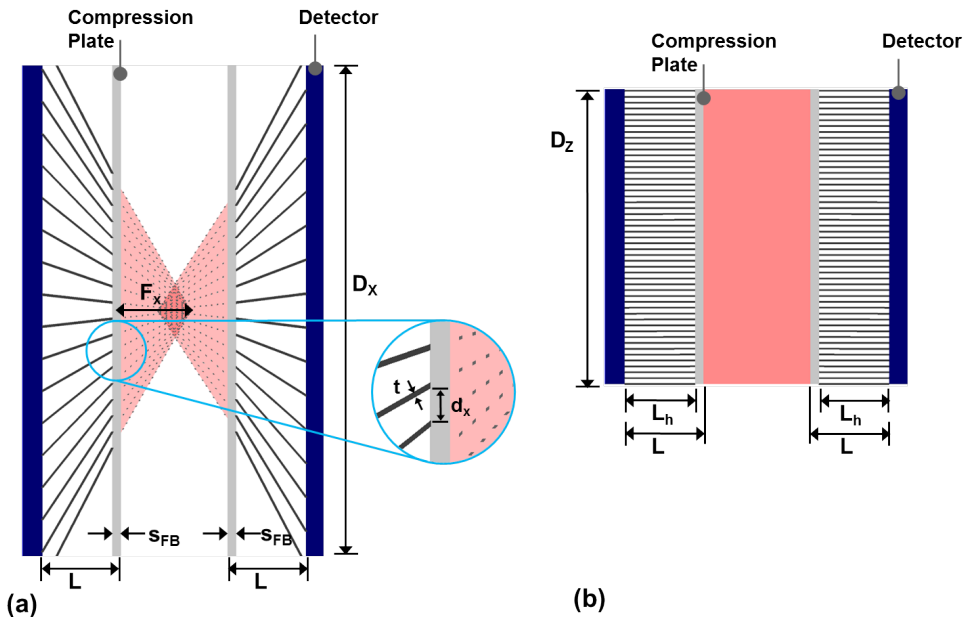

Figure 6-2 Example of a fan beam configuration. Two views are shown: (a) a coronal plane cross section and (b) a sagittal plane cross section. The detector, FOV, transparent compression plates and the collimators are indicated with blue, red, light grey, and dark grey respective-ly. Different parameters used are shown in the figure

Table 6-1 List of parameters for fan beam collimated geometries

Parameter	Description	Value	Varied/Fixed
L	[mm] Detector-breast distance		Free
L_h	[mm] Length of holes		L-s_{FB}
D_x, D_y	[mm] Dimensions of the detector	250, 150	Fixed
F_x	[mm] Focal distance in coronal plane, from collimator surface	40	Fixed to enable focused scanning
R_i	[mm] Intrinsic spatial resolution of detector	3.2	Fixed
R_t	[mm] Targeted system resolution	5, 6, 7, 8, 9, 10, 11	We optimize for several values
t	[mm] Septa thickness	>=0.3	Minimum imposed, further determined by Gunter's penetration criterion
d_x, d_y	[mm] Hole diameter		Calculated to keep system resolution constant
s_{FB}	[mm] Distance breast to collimator face	4	Fixed at minimal feasible value

Table 6-2 List of parameters for slit-slat collimated geometries

Parameter	Description	Value	Varied/Fixed
L	[mm] Detector-breast distance		Free
D_x, D_y	[mm] Dimensions of the detector	250, 150	Fixed
F_x	[mm] Focal distance in coronal plane, from collimator surface	40	Fixed to enable focused scanning
R_i	[mm] Intrinsic spatial resolution of detector	3.2	Fixed
R_t	[mm] Targeted system resolution	5, 6, 7, 8, 9, 10, 11	We optimize for several values
t	[mm] Septa thickness	>=0.3	Minimum imposed, further determined by Gunter's penetration criterion
d_y	[mm] Hole diameter		Calculated to keep system resolution constant
w	[mm] Slit width		Calculated to keep system resolution constant
α	Slit opening angle		Calculated to keep size of central projection 25 mm, same value set for all slits
s_{SS}	[mm] Distance breast to slit centre	6	Fixed at minimal feasible value

collimators to the value of 40 mm. This makes the FOV comparable to that of the optimized pinhole collimators in Van Roosmalen *et al.* (2017).

6.2.3.3 Slit-Slat specific considerations for collimator design.

The parameters for slit-slat collimators are listed in Table 6-2, and illustrated in Figure 6-3. The plate containing the slits is made of 6 mm thick tungsten, which provides sufficient stop-ping power for 140 keV photons letting through a fraction of 1.5×10^{-9}. The slats cover the whole space between the plate with slits and the detector. The slits are placed in the coronal plane, in exactly the same focusing arrangement as the pinholes in van Roosmalen et al. (2017) meaning that they are directed such that (i) they focus on a line 40 mm from the collimator (see Figure 6-3) and (ii) they result in non-overlapping tiled projections. Generally, increasing the opening angle α of the slits will allow for less slits to be used (because of the requirement of non-overlapping projections) but will also lead to a larger volume sensitivity per slit as the FOV for each slit becomes larger. Initial simulations showed that these effects largely cancel out meaning that the choice of α does not have a large influence on the resolution-sensitivity trade-off. Therefore, α of all slits is set to the same value such that the central slit's projection is 25 mm wide, which results in a constant number of 7 slits for all configurations. This is similar as done in the pinhole optimization study (**Chapter 5**).

For every change in the geometry, e.g. a different *L*, the slits should be repositioned to fully cover the detector with non-overlapping projections. For this, an automatic placement script was used
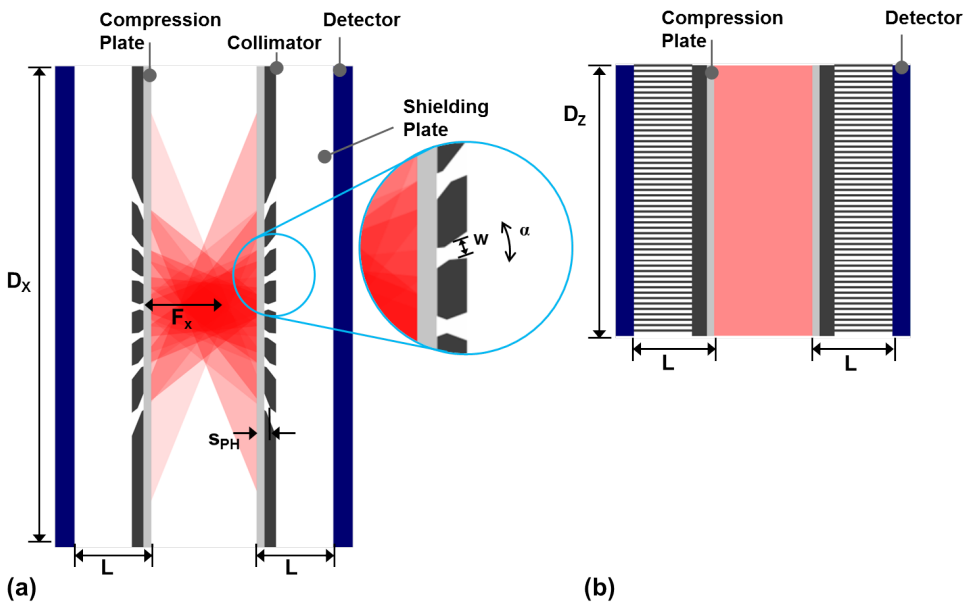

Figure 6-3 Example of a slit-slat beam configuration. Two views are shown: (a) a coronal plane cross section and (b) a sagittal plane cross section. The detector, FOV, transparent compression plates and the collimators are indicated with blue, red, light grey, and dark grey respectively. Different parameters used are shown in the figure.

in a similar way as for pinhole geometries. This was described in detail in Chapter 5 and van Roosmalen et al. (2017).

6.2.4   *Analysis of different collimators based on sensitivity-resolution trade-off*

We start the analysis of different geometries with an analytical optimization in which the sensitivity is maximized at fixed system resolution. We choose a range of different target system resolutions ranging from 5 to 11 mm. This range was chosen to encompass the optimal range of 7 to 10 mm found earlier for pinhole collimation. For each system resolution the fan beam and slit-slat designs with the highest sensitivity were selected and further analysed with full system simulations. After analysing these full system simulations, we assured that the optimal system was within the chosen resolution range.

We report sensitivity averaged over the breast shaped region described in section 6.2.6.1. In our design in which the detector and collimator are translated over a sequence of positions, sensitivity depends on the sequence chosen, which is provided in section 6.2.5. A sensitivity-weighted averaged resolution is determined over the same region, and the hole diameters, inter-slat distance and/or slit width are iteratively adjusted until the desired target system resolution is reached. The initial dimensions for this process are found by inverting the appropriate analytical resolution formula given below for the centre voxel.

6.2.4.1   *Fan beam specific analysis*

Sensitivity formulas traditionally used for converging collimators diverge near the focus (Formiconi, 1998) and as we focus within the breast these cannot be used. We therefore use a recently derived expression to determine sensitivity (van Roosmalen and Goorden, 2017) (**Chapter 4**) which we do not reproduce here due to its length.

The resolution for a fan beam collimator is different in the vertical and horizontal direction and for each direction given by (Moyer, 1974)

$$R_{FB} = \sqrt{\frac{R_i^2 \left(F - z_0\right)^2}{\left(F + L_e\right)^2} + d^2 \frac{\left(z_0 + L_e\right)^2}{Le^2} \frac{\left(F + \frac{L_e}{2}\right)^2}{\left(F + L_e\right)^2} \frac{1}{\cos^2 \theta_{FB}}} \tag{6-1}$$

where F is the focal distance for this collimator dimension, which in our case is F_x in the coronal plane and infinite in the other direction, z_0 is the distance from the collimator face, diameter d is either d_x or d_z depending on the direction and θ_{FB} is the angle between the collimator axis and the line from the focus to the position where resolution is to be determined. The effective collimator length $L_e = L_h - 2/\mu$ incorporates the effect of septal penetration via linear attenuation coefficient μ of the collimator material which is 3.39 mm^{-1} for Tungsten which is the material assumed for all MBT collimators.

6.2.4.2 Slit-slat specific analysis.

For sensitivity appropriate expressions have been derived in Accorsi *et al.* (2008). The authors recommend using different approximations in different parts of the FOV, and we calculated sensitivity this way. As this involves several lengthy expressions we do not reproduce the sensitivity equations here. As for resolution, in the coronal plane the same formula as for pinhole resolution is to be used which reads

$$R_{PH} = \sqrt{w_e^2 \left(1 + \frac{1}{M}\right)^2 + \left(\frac{R_i}{M}\right)^2}, \tag{6-2}$$

where M is the magnification factor of the slit (i.e. the ratio between distance from source to slit, and slit to detector), and we the effective slit-width given by Accorsi *et al.* (2008) as

$$w_e = w + \frac{\ln 2}{\mu}\left(\tan^2\frac{\alpha}{2} - \cot^2\theta_{ss}\right)\cot\frac{\alpha}{2}\sin\phi_0. \tag{6-3}$$

Here θ_{ss} is the angle between the plane of the slit and the line from slit to source, and ϕ_0 the incidence angle from the source through the centre of the slit onto the detector.

In the sagittal plane, the resolution is governed by the slats and can be calculated using the converging collimator expression as given in (6-1) with an infinite focal length (which is just the common parallel hole resolution formula).

6.2.5 Sampling and scan positions.

As mentioned above, the scan volume of MBT can be selected by the user and the collimator-detector pairs are then moved over a sequence of positions in a plane parallel to the compression plates in order to scan the VOI. In principle, the scan sequence should be adjusted to the size of the breast that is scanned and the shape of the FOV which is different for both types of collimators. However, as we compare a large number of designs and need to be sure we compare them equally we use a single set of sequences for all designs for both collimator types. In the sagittal plane, both collimators apply slats (see Figure 6-2 and Figure 6-3). In regions close to the collimator where the surface of the breast is located, the sensitivity just in front of the septa will be strongly reduced compared to that in front of the holes. Therefore, we move the collimator and detector 1 mm in the anterior direction for a second position so that every position is in front of the holes at least once. Furthermore, in the posterior position the collimators and detectors are moved from left to right in 4 mm steps from -76 to 76 mm while in the anterior position, the left to right steps are 8 mm from -74 to 74 mm. The bigger step size in the anterior position is to keep the number of bed positions low. Note that the positions in the anterior position are staggered compared to those in the posterior position; this improves the uniformity of the sampling. Note that by moving the collimator over the breast, angular coverage in the coronal plane is increased to a maximal full angle coverage that can be approximated by *2 arctan(D_x/2)/(F_x+L)* (see Figure 6-2 and Figure 6-3). We will provide this angle for all simulated designs.
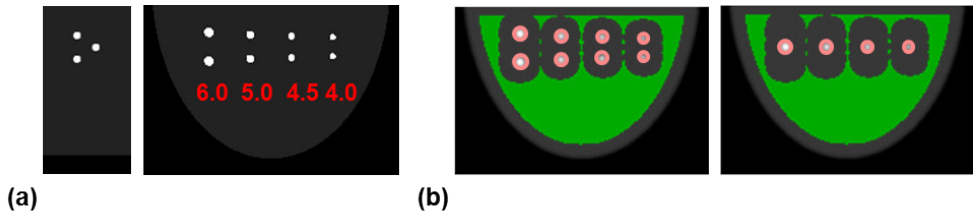
Figure 6-4 Slices through the breast phantom (a) left: slice parallel to sagittal plane through the 6.0 mm lesions, right: transverse slice at depth of two lesions. Lesion sizes indicated. (b). Transverse slices with red circles indicate the regions-of-interest used to determine the tumour signal while the green area denotes the background region.

6.2.6   *Validation by simulations of breast phantom scans*

In the full system simulations we performed after the analytical optimization, we employed the same ray-tracing simulator (Wang et al., 2017) (**Chapter 3**) both to generate simulated projections as well as a system matrix for image reconstruction. As its input, the simulator uses the collimator modelled as a voxelized volume, with a voxel size of 1/24th mm. The depth-of-interaction in the scintillator, collimator penetration, detector efficiency and detector resolution are modelled. We assumed detector pixels of 1.072 mm in a 234x140-pixel grid.

Phantom projections (phantom voxel size 0.5 mm) were obtained with the raytracer cut off set at 1% (Wang et al., 2017). A uniform attenuation coefficient in the phantom of 0.0151 mm^{-1} valid for 140 keV photons in water was assumed. Phantom projections for each of the scan sequence positions were obtained, accounting for the scan time and adding Poisson distributed noise to each projection. We already showed that in our geometry torso scatter hardly affects images (Wang et al., 2017) and it is therefore not modelled in this paper.

Images were reconstructed on a 1.0 mm isotropic voxel grid using Maximum Likelihood Expectation Maximization (MLEM) (Shepp and Vardi, 1982) using a system matrix with 1.0 mm source voxel grid and a threshold of 2%. The discrepancy in grid size between phantom and reconstruction, and between cut off thresholds is to mimic a continuous activity distribution without any actual cut-off. Moreover, no attenuation correction was applied.

6.2.6.1   Breast phantom

In this paper, we use the same phantom as in our earlier work (van Roosmalen et al., 2016; van Roosmalen et al., 2017) which models the breast as half an elliptically shaped disk (Dong et al., 2011), with a 110 mm chest-to-nipple distance, a width of 150 mm, and a thick-ness of 55 mm. The phantom is placed such that the top of the activity is at the same place as the start of the useful field of view of the detector. We placed four sets with three lesions each in the phantom (6.0, 5.0, 4.5, 4.0 mm diameter), see Figure 6-4(a). Within each set the central lesion was placed at a depth of 22 mm, with the other two lesions at a depth of 33 mm. We assumed a background activity concentration of 3.7 kBq/mL, consistent with an injection of 925 MBq 99mTc-Sestamibi (Hruska et al., 2012; Mann et al., 2012) and a concentration of 37 kBq/ml in the lesions to give

a tu- $\overline{S}$ mour-background uptake ratio of 10:1 (Maublant et al., 1996; Lee et al., $\overline{B}$ 2004; Hruska and O'Connor, 2008; Sullivan et σ_B al., 2012). We set a scan time of 10 minutes.

6.2.6.2 Analysis of images

Besides visually inspecting different images, we compared different breast phantom images by calculating the CNR, given by

$$CNR = \frac{\overline{S} - \overline{B}}{\sigma_B} \tag{6-4}$$

Here is the average signal taken in a spherical region placed on top of the lesion, is the average signal in a background region, and is the standard deviation in the background region and serves as measure of the noise. The regions used are indicated in Figure 6-4(b). All simulations are repeated for 20 different noise realizations, and the average of the CNR values is reported

6.3   Results

6.3.1   Analytical optimization

After considering the design restrictions, both collimator types have only one free parameter left: the distance between the breast and the detector. All the other parameters are fixed, used to control resolution, or directly related to other parameters. For a range of system resolutions, the sensitivity as function of the distance between breast and detector is plotted in Figure 6-5. This figure shows the fan beam and slit-slat collimators optimized in this work as well as results for the pinhole collimators from the previous study (van Roosmalen et al., 2017). For all collimator types an optimal distance exists which depends on the system resolution. For slit-slat collimation we find optimal detector-breast distances varying between 30.0 and 42.5 mm similar to the range found for pinholes which was in between 32.5 and 60 mm, while for fan beam collimation these distances are smaller and are between 15 and 21 mm. Two opposing effects play a role; placing the detector closer by increases the solid angle covered which is beneficial for the sensitivity, while on the other hand the magnification decreases meaning that the hole sizes have to decrease to maintain resolution which in turn reduces the sensitivity. The sharp drop in
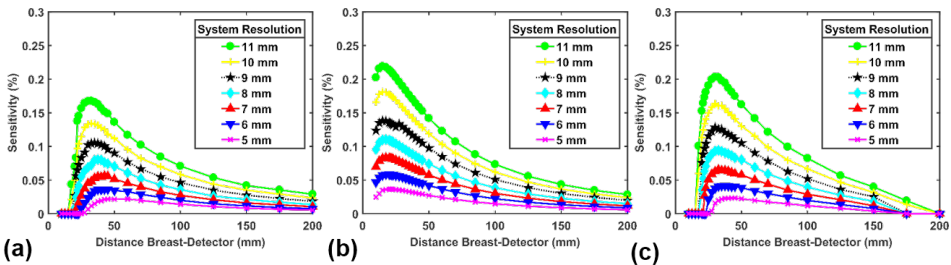
Figure 6-5 Sensitivity (averaged over the breast) for (a) pinhole, (b) fan beam, and (c) slit-slat collimators as function of distance between detector and breast and the lines indicate different system resolutions R_t (5, 6, 7, 8, 9, 10, and 11 mm).
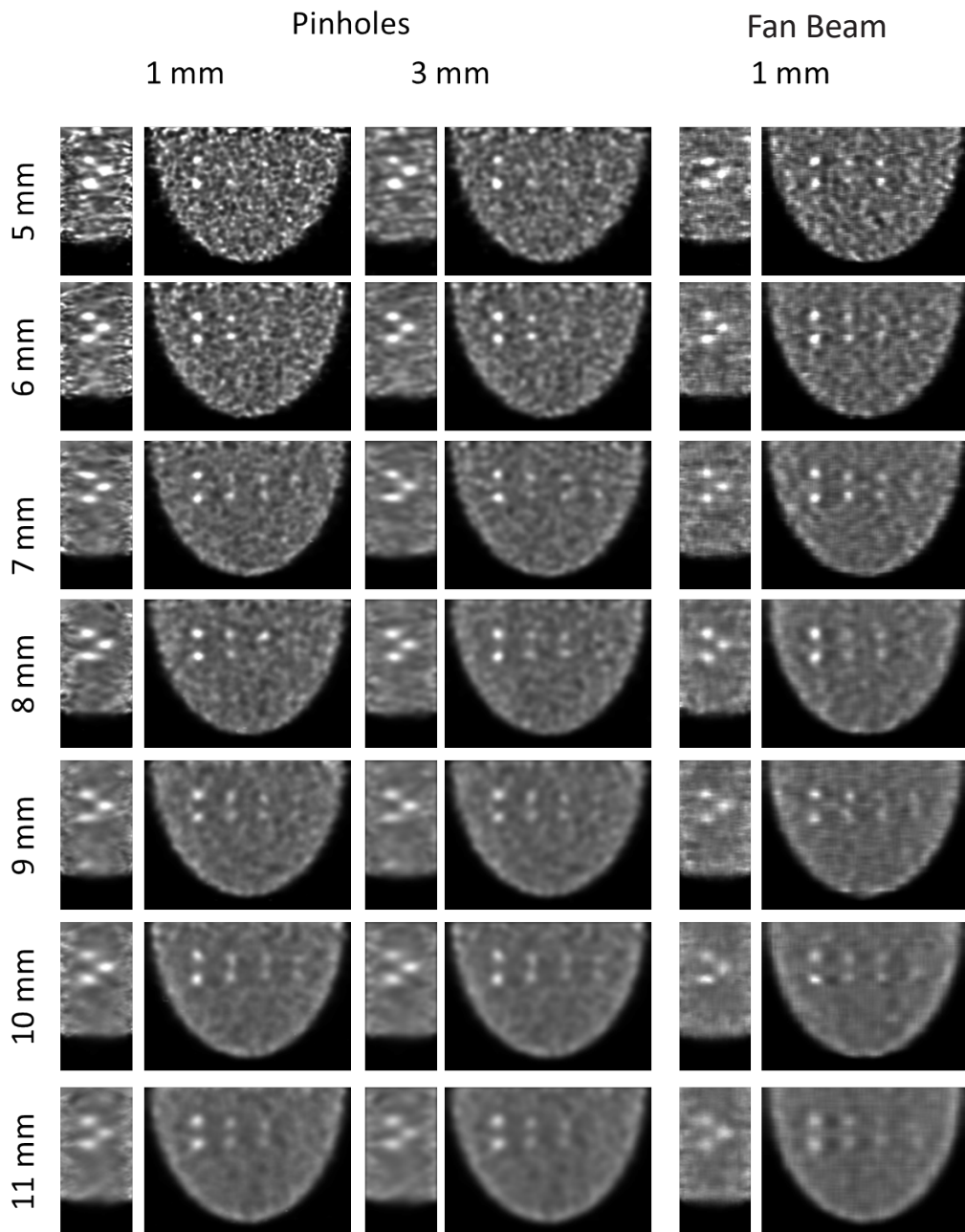
Figure 6-6 Simulated images of a breast shaped phantom containing lesions of 4.0, 4.5 , 5.0 and 6.0 mm. For each reconstruction two images are shown, a slice parallel to the sagittal plane through the 6.0 mm lesions, and a transverse slice. Each row represents a different target system resolution, while the different columns represent the different collimator types (pinhole, fan beam and slit-slat) and show 2 different filter levels (1.0 and 3.0 mm FWHM Gaussian filter). The number of iterations for each system is listed in tables 6-3, 6-4 and 6-5.

Fan Beam

Slit-Slat

3 mm

1 mm

3 mm
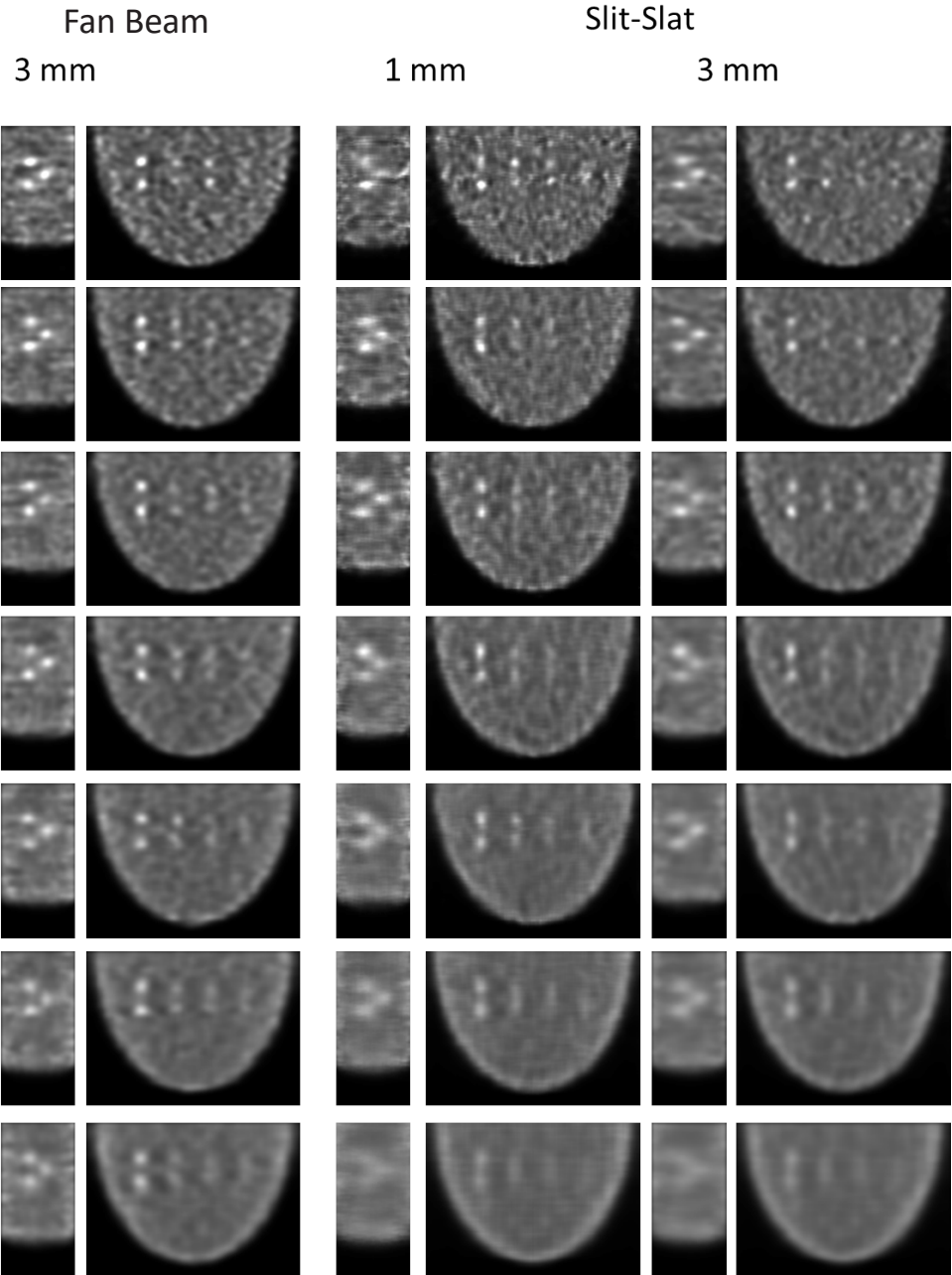
Table 6-3 Pinhole Configurations

System Resolution [mm]	5.0	6.0	7.0	8.0	9.0	10.0	11.0
Detector-breast distance [mm]	60	45	42.5	35	35	32.5	32.5
Pinhole Diameters [mm]	2.48	2.44	2.95	2.98	3.46	3.68	4.13
Angular range (degrees)	103	112	113	118	118	120	120
Volumetric sensitivity over the whole breast [%]	0.022	0.035	0.054	0.077	0.103	0.131	0.168
Sensitivity in focus [%]	0.087	0.130	0.191	0.259	0.346	0.424	0.520
Optimal iteration	11	14	16	17	17	19	20
Optimal filter FWHM [mm]	5	4	4	3	2	1	1
Optimal CNR	8.5	9.8	10.6	10.7	10.3	10.6	9.9
Standard deviation near chest wall (<5 mm)	0.49	0.47	0.37	0.37	0.34	0.29	0.28

Table 6-4 Fan Beam Configurations

System Resolution [mm]	5.0	6.0	7.0	8.0	9.0	10.0	11.0
Detector-breast distance [mm]	21	20	17.5	17.5	15	15	15
Hole diameters [mm] Horizontal/Vertical	1.68 / 1.11	1.86 / 1.36	1.82 / 1.43	2.03 / 1.64	1.85 / 1.55	2.09 / 1.77	2.27 / 1.95
Septa thickness [mm]	0.30 / 0.30	0.30 / 0.30	0.30 / 0.30	0.30 / 0.30	0.32 / 0.30	0.36 / 0.30	0.39 / 0.30
Angular range (degrees)	128	129	131	131	133	133	133
Volumetric sensitivity over the whole breast [%]	0.037	0.058	0.083	0.110	0.138	0.181	0.219
Sensitivity in focus [%]	0.167	0.273	0.397	0.539	0.684	0.839	1.002
Optimal iteration	16	17	19	22	22	22	25
Optimal filter FWHM [mm]	4	3	3	2	2	2	2
Optimal CNR	9.8	10.6	10.5	10.4	9.7	9.1	8.0
Standard deviation near chest wall (<5 mm)	0.33	0.33	0.31	0.30	0.29	0.27	0.28

Table 6-5 Slit-slat Configurations

| System Resolution [mm]	5.0	6.0	7.0	8.0	9.0	10.0	11.0
Detector-breast distance [mm]	42.5	37.5	32.5	32.5	30	30	30
Slit diameter [mm]	2.11	2.39	2.52	3.05	3.26	3.73	4.20
Hole diameter [mm]	1.77	2.12	2.30	2.70	2.87	3.23	3.59
Septa thickness [mm]	0.30	0.30	0.30	0.30	0.30	0.33	0.37
Angular range (degrees)	113	116	120	120	122	122	122
Volumetric sensitivity over the whole breast [%]	0.023	0.042	0.065	0.094	0.128	0.164	0.203
Sensitivity in focus [%]	0.101	0.169	0.241	0.346	0.443	0.561	0.687
Optimal iteration	13	17	23	28	28	32	32
Optimal filter FWHM [mm]	4	4	3	2	2	2	1
Optimal CNR	8.4	9.4	8.4	9.0	9.1	7.8	5.5
Standard deviation near chest wall (<5 mm)	0.29	0.29	0.31	0.30	0.29	0.29	0.24
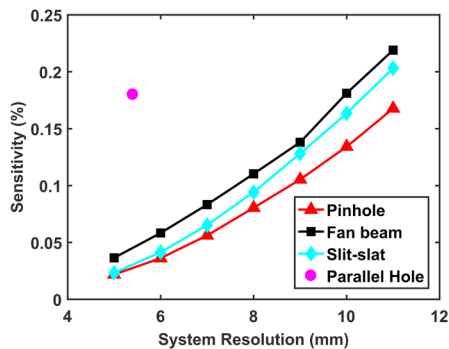
Figure 6-7 Plot of maximum reachable sensitivity as function of system resolution for pinhole, fan beam and slit-slat collimator. For each system resolution, the detector-breast distance that gives the highest sensitivity at that fixed resolution is used (maximum in Figure 6-5). For comparison a point (pink) is added showing an optimized parallel hole system from (Hruska et al., 2012)
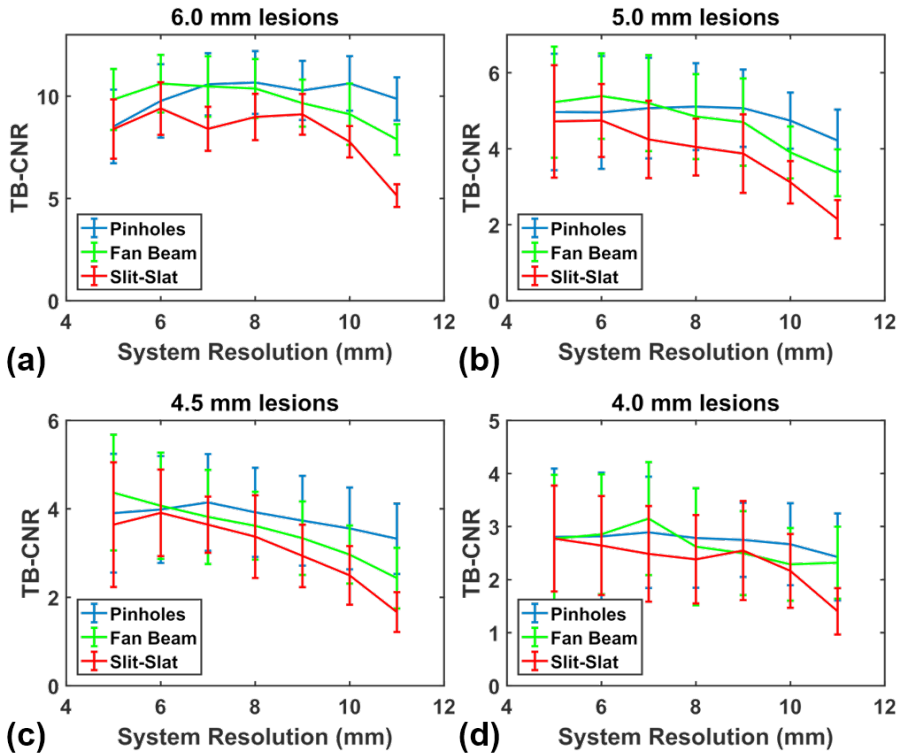
Figure 6-8 Plot of the best CNR for each system resolution, where the maximum is taken over iterations 5 to 32 and filters from 0 to 10 mm FWHM as indicated in Table 6-3, Table 6-4 and Table 6-5. The different lines represent the different collimator types and results are shown for (a) 6.0 mm lesions, (b) 5.0 mm lesions, (c) 4.5 mm lesions and (d) 4.0 mm lesions.

sensitivity for all collimator types when moving very close to the breast comes at the point that it becomes impossible to achieve the given fixed system resolution with that type of collimator. Apparently fan beam collimators can still achieve the target resolution at closer distances than pinhole or slit-slat collimators. The maximum achievable sensitivity as function of the system resolution is shown in Figure 6-7. This figure shows that both fan beam and slit slat collimators can achieve a higher sensitivity than the pinhole collimators at the same fixed system resolution, with the fan beam collimator having the highest sensitivity. At 5.0 mm system resolution, the optimal sensitivity of the slit-slat system is 8% higher than that of the pinhole systems, while the fan beam system has a 69% higher sensitivity. At 11.0 mm system resolution, the differences are 21% and 31% respectively. For comparison we show the resolution and sensitivity of the most sensitive parallel hole collimator from a highly optimized planar molecular breast imaging system (Hruska et al., 2012a). This system has much higher sensitivity than the other systems at equal system resolution, but of course it does not provide 3D information (see discussion section).

6.3.2 Full system simulations

Full system simulations were performed for each of the optimal configurations (maximum in Figure 6-5, and geometries summarized in Table 6-3, Table 6-4 and Table 6-5). The images depend on the number of iterations of MLEM used and the FWHM of the 3D Gaussian post-filter applied. We determined an optimal combination of iteration number and filter level in the following way: Gaussian filters with FWHM ranging from 0 to 8 mm (in 1 mm steps) were applied to all images and the iteration number and filter combination that lead to the highest CNR in the 6.0 mm lesions (on average over the noise realizations) was determined, requiring at least 5 iterations to ensure a minimum level of convergence. These optimal number of iterations and filter level and the resulting CNR are listed in Table 6-3, Table 6-4 and Table 6-5. The tables also list the noise (the standard deviation divided by the mean over all voxels) near the chest wall (top 5 mm of reconstructed images). For all collimators, this noise level reduces when sen-sitivity increases. For the majority of fixed system resolutions, the pinhole collimators lead to most noise near the chest wall, while fan beam and slit-slat have lower and comparable num-bers. For example, for a fixed 6.0 mm system resolution the pinhole system has a 48% and 69% higher chest wall noise level than the fan beam and slit-slat systems respectively. For the 10.0 mm system resolution this difference reduces to 7% and 0% respectively

Slices through reconstructed images are shown in Figure 6-6. From this figure, one can infer that in the saggital plane, the lesions are better recovered, i.e. more spherical, for the fan beam collimators than for the pinhole and slit-slat collimators which show more elongation. One possible explanation is that as the optimal fan beam collimators have the detector closer by, the angular sampling range (indicated in Table 6-3, Table 6-4 and Table 6-5 and discussed in section 6.2.5) may be larger resulting in better through-plane resolution.

In Figure 6-8, CNR curves are shown as function of system resolution. From this figure one can infer that the slit-slat collimators do not reach the same CNR as the other two collimator types. The reconstructed images in Figure 6-6 also indicate that slit-slat collimation provides a lower contrast than the other collimators. Furthermore, we see that th CNR results of the pinhole and fan beam collimators are close together for the largest lesions. For the 6.0 mm lesions, we concluded in our earlier work that the pinhole collimator optimum is reached for the 7 to 10 mm system resolution geometries with the absolute peak at a CNR of 10.7 for a fixed 8 mm system resolution. Fan beam collimators perform very similar, but with a small peak at 6 mm system resolution with a CNR value of 10.6. For the smaller lesions, we find that the higher resolution systems are more favourable. For the 5.0 mm lesions pinhole collimation leads to an optimal CNR of 5.1 at 8.0 mm system resolution while the fan beam has an optimum of 5.4 at 6.0 mm system resolution, compared to a CNR of 4.7 at 6.0 mm for the slit-slat collimator. For all simulations, we note that the spread between the noise realizations is large, with a trend to reduce for lower system resolutions.

6.4   Discussion

In this paper, we optimized focusing fan beam and slit-slat configurations in order to find the geometry that achieves the highest sensitivity at fixed system resolutions. We simulated the optimal systems and performed a CNR analysis to evaluate the spatial resolution-sensitivity trade-off. The CNR ratio is linked to detectability via the Rose-criterion (Currie, 1968; Rose, 1973; Cherry et al., 2012) and a relevant indicator for the possibility to use quantification to find regions with increased uptake. Moreover, CNR does not require a large number of noise realizations and can quickly be calculated for many systems, iterations and filter levels. Therefore, we were able to compare the CNR for optimized geometries with different fixed system resolutions.

In Figure 6-7, we also showed the resolution and sensitivity of a parallel hole collimator for a highly optimized planar molecular breast imaging system (Hruska et al., 2012). Note that such a parallel hole geometry only provides 2D information while the geometries considered in this paper result in 3D reconstructed images. Resolution in such reconstructed images can be higher than calculated system resolution. The same planar parallel hole geometry was simulated in an earlier comparison of MBT with planar molecular breast imaging (van Roosmalen et al., 2016). In that study, we showed that an MBT system with a 6 mm system resolution obtained a 110% higher CNR for 6.0 mm lesions than the planar imaging system despite the better sensitivity-system resolution trade off of the latter.

It is notable that two different collimator types (multi-pinhole and fan beam) show a very similar performance in terms of CNR all though sensitivity (at fixed system resolution) was higher for the fan beam collimator at the same system resolution (typically by 48%). This similarity in CNR is reached although the geometries of both collimators are clearly different; the pinhole collimators have a few holes accepting photons from many angles, while the fan beam collimators have many holes accepting photons from a small cone. Furthermore, the slit-slat collimators, which perform better than multi-pinhole collimators in terms of sensitivity-resolution trade-offs (on average slit-slat has 20% higher sensitivity), do worse on reconstructed images. This shows that collimator optimization is a complicated process and that the performance of a collimator depends on multiple factors such as resolution, sensitivity, size of the FOV and angular sampling over that FOV and that full system simulation are necessary for evaluation of different designs.

Scatter in the torso and in the breast can affect the images obtained with any breast imaging mo-dality. For the simulations in this study we did not model scatter, a decision based on earlier findings from Wang et al. (2017) (**Chapter 3**) in which we considered multi-pinhole MBT. In this previous paper, the reconstruction matrix was always obtained with a voxelized raytracer (as is done in this paper), but projections were either simulated with raytracing or with full Monte Carlo simu-lations (that included both scatter from the breast and scatter from the torso). We found that the images based on projections obtained with Monte Carlo simulations and corrected for scatter with the commonly used Triple Energy Window scatter correction method were very close to those obtained with raytracing. Combined with the superior speed of the voxelized

raytracer, we therefore decided to use raytracing for the current study and did not model scatter. In future research it is of interest to also investigate the influence of scatter on reconstructed images for a fan beam or slit-slat collimator geometry.

Note that to obtain similar images from an experimental MBT system as those simulated in this paper, system calibration is required to obtain accurate system matrices. These can e.g. be based on point source measurements like used for existing preclinical multi-pinhole SPECT (van der Have et al., 2008).

6.5   Conclusion

Results from this paper indicate that fan beam or pinhole collimators might be the best choice for collimation in the studied MBT set-up in terms of CNR while the slit-slat collimators performed significantly worse. Fan beam collimation may have the important advantage that it allows for better imaging near the chest wall.

Acknowledgements

Chapter 7

Thesis Summary & General Discussion

In this chapter, a summary with conclusions from this thesis is provided together with an outlook and recommendations for further research.

In this thesis, we developed tools to model and simulate single gamma imaging modalities. These tools were subsequently used to simulate and optimize a design for Molecular Breast Tomosynthesis (MBT). The chapters in this thesis can be divided into two groups. The first group consists of **Chapters 3 and 4** detailing technical topics concerning modelling and simulation of single gamma emitter imaging modalities, while the other chapters deal with MBT and its optimization. We will first discuss the chapters from the first group individually and then discuss the latter group.

Chapter 3 describes simulation software developed in our research group which is currently used for the simulation of small animal SPECT/PET systems and which in this thesis is applied to MBT. We conclude that the use of dedicated simulation software based on a voxelized raytracer (VRT) has many benefits over conventional Monte Carlo simulations like those enabled by the GATE simulation software package. In general, our dedicated software is orders of magnitude faster than more general software would allow, while still having flexibility in collimator design. VRT does not model scatter in either the patient or the collimator. We show that scatter can indeed be neglected for the MBT geometry even though there is substantial tracer uptake in heart and liver. For other designs or scanners, it would have to be checked beforehand if VRT would be sufficiently accurate.

A new mathematical expression for sensitivity of converging collimators is derived in **Chapter 4**. It can be used in the design and optimization of any system using a converging SPECT collimator. This new expression does not diverge near the focus as conventional expressions do, and is valid over the full field-of-view of the collimator. This allows accurate calculation of the sensitivity even for collimators with the focus close to or in the object of interest. Moreover, we conclude that if the object of interest is close to the collimator surface the exact location of the holes and septa have a large influence on the local sensitivity and full simulations are in order.

The other chapters in this thesis deal with our design for MBT. In **Chapter 2**, we introduced an initial focused multi-pinhole design and compared MBT with existing planar imaging modalities. We found that in a breast phantom containing different lesions, MBT improved tumour-to-background contrast-to-noise ratio (CNR) over planar MBI when scanning a whole breast. Much larger CNR improvements were found in scans focused on a specific breast region known to contain several lesions.

In **Chapter 5**, we optimized the pinhole geometry of our initial design, while in **Chapter 6** we considered using fan beam or slit-slat collimators which were also optimized. In all cases initially an analytical optimization was performed to maximize the sensitivity at a series of given fixed system resolutions. For each system resolution, the system with highest sensitivity was subsequently selected for a full system simulation. Using a CNR analysis we then determined which resolution

is optimal for lesions with sizes ranging from 4.0 to 6.0 mm. Based on the optimization studies we found a small improvement of optimized multi-pinhole MBT over our initial design. The fan beam collimators achieved the same CNR as the pinhole collimators but at slightly better system resolution (6.0 mm versus 7.0 to 10.0 mm), and in the reconstructed images there was less elongation of the spherical lesions in the dimension perpendicular to the collimator plates. The slit-slat collimators underperformed compared to both other collimators.

In the optimizations in **Chapters 5 and 6,** only small gains (around 10%) in CNR were found compared to the initial design. Therefore, the optimized systems are unlikely to compare significantly more favourably to the existing planar systems than the initial design does in **Chapter 2**. The 3D information provided by MBT could be valuable compared to planar MBI, and compared to existing planar imaging systems MBT offers a small benefit as far as CNR is concerned. Moreover, the results from **Chapter 2** show that the benefits of MBT are mostly found in its unique ability to perform focused scans on small areas of interest. MBT might be valuable in follow-up scans on areas with suspected lesions identified with other modalities. Therefore, it can be interesting to investigate in future research how fan beam collimators behave in focused scans, and to optimize the collimators specifically for a focused scanning use case.

Some topics came up in each of these chapters and warrant discussion in this concluding chapter. The first topic is detector choice for MBT. In **Chapter 5**, two different detector types were compared. The first was based on a continuous NaI(Tl) scintillator read out with PMTs resulting in an intrinsic resolution of 3.2 mm. The second was a pixelated CZT detector with 1.6 mm pixels. We found no differences in performance with respect to CNR or in the visual inspection of the reconstructed images. Therefore, we only used the NaI(Tl) based detector in **Chapter 6**, as it is much more cost-effective than CZT. While considering detectors, it is important to also consider the dead-edge of the detector, which is the area at the edge of the detector that is not providing useful information. Given the geometry of MBT in general, it is important to minimize this dead-edge to be able to scan as close to the chest-wall as possible. As indicated in several chapters, using maximum-likelihood processing of the PMT signals, it should be possible to reduce the dead-edge of the continuous NaI(Tl) based detectors. Prototypes and experiments will have to show what exactly will be achievable in practise. Moreover, it could be possible to investigate if small changes to the collimation geometry, like for example tilting the upper pinholes, or slanting the holes of the fan beam collimators, could help to image closer to the chest-wall. Care should be taken, to avoid the collimators looking directly at the heart or other organs with large tracer uptake.

The noise patterns observed in the MBT reconstructed images in **Chapters 2, 5 and 6** deserve some discussion. Very similar correlated noise patterns can be seen in the backgrounds of all the reconstructed images regardless of collimation type. Increasing the number of counts in the projections, or averaging of reconstructed images over different noise realizations, showed the patterns to reduce or disappear. Given the independence of collimation type, it suggests that the cause of these patterns is something more fundamental in the geometry. Possibly the

limited angular sampling, induces local correlations in the reconstructions. One might suggest investigating ways to provide additional sampling from other directions to reduce the patterns in the background noise. Unfortunately, this is made very difficult by the non-constant distance between the two collimator plates. The need to be able to scan patients with small breasts, limits the size of any side collimator/detector. At the same time, this would require extra shielding to prevent photons circumventing the collimators of these side detectors while scanning patients with larger breasts.

Hoofdstuk 7

Samenvatting van het proefschrift & Algemene Discussie

In dit hoofdstuk wordt een samenvatting met conclusies van dit proefschrift gegeven samen met een vooruitblik en aanbevelingen voor verder onderzoek.

In dit proefschrift hebben we methodes ontwikkeld voor het modelleren en simuleren van afbeeldingtechnieken voor gamma-uitzenders. Deze methoden zijn vervolgens gebruikt voor het simuleren en optimaliseren van een ontwerp voor Molecular Breast Tomosynthesis (MBT, moleculaire borst tomografie). De hoofdstukken in dit proefschrift kunnen in twee groepen worden verdeeld. De eerste groep bestaat uit **hoofdstukken 3 en 4** die technische onderwerpen behandelen met betrekking tot modellering en simulatie van afbeeldingstechnieken voor gamma-uitzenders, terwijl de andere hoofdstukken MBT en de optimalisatie daarvan beschrijven. We zullen eerst de hoofstukken uit de eerste groep individueel bespreken en dan de tweede groep bediscussiëren.

Hoofdstuk 3 beschrijft de simulatiesoftware die in onze onderzoeksgroep is ontwikkeld en welke nu gebruikt wordt voor de simulatie van SPECT/PET-systemen voor kleine proefdieren. Deze software wordt in dit proefschrift toegepast op MBT. We concluderen dat het gebruik van speciale simulatie software gebaseerd op een voxelized raytracer (VRT, een op voxels gebaseerde raytracer) vele voordelen heeft boven conventionele Monte Carlo simulaties zoals die mogelijk gemaakt worden door bijvoorbeeld het GATE-simulatiesoftwarepakket. In het algemeen is onze speciale software enkele ordegroottes sneller dan algemene software zou toestaan, terwijl het nog steeds flexibel is in collimator ontwerp. De verstrooiing in de patiënt of de collimator wordt in VRT niet gemodelleerd. We laten zien dat verstrooiing inderdaad verwaarloosd kan worden voor de MBT-geometrie ondanks de substantiële opname van de tracer in het hart en de lever. Voor andere ontwerpen of scanners zal van tevoren gecontroleerd moeten worden of VRT accuraat genoeg is.

Een nieuwe wiskundige uitdrukking voor de gevoeligheid van convergerende collimators wordt afgeleid in **hoofdstuk 4**. Deze kan gebruikt worden bij het ontwerpen en optimaliseren van elk systeem dat gebruikmaakt van een convergerende SPECT-collimator. Deze nieuwe uitdrukking divergeert niet nabij de focus zoals de conventionele uitdrukkingen doen, en is geldig over het hele gezichtsveld van de collimator. Hierdoor is het mogelijk nauwkeurige berekeningen te maken van de gevoeligheid zelfs voor collimators met de focus dichtbij of in het object dat wordt bestudeerd. Bovendien, concluderen we dat als het object dicht bij het oppervlak van de collimator is, dat dan de exacte locatie van de gaten en de septa een grote invloed hebben op de lokale gevoeligheid en volledige simulaties noodzakelijk zijn.

De andere hoofdstukken in dit proefschrift gaan over ons ontwerp voor MBT. In **hoofdstuk 2** introduceren we een eerste gefocust multi-pinhole ontwerp en vergelijken we MBT met bestaande plenaire afbeeldingsmodaliteiten. We vonden dat in een borst fantoom met verschillende tumoren, MBT de tumor-tot-achtergrond contrast-tot-ruis verhouding (CNR) verbetert ten opzichte van plenaire MBI wanneer we een hele borst scannen. Veel grotere CNR-verbeteringen

zijn gevonden in scans die focussen op een specifieke regio van de borst waarvan bekend is dat er verschillende tumoren zitten.

In **hoofdstuk 5** optimaliseren we de pinhole geometrie van ons initiële ontwerp, terwijl we in **hoofdstuk 6** overwogen om geoptimaliseerde fan-beam of slit-slat collimators te gebruiken. In alle gevallen, is eerst een analytische optimalisatie uitgevoerd om de gevoeligheid te maximaleren voor een reeks van gegeven vaste systeemresoluties. Voor elke systeemresolutie hebben we het systeem met de hoogste gevoeligheid vervolgens geselecteerd voor een simulatie van het complete systeem. Met behulp van een CNR-analyse hebben we bepaald welke resolutie optimaal is voor tumoren met afmetingen van 4.0 tot 6.0 mm. Gebaseerd op optimalisatie studies vonden we een kleine verbetering van geoptimaliseerd multi-pinhole MBT over ons initiële ontwerp. De fan-beam collimators bereikte dezelfde CNR als de pinhole collimators maar bij een iets betere systeemresolutie (6.0 mm tegenover 7.0 tot 10.0 mm), en in gereconstrueerde beelden was er minder uitsmering van de bolvormige tumoren in de richting loodrecht op de collimator platen te zien. De slit-slat collimators onderpresteerden vergleken met de beide andere collimators.

In de optimalisaties in **hoofdstukken 5 en 6,** vonden we maar kleine verbeteringen (rond 10%) in CNR vergeleken met het initiële ontwerp. Daarom is het onwaarschijnlijk dat de geoptimaliseerde systemen significant gunstiger uit de vergelijking met bestaande plenaire systemen zouden komen dan het initiële ontwerp doet in **hoofdstuk 2**. De 3D informatie geleverd door MBT kan waardevol zijn vergeleken met plenaire MBI, en vergeleken met bestaande plenaire systemen biedt MBT een klein voordeel wat betreft CNR. Bovendien laten de resultaten van **hoofdstuk 2** zien, dat de voordelen van MBT vooral gevonden worden in zijn unieke mogelijkheid om gefocuste scans op kleine gebieden van interesse uit te voeren. MBT kan dus waardevol zijn in opvolg scans van gebieden waar verdachte tumor zijn geïdentificeerd met andere modaliteiten. Daarom kan het interessant zijn om in de toekomst te onderzoeken hoe fan-beam collimators zich gedragen in gefocuste scans, en om de collimators specifiek te optimaliseren voor gefocuseerde scans.

In **hoofdstukken 5 en 6** wordt bijna dezelfde prestatie bereikt met geoptimaliseerde pinhole en fan-beam collimators. Dit suggereert dat het onwaarschijnlijk is dat verdere collimator optimalisatie nog significante verbeteringen kan opleveren voor MBT. Als men op zoek gaat naar radicale verbeteringen in prestatie, zal het nodig zijn om de aannames en algemene ontwerp restricties opnieuw te bekijken. Een totaal andere geometrie zou eventueel (maar niet noodzakelijkerwijs) kunnen leiden tot betere resultaten. Een ander mogelijk onderzoeksrichting zou zijn om te kijken wat andere reconstructiemethoden of filtertechnieken kunnen doen voor het verbeteren van de scans.

Een aantal onderwerpen kwamen in elk van deze hoofdstukken naar boven en verdienen discussie in dit concluderende hoofdstuk. Het eerste onderwerp is de detector keuze voor MBT. In **hoofdstuk 5** zijn twee verschillende detector typen vergeleken. De eerste was gebaseerd op een continue NaI(Tl) scintillator die werd uitgelezen door PMTs wat resulteerde in een intrinsieke resolutie van 3.2 mm. De tweede was een CZT-detector met discrete pixels van 1.6 mm. We

vonden geen verschillen in prestatie wat betreft de behaalde CNR of bij visuele inspectie van de gereconstrueerde beelden. Daarom hebben we alleen de detector die was gebaseerd op NaI(Tl) gebruikt in **hoofdstuk 6**, aangezien deze veel kosten-efficiënter is dan CZT-detectoren. Als men gebruik van verschillende detectoren overweegt, is het belangrijk ook te kijken naar de dode rand van de detector. Dit is het gebied aan de rand dat geen nuttige informatie oplevert. Vanwege de algemene geometrie van MBT is het belangrijk om deze dode rand zo klein mogelijk te maken om zo dicht mogelijk bij de borstwand te kunnen scannen. Zoals aangegeven in verschillende hoofdstukken, zou het met gebruik van maximale-waarschijnlijkheid verwerking van de PMT-signalen mogelijk moeten zijn om de dode rand van een continue op NaI(Tl) gebaseerde detector te verminderen. Prototypen en experimenten zullen moeten laten zien wat er haalbaar zal zijn in de praktijk. Bovendien zou het mogelijk kunnen zijn om te onderzoeken of kleine wijzigingen in het ontwerp van de collimator geometrie, zoals bijvoorbeeld het draaien van de bovenste pinholes of het schuin plaatsen van de gaten van de fanbeam collimators, kunnen helpen om dichter bij de borstwand te kijken. Er moet dan echter wel op worden gelet dat de collimators niet direct naar het hart of andere organen met grote zoekstof opname kijken.

De ruis patronen geobserveerd in MBT gereconstrueerde afbeeldingen in **hoofstukken 2, 5 en 6** verdienen enige discussie. Zeer verglijkbare gecorreleerde ruis patronen zijn zichtbaar in de achtergrond van alle gereconstrueerde afbeeldingen, onafhankelijk van collimator type. Het vergroten van de aantallen in de projecties, of het middelen van gereconstrueerde afbeeldingen over verschillende ruisrealisaties, laten zien dat de patronen verminderen of verdwijnen. Gegeven de onafhankelijkheid van het collimatortype, suggereert dit dat de oorzaak van deze patronen ligt in iets meer fundamenteels in de geometrie. Mogelijk veroorzaakt de beperkte hoekmonstering lokale correlaties in de reconstructies. Men zou kunnen aanbevelen te onderzoeken hoe extra bemonstering vanuit andere richtingen de patronen in de achtergrond kunnen verminderen. Helaas wordt dit bemoeilijkt door de niet contante afstand tussen de twee collimatorplaten. De noodzaak om patiënten met kleine borsten te kunnen scannen beperkt de afmetingen van elke collimator/detector aan de zijkant. Tegelijkertijd, zou extra afscherming nodig zijn om de voorkomen dat fotonen de collimator ontwijken tijdens het scannen van patiënten met grote borsten.

References

Abreu, M. C., *et al.* **2006.** *Design and evaluation of the clear-PEM scanner for positron emission mammography.* IEEE Trans Nucl Sci, 53(1), 71-77. doi: 10.1109/TNS.2006.870173

Accorsi, R. and Metzler, S. D. **2006.** *Non-diverging analytic expression for the on-axis sensitivity of converging collimators: analytic derivation.* Phys Med Biol, 51(21):5675–96.

Anger, H. O. **1964.** *Scintillation Camera with Multichannel Collimators.* J Nucl Med, 5(7), 515-531.

Anger, H. O. **1967.** *Radioisotope cameras.* In Hine, G. J., editor, *Instrumentation in Nuclear Medicine*, volume 1, chapter 19, pages 485–552. Academic Press, New York, NY, USA.

Assie, K., *et al.* **2005.** *Validation of the Monte Carlo simulator GATE for indium-111 imaging.* Phys Med Biol, 50(13), 3113-3125. doi: 10.1088/0031-9155/50/13/010

Badal, A., *et al.* **2009.** *Mesh-Monte Carlo Radiation Transport Simulation in a Triangle Mesh Geometry.* IEEE Trans Med Imag, 28(12), 1894-1901. doi: 10.1109/Tmi.2009.2021615

Baghaei, H., *et al.* **2010.** *A Breast Phantom Lesion Study With the High Resolution Transformable HOTPET Camera.* IEEE Trans Nucl Sci, 57(5), 2504-2509. doi: 10.1109/Tns.2010.2049585

Barrett, H. H. **1990.** *Objective assessment of image quality: effects of quantum noise and object variability.* J Opt Soc of Am A, 7(7), 1266-1278. doi: 10.1364/JOSAA.7.001266

Barrett, H. H., *et al.* **2009.** *Maximum-Likelihood Methods for Processing Signals From Gamma-Ray Detectors.* IEEE Trans Nucl Sci, 56(3), 725-735. doi: 10.1109/TNS.2009.2015308

Barrett, H. H., & Myers, K. J. **2004.** *Foundations of image science.* Hoboken, New Jersey: John Wiley & Sons.

Beekman, F. J. **2001.** *Apparatus for making tomographic images.* US Patent 6,324,258.

Beekman, F. J. **2011.** *Gamma radiation imaging apparatus* (Patent: US 20110158384, EP 2310876).

Beekman, F. J. **2014.** *Gamma radiation breast imaging apparatus* (Patent: US 14/044,019, NL 2009566).

Beekman, F. J., *et al.* **1998.** *Half-fanbeam collimators combined with scanning point sources for simultaneous emission-transmission imaging.* J Nucl Med, 39(11):1996–2003.

Beekman, F. J., *et al.* **1999.** *Efficient SPECT scatter calculation in non-uniform media using correlated Monte Carlo simulation.* Phys Med Biol, 44(8), N183-N192. doi: 10.1088/0031-9155/44/8/402

Beekman, F. J., *et al.* **2005.** *U-SPECT-I: a novel system for submillimeter-resolution tomography with radiolabeled molecules in mice.* J Nucl Med, 46(7), 1194-1200.

Beekman, F., & van der Have, F. **2007.** *The pinhole: gateway to ultra-high-resolution three-dimensional radionuclide imaging.* Eur J Nucl Med Mol Img, 34(2), 151-161. doi: 10.1007/s00259-006-0248-6

Bert, J., *et al.* **2013.** *Geant4-based Monte Carlo simulations on GPU for medical applications.* Phys Med Biol, 58(16), 5593-5611. doi: 10.1088/0031-9155/58/16/5593

Bochud, F. O., *et al.* **1999.** *Estimation of the noisy component of anatomical backgrounds.* Med Phys, 26(7), 1365-1370. doi: 10.1118/1.598632

Branderhorst, W., *et al.* **2011.** *Targeted multi-pinhole SPECT.* Eur J Nucl Med Mol Img, 38(3), 552-561. doi: 10.1007/s00259-010-1637-4

Branderhorst, W., *et al.* **2014.** *Three-Dimensional Histologic Validation of High-Resolution SPECT of Antibody Distributions Within Xenografts.* J Nucl Med, 55(5), 830-837. doi: 10.2967/jnumed.113.125401

Brem, R. F., *et al.* **2008.** *Breast-specific Gamma Imaging as an Adjunct Imaging Modality for the Diagnosis of Breast Cancer.* Radiology, 247(3), 651-657. doi: doi:10.1148/radiol.2473061678

Brunner, F. C., *et al.* **2009.** *Simulation of PIXSCAN, a photon counting micro-CT for small animal imaging.* Journal of Instrumentation, 4. doi: Artn P05012 10.1088/1748-0221/4/05/P05012

Brzymialkiewicz, C. N., *et al.* **2005.** *Evaluation of fully 3-D emission mammotomography with a compact cadmium zinc telluride detector.* IEEE Trans Med Imag, 24(7), 868-877. doi: 10.1109/Tmi.2005.852501

Burgess, A. E. **1999a**. *Mammographic structure: data preparation and spatial statistics analysis.* Proc. SPIE 3661, 642, doi: 10.1117/12.348620

Burgess, A. E. **1999b**. *Visual signal detection with two-component noise: low-pass spectrum effects.* J Opt Soc Am A, 16(3), 694-704. doi: 10.1364/JOSAA.16.000694

Burgess, A. E., *et al.* **2001**. *Human observer detection experiments with mammograms and power-law noise.* Med Phys, 28(4), 419-437. doi: 10.1118/1.1355308

Campbell, D. L., & Peterson, T. E. **2014**. *Simulation study comparing high-purity germanium and cadmium zinc telluride detectors for breast imaging.* Phys Med Biol, 59(22), 7059-7079. doi: 10.1088/0031-9155/59/22/7059

Carney, P. A., *et al.* **2003**. *Individual and Combined Effects of Age, Breast Density, and Hormone Replacement Therapy Use on the Accuracy of Screening Mammography.* Annals of Internal Medicine, 138(3), 168-175. doi: 10.7326/0003-4819-138-3-200302040-00008

Capote, R. M., *et al.* **2013**. *Optimization of convergent collimators for pixelated SPECT systems.* Med Phys, 40(6), 062501. doi: 10.1118/1.4804053

Chen, Y., *et al.* **2009**. *Characterization of scatter in cone-beam CT breast imaging: Comparison of experimental measurements and Monte Carlo simulation.* Med Phys, 36(3), 857-869. doi: 10.1118/1.3077122

Cherry, S. R., *et al.* **2003**. *Physics in Nuclear Medicine.* Saunders, Philadelphia, PA, USA, 3rd edition.

Coover, L. R., *et al.* **2004**. *Scintimammography with dedicated breast camera detects and localizes occult carcinoma.* J Nucl Med, 45(4), 553-558.

Cot, A., *et al.* **2002**. *Evaluation of the geometric, scatter, and septal penetration components in fan-beam collimators using Monte Carlo simulation.* IEEE Trans Nucl Sci, 49(1), 12-16. doi: 10.1109/Tns.2002.998674

Cot, A., *et al.* **2004**. *Study of the point spread function (PSF) for I-123 SPECT imaging using Monte Carlo simulation.* Phys Med Biol, 49(14), 3125-3136. doi: 10.1088/0031-9155/49/14/007

Crotty, D. J., *et al.* **2008**. *Improved chest wall imaging through combined complex trajectories in dedicated dual modality SPECT-CT breast molecular imaging.* Paper presented at the Nuclear Science Symposium Conference Record, 2008.

Currie, L. A. **1968**. *Limits for qualitative detection and quantitative determination. Application to radiochemistry.* Analytical Chemistry, 40(3), 586-593. doi: 10.1021/ac60259a007

Daekwang, K., & Metzler, S. D. **2012**. *Finding Optimized Conditions of Slit-Slat and Multislit-Slat Collimation for Breast Imaging.* IEEE Trans Nucl Sci, 59(1), 62-69. doi: 10.1109/TNS.2011.2177912

de Beenhouwer, J., *et al.* **2007**. *Cluster computing software for GATE simulations.* Med Phys, 34(6), 1926-1933. doi: 10.1118/1.2731993

de Jong, H. W. A. M., *et al.* **2001**. *Acceleration of Monte Carlo SPECT simulation using convolution-based forced detection.* IEEE Trans Nucl Sci, 48(1), 58-64. doi: 10.1109/23.910833

Descourt, P., *et al.* **2010**. *Implementation of angular response function modeling in SPECT simulations with GATE.* Phys Med Biol, 55(9), N253-N266. doi: 10.1088/0031-9155/55/9/N04

Devries, D. J., *et al.* **1990**. <u>*Development and Validation of a Monte-Carlo Simulation of Photon Transport in an Anger Camera.*</u> IEEE Trans Med Imag, 9(4), 430-438. doi: 10.1109/42.61758

Dickerscheid, D., *et al.* **2013**. *Contrast-noise-ratio (CNR) analysis and optimisation of breast-specific gamma imaging (BSGI) acquisition protocols.* EJNMMI research, 3(1), 1-9. doi: 10.1186/2191-219X-3-21

Dong, S.-L., *et al.* **2011**. *Development of an Adjustable Model Breast for Mammographic Dosimetry Assessment in Taiwanese Women.* Am J of Roentgenology, 196(4), W476-W481.

Drukteinis, J. S., *et al.* **2013**. *Beyond Mammography: New Frontiers in Breast Cancer Screening.* The American Journal of Medicine, 126(6), 472-479. doi:10.1016/j.amjmed.2012.11.025

El Bitar, Z., *et al.* **2011**. *Acceleration of Fully 3D Monte Carlo Based System Matrix Computation for Image Reconstruction in Small Animal SPECT.* IEEE Trans Nucl Sci, 58(1), 121-132. doi: 10.1109/Tns.2010.2096292

Feng, B., *et al.* **2010**. *Modeling of the Point Spread Function by Numerical Calculations in Single-Pinhole and Multipinhole SPECT Reconstruction.* IEEE Trans Nucl Sci, 57(1), 173-180. doi: 10.1109/Tns.2009.2034656

Ferlay, J., *et al.* **2015**. *Cancer incidence and mortality worldwide: Sources, methods and major patterns in GLOBOCAN 2012.* Int J of Cancer, 136(5), E359-E386. doi: 10.1002/ijc.29210

Formiconi, A. R. **1998**. *Geometrical response of multihole collimators.* Phys Med Biol, 43(11):3359–79.

Formiconi, A. R., *et al.* **2004** *Optimization of high energy collimator design.* Paper presented at the Nuclear Science Symposium Conference Record

Fowler, A. M. **2014**. *A Molecular Approach to Breast Imaging.* J Nucl Med, 55(2), 177-180. doi: 10.2967/jnumed.113.126102

Funk, T., *et al.* **2006**. *Simulation and validation of point spread functions in pinhole SPECT imaging.* IEEE Trans Nucl Sci, 53(5), 2729-2735. doi: 10.1109/Tns.2006.878009

Garcia, M.-P., *et al.* **2016**. *Accelerated GPU based SPECT Monte Carlo simulations.* Phys Med Biol, 61(11), 4001.

Gieles, M., *et al.* **2002**. *Monte Carlo simulations of pinhole imaging accelerated by kernel-based forced detection.* Phys Med Biol, 47(11), 1853-1867. doi: 10.1088/0031-9155/47/11/302

Glassner, A. S. **1984**. *Space Subdivision for Fast Ray Tracing.* IEEE Comp. Graph Appl, 4(10), 15-22.

Goertzen, A. L., *et al.* **2002**. *Effect of phantom voxelization in CT simulations.* Med Phys, 29(4), 492-498. doi: 10.1118/1.1461841

Gong, Z. Y., & Williams, M. B. **2015**. *Comparison of breast specific gamma imaging and molecular breast tomosynthesis in breast cancer detection: Evaluation in phantoms.* Med Phys, 42(7), 4250-4259. doi: 10.1118/1.4922398

Goorden, M. C., & Beekman, F. J. **2010**. *High-resolution tomography of positron emitters with clustered pinhole SPECT.* Phys Med Biol, 55(5), 1265-1277. doi: 10.1088/0031-9155/55/5/001

Goorden, M. C., *et al.* **2008**. *Theoretical analysis of multi-pinhole brain spect.* In IEEE Nuclear Science Symposium Conference Record, pages 4036–4038.

Goorden, M. C., *et al.* **2011**. *An efficient simulator for pinhole imaging of PET isotopes.* Phys Med Biol, 56(6), 1617-1634. doi: 10.1088/0031-9155/56/6/007

Goorden, M. C., *et al.* **2016**. *Optimizing modelling in iterative image reconstruction for preclinical pinhole PET.* Phys Med Biol, 61(10), 3712-3733. doi: 10.1088/0031-9155/61/10/3712

Gopan, O., *et al.* **2014**. *Molecular Imaging of the Breast Using a Variable-Angle Slant-Hole Collimator.* IEEE Trans Nucl Sci, 61(3), 1143-1152. doi: 10.1109/TNS.2014.2322520

Gradshteyn, I. and Ryzhik, I. **2014**. *Table of Integrals, Series, and Products.* Elsevier Science.

Grevillot, L., *et al.* **2011**. *Simulation of a 6 MV Elekta Precise Linac photon beam using GATE/GEANT4.* Phys Med Biol, 56(4), 903-918. doi: 10.1088/0031-9155/56/4/002

Gruber, G. J., *et al.* **1999**. *Monte Carlo simulation of breast tumor imaging properties with compact, discrete gamma cameras.* IEEE Trans Nucl Sci, 46(6), 2119-2123. doi: Doi 10.1109/23.819292

Gullberg, G. T., *et al.* **1991a**. *Cone beam tomography of the heart using single-photon emission-computed tomography.* Investigative Radiology, 26(7):681–688.

Gullberg, G. T., *et al.* **1991b**. *Single photon emission computed tomography of the heart using cone beam geometry and noncircular detector rotation.* Progress in clinical and biological research, 363:123–138.

Gunter, D. L. **1996**. *Collimator characteristics and design.* Nuclear Medicine, 1, 96-124.

Gunter, D. L. **2004**. *Collimator design for nuclear medicine.* In Wernick, M. N. and Aarsvold, J. N., editors, *Emission tomography: the fundamentals of PET and SPECT.*, pages 153–68. Elsevier Academic

Hammond, R. L., *et al.* **2015**. *Reflection on the Oslo Tomosynthesis Screening Trial*. In P. Hogg, J. Kelly, & C. Mercer (Eds.), *Digital Mammography: A Holistic Approach* (pp. 247-250). Cham: Springer International Publishing.

Harris, C. H. **2010**. *New imaging tools address challenges of dense breast tissue*. AuntMinnie.com special report: *advances in MBI*. http://www.auntminnie.com/index.aspx?sec=spt&sub=mbi

Hashimoto, J., *et al.* **1997**. *Scatter and attenuation correction in technetium-99m brain SPECT.* J Nucl Med, 38(1), 157-162.

Hawman, P. C. and Haines, E. J. **1994**. *The cardiofocal collimator: a variable-focus collimator for cardiac spect.* Phys Med Biol, 39(3):439.

Haynor, D. R., *et al.* **1990**. *Improving the Efficiency of Emission Tomography Simulations Using Variance Reduction Techniques*. IEEE Trans Nucl Sci, 37(2), 749-753. doi: 10.1109/23.106709

Helvie, M. A., *et al.* **1994**. *Breast thickness in routine mammograms: effect on image quality and radiation dose.* Am J Roentgenology, 163(6), 1371-1374. doi: 10.2214/ajr.163.6.7992731

Hesterman, J. Y., *et al.* **2010**. *Maximum-Likelihood Estimation With a Contracting-Grid Search Algorithm*. IEEE Trans Nucl Sci, 57(3), 1077-1084. doi: 10.1109/TNS.2010.2045898

Hruska, C. B. **2016**. *Molecular Breast Imaging for Screening in Dense Breasts: State of the Art and Future Directions*. Am J Roentgenology, 208(2), 275-283. doi: 10.2214/AJR.16.17131

Hruska, C. B., *et al.* **2008**. *Molecular Breast Imaging: Use of a Dual-Head Dedicated Gamma Camera to Detect Small Breast Tumors*. Am J Roentgenology, 191(6), 1805-1815. doi: 10.2214/Ajr.07.3693

Hruska, C. B., *et al.* **2012a**. *Proof of concept for low-dose molecular breast imaging with a dual-head CZT gamma camera. Part I. Evaluation in phantoms.* Med Phys, 39(6), 3466-3475. doi: 10.1118/1.4718665

Hruska, C. B., *et al.*. **2012b**. *Proof of concept for low-dose molecular breast imaging with a dual-head CZT gamma camera. Part II. Evaluation in patients.* Med Phys, 39(6), 3476-3483. doi: 10.1118/1.4719959

Hruska, C. B., & O'Connor, M. K. **2006**. *CZT detectors: How important is energy resolution for nuclear breast imaging?* Physica Medica, 21, 72-75. doi: 10.1016/s1120-1797(06)80029-3

Hruska, C. B., & O'Connor, M. K. **2008a**. *A Monte Carlo Model for Energy Spectra Analysis in Dedicated Nuclear Breast Imaging*. IEEE Trans Nucl Sci, 55(1), 491-500. doi: 10.1109/TNS.2007.910882

Hruska, C. B., & O'Connor, M. K. **2008b**. *Quantification of lesion size, depth, and uptake using a dual-head molecular breast imaging system.* Med Phys, 35(4), 1365-1376. doi: 10.1118/1.2885371

Hruska, C. B., & O'Connor, M. K. **2013**. *Nuclear imaging of the breast: Translating achievements in instrumentation into clinical use.* Med Phys, 40(5), 050901. doi: 10.1118/1.4802733

Hubert-Tremblay, V., *et al.* **2006**. *Octree indexing of DICOM images for voxel number reduction and improvement of Monte Carlo simulation computing efficiency.* Med Phys, 33(8), 2819-2831. doi: 10.1118/1.2214305

Hunter, W. C. J., *et al.* **2013**. *SCOUT: a fast Monte-Carlo modeling tool of scintillation camera output.* Phys Med Biol, 58(11), 3581-3598. doi: 10.1088/0031-9155/58/11/3581

Hutton, B. F., *et al.* **2011**. *Review and current status of SPECT scatter correction.* Phys Med Biol, 56(14), R85-R112. doi: 10.1088/0031-9155/56/14/R01

Ichihara, T., *et al.* **1993**. *Compton Scatter Compensation Using the Triple-Energy Window Method for Single-Isotope and Dual-Isotope Spect.* J Nucl Med, 34(12), 2216-2221.

Ivashchenko, O., *et al.* **2014**. *Quarter-Millimeter-Resolution Molecular Mouse Imaging with U-SPECT.* Molecular Imaging, 13, 1-8. doi: 10.2310/7290.2014.00053

Ivashchenko, O., *et al.* **2015**. *Ultra-High-Sensitivity Submillimeter Mouse SPECT.* J Nucl Med, 56(3), 470-475. doi: 10.2967/jnumed.114.147140

Jan, S., *et al.* **2004**. *GATE: a simulation toolkit for PET and SPECT.* Phys Med Biol, 49(19), 4543. doi: 10.1088/0031-9155/49/19/007

Jan, S., *et al.* **2011**. *GATE V6: a major enhancement of the GATE simulation platform enabling modelling of CT and radiotherapy.* Phys Med Biol, 56(4), 881. doi: 10.1088/0031-9155/56/4/001

Jaszczak, R. J., *et al.* **1979**. *Single photon emission computed tomography using multi-slice fan beam collimators.* IEEE Trans Nucl Sci, 26(1):610–618.

Jaszczak, R. J., *et al.* **1986**. *Cone beam collimation for single photon-emission computed-tomography -analysis, simulation, and image-reconstruction using filtered backprojection.* Med Phys, 13(4):484–489.

Jaszczak, R. J., *et al.* **1988**. *Spect using a specially designed cone beam collimator.* J Nucl Med, 29(8):1398–1405.

Judy, P. G., *et al.* **2010**. *Analysis of Image Combination Methods for Conjugate Breast Scintigraphy.* IEEE Trans Nucl Sci, 57(3), 1146-1154. doi: 10.1109/TNS.2009.2038472

Kalles, V., *et al.* **2013**. *The current status of positron emission mammography in breast cancer diagnosis.* Breast Cancer, 20(2), 123-130. doi:10.1007/s12282-012-0433-3

Kamphuis, C. and Beekman, F. J. **1998**. *The use of offset cone-beam collimators in a dual head system for combined emission transmission brain spect: a feasibility study.* IEEE Trans Nucl Sci, 45(3):1250–1254.

Keidar, Z., *et al.* **2016**. *Novel Cadmium Zinc Telluride Based detector General Purpose Gamma Camera: Initial Evaluation and Comparison with a Standard Camera.* J Nucl Med, 57(supplement 2), 259.

Kemp, B. J., *et al.* **1995**. *Transmission computed tomography imaging of the head with a spect system and a collimated line source.* J Nucl Med, 36(2):328–335.

Kijewski, M. F., *et al.***1997**. *Nonuniform collimator sensitivity: Improved precision for quantitative spect.* J Nucl Med, 38(1):151–156.

Kolb, T. M., *et al.* **2002**. *Comparison of the Performance of Screening Mammography, Physical Examination, and Breast US and Evaluation of Factors that Influence Them: An Analysis of 27,825 Patient Evaluations.* Radiology, 225(1), 165-175. doi: 10.1148/radiol.2251011667

Kowalsky, R. J., & Falen, S. W. **2011**. *Radiopharmaceuticals in Nuclear Pharmacy and Nuclear Medicine*: American Pharmacists Association.

Lamare, F., *et al.* **2006**. *Validation of a Monte Carlo simulation of the Philips Allegro/GEMINI PET systems using GATE.* Phys Med Biol, 51(4), 943-962. doi: 10.1088/0031-9155/51/4/013

Lång, K., *et al.* **2015**. *Performance of one-view breast tomosynthesis as a stand-alone breast cancer screening modality: results from the Malmö Breast Tomosynthesis Screening Trial, a population-based study.* European Radiology, 1-7. doi: 10.1007/s00330-015-3803-3

Lange, K., & Carson, R. **1984**. *EM reconstruction algorithms for emission and transmission tomography.* J Comput Assist Tomogr, 8(2), 306-316.

Lee, C. H., *et al.* **2010**. *Breast Cancer Screening With Imaging: Recommendations From the Society of Breast Imaging and the ACR on the Use of Mammography, Breast MRI, Breast Ultrasound, and Other Technologies for the Detection of Clinically Occult Breast Cancer.* J Am Col of Radiology, 7(1), 18-27. doi: 10.1016/j.jacr.2009.09.022

Lee, T., *et al.* **2004**. *The effects of lead shielding of background organ activity in pinhole Single Photon Emission Computed Tomography (SPECT) breast tumor imaging.* Paper presented at the Nuclear Science Symposium Conference Record.

Li, C. *et al.* **2009**. *Methodology for generating a 3D computerized breast phantom from empirical data.* Med Phys, 36(7), 3122-3131. doi: 10.1118/1.3140588

Li, J., *et al.* **1996**. *Half-cone beam collimation for triple-camera spect systems.* J Nucl Med, 37(3):498–502.

Li, X., & Furenlid, L. R. **2014**. *A SPECT system simulator built on the Solid Works (TM) 3D-Design package.* Paper presented at the Medical Applications of Radiation Detectors Iv.

Lippuner, J., & Elbakri, I. A. **2011**. *A GPU implementation of EGSnrc's Monte Carlo photon transport for imaging applications.* Phys Med Biol, 56(22), 7145-7162. doi: 10.1088/0031-9155/56/22/010

Ljungberg, M., *et al.* **2005**. *A new collimator simulation in SIMIND based on the delta-scattering technique.* IEEE Trans Nucl Sci, 52(5), 1370-1375. doi: 10.1109/Tns.2005.858252

Long, Z., *et al.* **2016**. *Performance characteristics of dedicated molecular breast imaging systems at low doses.* Med Phys, 43(6), 3062-3070.

Lowe, D., *et al.* **2002**. *Optimisation of the design of round-hole parallel collimators for ultra-compact nuclear medicine imaging.* Nuclear Instruments and Methods in Physics Research Section A: Accelerators, Spectrometers, Detectors and Associated Equipment, 488(12):428 – 440.

Luo, W., *et al.* **2010**. *Performance Evaluation of a PEM Scanner Using the NEMA NU 4–2008 Small Animal PET Standards.* IEEE Trans Nucl Sci, 57(1), 94-103. doi: 10.1109/TNS.2009.2036847

MacDonald, L., *et al.* **2009**. *Clinical Imaging Characteristics of the Positron Emission Mammography Camera: PEM Flex Solo II.* J Nucl Med, 50(10), 1666-1675. doi: 10.2967/jnumed.109.064345

Madhav, P., *et al.* **2006**. *Initial Development of a Dual-Modality SPECT-CT System for Dedicated Mammotomography.* Paper presented at the Nuclear Science Symposium Conference Record.

Mallard, J. R., & Myers, M. J. **1963**. *The Performance of a Gamma Camera for the Visualization of Radioactive Isotopes in vivo.* Phys Med Biol, 8(2), 165.

Manglos, S. H., *et al.* **1992**. *Imaging of the human torso using cone-beam transmission ct implemented on a rotating gamma camera.* J Nucl Med, 33(1):150–156.

Mankoff, D. A., *et al.* **2002**. *[Tc-99m]-sestamibi uptake and washout in locally advanced breast cancer are correlated with tumor blood flow.* Nuclear Medicine and Biology, 29(7), 719-727. doi: 10.1016/S0969-8051(02)00333-5

Mankoff, D. A., *et al.* **2007**. *Molecular Imaging Research in the Outcomes Era: Measuring Outcomes for Individualized Cancer Therapy.* Academic Radiology, 14(4), 398-405. doi: 10.1016/j.acra.2007.01.005

Mann, S. D., *et al.* **2012**. *Initial In Vivo Quantification of Tc-99m Sestamibi Uptake as a Function of Tissue Type in Healthy Breasts Using Dedicated Breast SPECT-CT.* Journal of Oncology. doi: 10.1155/2012/146943

Matej, S., & Lewitt, R. M. **1996**. *Practical considerations for 3-D image reconstruction using spherically symmetric volume elements.* IEEE Trans Med Imag, 15(1), 68-78. doi: 10.1109/42.481442

Mather, R. L. **1957**. *Gamma-ray collimator penetration and scattering effects.* Journal of Applied Physics, 28(10):1200–1207.

Maublant, J., *et al.* **1996**. *Technetium-99m-sestamibi uptake in breast tumor and associated lymph nodes.* J Nucl Med, 37(6), 922-925.

Meagher, D. **1982**. *Geometric Modeling Using Octree Encoding.* Computer Graphics and Image Processing, 19(2), 129-147. doi: 10.1016/0146-664x(82)90104-6

Menezes, G. L. G., *et al.* **2014**. *Magnetic resonance imaging in breast cancer: A literature review and future perspectives.* World Journal of Clinical Oncology, 5(2), 61-70. doi:10.5306/wjco.v5.i2.61

Metheany, K. G., *et al.* **2008**. *Characterizing anatomical variability in breast CT images.* Med Phys, 35(10), 4685-4694. doi: 10.1118/1.2977772

Metz, C. E., *et al.* **1980**. *The geometric transfer function component for scintillation camera collimators with straight parallel holes.* Phys Med Biol, 25(6):1059.

Metzler, S. D., *et al.* **2001**. *Analytic determination of pinhole collimator sensitivity with penetration.* IEEE Trans Med Imaging, 20(8), 730-741. doi: 10.1109/42.938241

Metzler, S. D., *et al.* **2006**. *On-Axis Sensitivity and Resolution of a Slit-Slat Collimator.* J Nucl Med, 47(11), 1884-1890.

Milster, T. D., *et al.* **1985**. *Digital Position Estimation for the Modular Scintillation Camera.* IEEE Trans Nucl Sci, 32(1), 748-752. doi: 10.1109/TNS.1985.4336935

Milster, T. D., *et al.* **1990**. *A Full-Field Modular Gamma Camera.* J Nucl Med, 31(5), 632-639.

Mitchell, D., *et al.* **2013**. *99mTc-Sestamibi Using a Direct Conversion Molecular Breast Imaging System to Assess Tumor Response to Neoadjuvant Chemotherapy in Women With Locally Advanced Breast Cancer.* Clinical nuclear medicine, 38(12), 949-956.

Miyake, K. K., *et al.* **2014**. *Performance Evaluation of a New Dedicated Breast PET Scanner Using NEMA NU4-2008 Standards.* J Nucl Med. doi: 10.2967/jnumed.113.131565

Miyake, K. K., *et al.* **2016**. *Current Status of Dedicated Breast PET Imaging.* Current Radiology Reports, 4(4), 16. doi:10.1007/s40134-016-0145-0

Miyake, K. K., & Nakamoto, Y. **2017**. *Clinical Evaluation of Focused High-Resolution Breast PET.* In T. Inoue, D. Yang, & G. Huang (Eds.), P*ersonalized Pathway-Activated Systems Imaging in Oncology: Principal and Instrumentation* (pp. 171-184). Singapore: Springer Singapore.

Mok, G. S. P., *et al.* **2009**. *Quantification of the Multiplexing Effects in Multi-Pinhole Small Animal SPECT: A Simulation Study.* IEEE Trans Nucl Sci, 56(5), 2636-2643. doi: 10.1109/TNS.2009.2023444

Moliner, L., *et al.* **2012**. *Design and evaluation of the MAMMI dedicated breast PET.* Med Phys, 39(9), 5393-5404. doi: 10.1118/1.4742850

Moore, S. K., *et al.* **2007**. *Maximum-likelihood estimation of 3D event position in monolithic scintillation crystals: Experimental results.* Paper presented at the Nuclear Science Symposium Conference Record.

Moore, S. C., *et al.* **1992**. *Collimator design for single photon emission tomography.* European J Nucl Med, 19(2), 138-150. doi: 10.1007/bf00184130

Moyer, R. A. **1974**. *A low-energy multihole converging collimator compared with a pinhole collimator.* J Nucl Med, 15(2):59–64.

Mueller, B., *et al.* **2003**. *Evaluation of a small cadmium zinc telluride detector for scintimammography.* J Nucl Med, 44(4), 602-609.

Nyström, L., *et al.* **2002**. *Long-term effects of mammography screening: updated overview of the Swedish randomised trials.* The Lancet, 359**9310**, 909-919. doi: 10.1016/S0140-6736(02)08020-0

O'Connor, M. K., *et al.* **2007**. *Molecular Breast Imaging: Advantages and Limitations of a Scintimammographic Technique in Patients with Small Breast Tumors.* The Breast Journal, 13(1), 3-11. doi: 10.1111/j.1524-4741.2006.00356.x

O'Connor, M.K., *et al.* **2008**. *Molecular breast imaging (MBI) as an adjunct to screening mammography.* J Nucl Med, 49(Supplement 1), 40P.

O'Connor, M.K., *et al.* **2009**. *Molecular breast imaging.* Expert Rev Anticancer Ther, 9(8), 1073-1080. doi:10.1586/era.09.75

Ogawa, K., *et al.* **1991**. *A Practical Method for Position-Dependent Compton-Scatter Correction in Single Photon-Emission CT.* IEEE Trans Med Imag, 10(3), 408-412. doi: 10.1109/42.97591

Ogawa, K., & Maeda, S. **1995**. *A Monte Carlo method using octree structure in photon and electron transport.* IEEE Trans Nucl Sci, 42(6), 2322-2326. doi: 10.1109/23.489435

Orlov, S. **1975**. *Theory of three dimensional reconstruction: I. Conditions for a complete set of projections.* Kristallografiya, 20, 312-314.

Otto, S. J., *et al.***2003**. *Initiation of population-based mammography screening in Dutch municipalities and effect on breast-cancer mortality: a systematic review.* The Lancet, 361**9367**, 1411-1417. doi: 10.1016/S0140-6736(03)13132-7

Paix, D. **1967**. *Pinhole imaging of gamma rays.* Phys Med Biol, 12(4), 489.

Pani, R., *et al.* **1998**. *Dedicated Gamma Camera for Single Photon Emission Mammography (SPEM).* IEEE Trans Nucl Sci, 45(6), 3127-3133. doi: 10.1109/23.737675

Park, M.-A., *et al.* **2003**. *Evaluation of ultra- short focusing cone-beam collimators for spect brain imaging.* In Nuclear Science Symposium Conference Record, volume 3, pages 1865–1867 Vol.3.

Park, M.-A., *et al.* **2005**. *Brain spect with short focal-length cone-beam collimation.* Med Phys, 32(7):2236–2244.

Pato, L. R. V., *et al.* **2015**. *Parallel-hole collimator concept for stationary spect imaging.* Phys Med Biol, 60(22):8791.

Perez, K. L., *et al.* **2010**. *Characterizing the contribution of cardiac and hepatic uptake in dedicated breast SPECT using tilted trajectories.* Phys Med Biol, 55(16), 4721. doi: 10.1088/0031-9155/55/16/007

Perez, K. L., *et al.* **2011**. *Towards Quantification of Functional Breast Images Using Dedicated SPECT With Non-Traditional Acquisition Trajectories.* IEEE Trans Nucl Sci, 58(5), 2219-2225. doi: 10.1109/TNS.2011.2165223

Peterson, T. E., & Furenlid, L. R. **2011**. *SPECT detectors: the Anger Camera and beyond.* Phys Med Biol, 56(17), R145. doi: 10.1088/0031-9155/56/17/R01

Peterson, T. E., & Shokouhi, S. **2012**. *Advances in Preclinical SPECT Instrumentation.* J Nucl Med, 53(6), 841-844. doi: 10.2967/jnumed.111.099853

Pisano, E. D., *et al.* **2008**. *Diagnostic Accuracy of Digital versus Film Mammography: Exploratory Analysis of Selected Population Subgroups in DMIST.* Radiology, 246(2), 376-383. doi: 10.1148/radiol.2461070200

Plana, M. N., *et al.* **2012**. *Magnetic resonance imaging in the preoperative assessment of patients with primary breast cancer: systematic review of diagnostic accuracy and meta-analysis.* European Radiology, 22(1), 26-38. doi: 10.1007/s00330-011-2238-8

Qi, J., & Leahy, R. M. **2006**. *Iterative reconstruction techniques in emission computed tomography.* Phys Med Biol, 51(15), R541. doi: 10.1088/0031-9155/51/15/R01

Raylman, R. R., *et al.* **2008**. *The positron emission mammography/tomography breast imaging and biopsy system (PEM/PET): design, construction and phantom-based measurements.* Phys Med Biol, 53(3), 637-653. doi: 10.1088/0031-9155/53/3/009

Raymond, R. R., *et al.* **2008**. *The positron emission mammography/tomography breast imaging and biopsy system (PEM/PET): design, construction and phantom-based measurements.* Phys Med Biol, 53(3), 637.

Rehfeld, N. S., *et al.* **2009**. *Introducing improved voxel navigation and fictitious interaction tracking in GATE for enhanced efficiency.* Phys Med Biol, 54(7), 2163-2178. doi: 10.1088/0031-9155/54/7/021

Rentmeester, M. C., *et al.* **2007**. *Optimizing multi-pinhole spect geometries using an analytical model.* Phys Med Biol, 52(9):2567–81.

Rhodes, D. J., *et al.* **2005**. *Molecular Breast Imaging: A New Technique Using Technetium Tc 99m Scintimammography to Detect Small Tumors of the Breast.* Mayo Clinic Proceedings, 80(1), 24-30. doi: 10.4065/80.1.24

Rhodes, D. J., *et al.* **2015**. *JOURNAL CLUB: Molecular Breast Imaging at Reduced Radiation Dose for Supplemental Screening in Mammographically Dense Breasts.* Am J Roentgenology, 204(2), 241-251. doi: 10.2214/AJR.14.13357

Rogers, D. W. O. **2006**. *Fifty years of Monte Carlo simulations for Medical Physics.* Phys Med Biol, 51(13), R287-R301. doi: 10.1088/0031-9155/51/13/R17

Rose, A. **1973**. *Vision: human and electronic*: Plenum Press, New York.

Rozler, M., *et al.* **2012**. *Development of a cost-effective modular pixelated NaI(Tl) detector for clinical SPECT applications.* IEEE Trans Nucl Sci, 59(5), 1831-1840. doi: 10.1109/TNS.2012.2210908

Salvador, S., *et al.* **2012**. *Improved EMCCD gamma camera performance by SiPM pre-localization.* Phys Med Biol, 57(22), 7709. doi: 10.1088/0031-9155/57/22/7709

Sarrut, D., & Guigues, L. **2008**. *Region-oriented CT image representation for reducing computing time of Monte Carlo simulations.* Med Phys, 35(4), 1452-1463. doi: 10.1118/1.2884854

Schmidtlein, C. R., *et al.* **2006**. *Validation of GATE Monte Carlo simulations of the GE Advance/Discovery LS PET scanners.* Med Phys, 33(1), 198-208. doi: 10.1118/1.2089447

Schneble, E. J., *et al.* **2014**. *Future Directions for the Early Detection of Recurrent Breast Cancer.* Journal of Cancer, 5(4), 291-300. doi:10.7150/jca.8017

Schramm, N. U., *et al.* **2003**. *High-resolution SPECT using multipinhole collimation.* IEEE Trans Nucl Sci, 50(3), 315-320. doi: 10.1109/Tns.2003.812437

Scopinaro, F., *et al.* **1999**. *High-resolution scintimammography improves the accuracy of technetium-99m methoxyisobutylisonitrile scintimammography: use of a new dedicated gamma camera.* European J Nucl Med, 26(10), 1279-1288. doi: 10.1007/s002590050584

Sechopoulos, I. **2013**. *A review of breast tomosynthesis. Part I. The image acquisition process.* Med Phys, 40(1), -. doi: 10.1118/1.4770279

Segars, W. P., *et al.* **2010**. *4D XCAT phantom for multimodality imaging research.* Med Phys, 37(9), 4902-4915. doi: 10.1118/1.3480985

Segars, W. P., & Tsui, B. M. W. **2009**. *MCAT to XCAT: The Evolution of 4-D Computerized Phantoms for Imaging Research.* Proceedings of the IEEE, 97(12), 1954-1968. doi: 10.1109/JPROC.2009.2022417

Shah, J. P., *et al.* **2014**. *Design of a nested SPECT-CT system with fully suspended CT sub-system for dedicated breast imaging.* Proc. SPIE 9033, doi: 10.1117/12.2043739

Shepp, L. A., & Vardi, Y. **1982**. *Maximum Likelihood Reconstruction for Emission Tomography.* IEEE Trans Med Imag, 1(2), 113-122. doi: 10.1109/TMI.1982.4307558

Shermis, R. B., *et al.* **2016**. *Supplemental Breast Cancer Screening With Molecular Breast Imaging for Women With Dense Breast Tissue.* Am J Roentgenology, 207(2), 450-457. doi: 10.2214/AJR.15.15924

Shultis, J. K., & Faw, R. E. **2016**. *Fundamentals of Nuclear Science and Engineering* (Third Edition ed.): CRC press.

Siddon, R. L. **1985**. *Fast calculation of the exact radiological path for a three-dimensional ct array.* Med Phys, 12(2):252–255.

Siman, W., & Kappadath, S. C. **2012**. *Performance characteristics of a new pixelated portable gamma camera.* Med Phys, 39(6), 3435-3444. doi: 10.1118/1.4718874

Skaane, P., *et al.* **2013**. *Comparison of Digital Mammography Alone and Digital Mammography Plus Tomosynthesis in a Population-based Screening Program.* Radiology, 267(1), 47-56. doi: 10.1148/radiol.12121373

Skaane, P., *et al.* **2014**. *Two-View Digital Breast Tomosynthesis Screening with Synthetically Reconstructed Projection Images: Comparison with Digital Breast Tomosynthesis with Full-Field Digital Mammographic Images.* Radiology, 271(3), 655-663. doi:10.1148/radiol.13131391

Smith, M. F., *et al.* **1997**. *Lead and tungsten pinhole inserts for I-131 SPECT tumor imaging: Experimental measurements and photon transport simulations.* IEEE Trans Nucl Sci, 44(1), 74-82. doi: Doi 10.1109/23.554828

Staelens, S., *et al.* **2006**. *GATE simulations for optimization of pinhole imaging.* Nuclear Instruments & Methods in Physics Research Section a-Accelerators Spectrometers Detectors and Associated Equipment, 569(2), 359-363. doi: 10.1016/j.nima.2006.08.071

Suganuma, R., & Ogawa, K. **2000**. *Effective description of a 3D object for photon transportation in Monte Carlo simulation.* IEEE Trans Nucl Sci, 47(3), 1024-1029. doi: 10.1109/23.856542

Sullivan, D. C., *et al.* **1991**. *Measurement of force applied during mammography.* Radiology, 181(2), 355-357. doi: 10.1148/radiology.181.2.1924771

Sullivan, O., *et al.* **2012**. *The Impact of Reduced Injected Radioactivity on Image Quality of Molecular Breast Imaging Tomosynthesis.* In A. A. Maidment, P. Bakic & S. Gavenonis (Eds.), *Breast Imaging* (Vol. 7361, pp. 300-307): Springer Berlin Heidelberg.

Sun, Y., *et al.* **2013**. *Clinical usefulness of breast-specific gamma imaging as an adjunct modality to mammography for diagnosis of breast cancer: a systemic review and meta-analysis.* Eur J Nucl Med Mol Img, 40(3), 450-463. doi: 10.1007/s00259-012-2279-5

Tabary, J., *et al.* **2004**. *Combination of high resolution analytically computed uncollided flux images with low resolution Monte Carlo computed scattered flux images.* IEEE Trans Nucl Sci, 51(1), 212-217. doi: 10.1109/Tns.2003.823038

Ter-Antonyan, R., *et al.* **2009**. *Combination of converging collimators for high-sensitivity brain spect.* J Nucl Med, 50(9):1548–1556.

Tornai, M. P., *et al.* **2003**. *Mammotomography with pinhole incomplete circular orbit SPECT.* J Nucl Med, 44(4), 583-593.

Torre, L. A., *et al.* **2015**. *Global cancer statistics, 2012.* CA: A Cancer Journal for Clinicians, 65(2), 87-108. doi: 10.3322/caac.21262

Tsui, B. M., *et al.* **1986**. *Design and clinical utility of a fan beam collimator for spect imaging of the head.* J Nucl Med, 27(6):810–9.

Tsui, B. M. W. & Gullberg, G. T. **1990**. *The geometric transfer-function for cone and fan beam collimators.* Phys Med Biol, 35(1):81–93.

Tuy, H. K. **1983**. *An Inversion Formula for Cone-Beam Reconstruction.* SIAM Journal on Applied Mathematics, 43(3), 546-552. doi: 10.1137/0143035

Vaissier, P. E. B., *et al.* **2012**. *Fast Spiral SPECT with Stationary γ-Cameras and Focusing Pinholes.* J Nucl Med, 53(8), 1292-1299. doi: 10.2967/jnumed.111.101899

van Audenhaege, K., *et al.* **2015**. *Review of spect collimator selection, optimization, and fabrication for clinical and preclinical imaging.* Med Phys, 42(8):4796–4813.

van der Have, F., *et al.* **2009**. *U-SPECT-II: An Ultra-High-Resolution Device for Molecular Small-Animal Imaging.* J Nucl Med, 50(4), 599-605. doi: 10.2967/jnumed.108.056606

van der Laan, *et al.*. **2010**. *Optical simulation of monolithic scintillator detectors using GATE/GEANT4.* Phys Med Biol, 55(6), 1659-1675. doi: 10.1088/0031-9155/55/6/009

van Roosmalen, J., *et al.* **2015**. *Optimization of a High Resolution Focussed Molecular Breast Tomosynthesis Device.* Paper presented at the 2015 IEEE Nuclear Science Symposium and Medical Imaging Conference (NSS/MIC).

van Roosmalen, J.,*et al.* **2016**. *Molecular breast tomosynthesis with scanning focus multi-pinhole cameras.* Phys Med Biol, 61(15), 5508. doi: 10.1088/0031-9155/61/15/5508

van Roosmalen, J., *et al.*. **2017**. *System geometry optimization for Molecular Breast Tomosynthesis with focusing multi-pinhole collimators.* Physics in Medicine and Biology, 63(1), 15018, doi: 10.1088/1361-6560/aa9265

Vastenhouw, B., & Beekman, F. **2007**. *Submillimeter total-body murine imaging with U-SPECT-I.* J Nucl Med, 48(3), 487-493.

Vunckx, K., *et al.* **2008**. *Effect of Overlapping Projections on Reconstruction Image Quality in Multipinhole SPECT.* IEEE Trans Med Imag, 27(7), 972-983. doi: 10.1109/TMI.2008.922700

Wackers, F. J. T., *et al.* **1989**. *Technetium-99m Hexakis 2-Methoxyisobutyl Isonitrile: Human Biodistribution, Dosimetry, Safety, and Preliminary Comparison to Thallium-201 for Myocardial Perfusion Imaging.* J Nucl Med, 30(3), 301-311.

Walrand, S., **2002**. *Acquisition of linograms in spet: implementation and benefits.* Eur J Nucl Med Mol Img, 29(9):1188–1197.

Wang, B., *et al.* **2016**. *Fast and accurate ray-tracing simulation of multi-pinhole Molecular Breast Tomosynthesis.* Paper presented at the Society of Nuclear Medicine and Molecular Imaging Annual Meeting.

Wang B, *et al.* **2017** *Voxelized ray-tracing simulation dedicated to multi-pinhole molecular breast tomosynthesis* Biomed. Phys. Eng. Express, 3(4), 045021. doi: 10.1088/2057-1976/aa8012

Wang, H. L., *et al.***1993**. *A New Composite Model of Objects for Monte-Carlo Simulation of Radiological Imaging.* Phys Med Biol, 38(9), 1235-1262. doi: 10.1088/0031-9155/38/9/005

Wang, H., *et al.* **1996**. *Prone breast tumor imaging using vertical axis-of-rotation (VAOR) SPECT systems: an initial study.* Paper presented at the Nuclear Science Symposium Conference Record.

Weinmann, A. L., *et al.* **2009**. *Design of optimal collimation for dedicated molecular breast imaging systems.* Med Phys, 36(3), 845-856. doi: 10.1118/1.3077119

Weissleder, R. **2010**. Molecular imaging: principles and practice: PMPH-USA.

Wernick, M. N., & Aarsvold, J. N. **2004**. *Emission tomography: the fundamentals of PET and SPECT*: Academic Press.

Williams, M. B., *et al.* **2010**. *Dual-Modality Breast Tomosynthesis.* Radiology, 255(1), 191-198. doi: doi:10.1148/radiol.09091160

Williams, M. B., *et al.* **2003**. *Analysis of position-dependent Compton scatter in scintimammography with mild compression.* IEEE Trans Nucl Sci, 50(5), 1643-1649. doi: 10.1109/Tns.2003.817297

Yanagida, T., *et al.* **2010**. *Development of Pr:LuAG Scintillator Array and Assembly for Positron Emission Mammography.* IEEE Trans Nucl Sci, 57(3), 1492-1495. doi: 10.1109/Tns.2009.2032265

Zackrisson, S., & Houssami, N. **2016**. *Evolution of Mammography Screening: From Film Screen to Digital Breast Tomosynthesis* Breast Cancer Screening (pp. 323-346). Boston: Academic Press.

Zbijewski, W., & Beekman, F. J. **2006**. *Comparison of methods for suppressing edge and aliasing artefacts in iterative x-ray CT reconstruction.* Phys Med Biol, 51(7), 1877-1889. doi: 10.1088/0031-9155/51/7/017

Acknowledgements

This thesis would not have been possible without the help and support of many people. First, I would like to thank Marlies for hiring me and for being my daily supervisor. She always had suggestions and ideas whenever I got stuck, and questions to keep me sharp. Moreover, her valuable feedback resulted in more precise and clearer papers. Secondly, I would like to thank Freek for acting as my Promotor. He often provided a valuable outside perspective, that helped me see how readers might perceive my work. And, although it wasn't always easy to hear, his keen scientific insight helped us to keep an eye on other possible solutions and techniques. This also helped in strengthening our reasoning and conclusions.

Over the years, the other group members provided me with interesting discussions and sparring sessions. Frans and Brendan helped me, especially in the first years, with their deep knowledge of the different software codes used in our group. I thank Pieter Vaissier for the many discussions, brainstorm sessions and opportunities to share our frustrations when the research didn't progress as we'd like it to. Sasha started her PhD just a few months before me, so we had a lot of common experiences. She became a better friend to me than I could have wished for, and I'm grateful for that. Moreover, I would like to thank her for creating the cover of this thesis, the illustrations in the chapters, and for agreeing to be one of my paranimphs.

My project would not have been possible without the organizational support provided by Trudy (and before her by Thea). Whenever the research was tough, the coffee breaks and lunches with everyone from our group and the luminescent materials research group provided a welcome distraction. Thanks to (in random order): Beien, Yuan, Minh, Rob, Jan, Misha, Romee, Edith, David, Hongde, Michiel, Roy, Melvin, Anna, Adrie, John, Johan, Weronika, Pieter Dorenbos, Erik, Evert, and anyone I might have forgotten. Moreover, often we would go with a group to "'t Koepeltje" or for dinner in Delft. There was a core group of people, with whom we shared many evenings, and we also had a great trip to Poland: Beien, Hongde, Roy, Anna and Weronika, thanks for the fond memories.

During my project, I had the pleasure of working with many talented students. They often brought a lot of energy into the group: Matthias, Marcel, Stefan, Fedde, Witek, Jonathan, Stephan, Edwin, Siem, Thijs, Jeroen, Stef, Atia, Rens, Kathalijne and a large number of PEP students. Thanks for all the interesting discussions.

And last but not least my family. I would like to thank my parents Kees and Sjan, my brother Lars and his wife Bo for their support. You were there for me to celebrate the successes but also to help me through the rough times. Lars, thank you for being a paranimph. Sjan and Kees, our many conversations helped me learn deal with the frustrations of doing a PhD, and your support helped me through.

Publications list

Peer-reviewed international journal articles

Prins, C. R., Ten Thije Boonkkamp, J. H. M., **van Roosmalen, J.**, IJzerman, W. L, & Tukker, T. W. **2014** *A Monge-Ampère-solver for free-form reflector design.* SIAM J. Sci. Comput., 36(3), B640-B660

Goorden, M.C., **van Roosmalen, J.**, van der Have, F., & Beekman, F. J., **2016** *Optimizing modelling in iterative image reconstruction for preclinical pinhole PET.* Phys. Med. Bio., 61, 3712

van Roosmalen, J., Goorden, M. C., & Beekman, F. J. **2016**. *Molecular breast tomosynthesis with scanning focus multi-pinhole cameras.* Phys. Med. Bio., 61, 5508.

van Roosmalen, J., & Goorden, M. C. **2017** *Non-diverging analytical expression for the sensitivity of converging SPECT collimators*, Phys. Med. Bio, 62, N228

Wang, B.*, **van Roosmalen, J.***, Piët, L., van Schie, M. A., Beekman, F. J. and Goorden, M. C., **2017** *Voxelized ray-tracing simulation dedicated to multi-pinhole molecular breast tomosynthesis*, Biomed. Phys. Eng. Express, 3(4), 045021
equal contribution

van Roosmalen, J., Beekman, F. J., & Goorden, M. C. **2017** *System geometry optimization for Molecular Breast Tomosynthesis with focusing multi-pinhole collimators.* Phys. Med. Bio., 63, 015018

van Roosmalen, J., Beekman, F. J., & Goorden, M. C. **2018** *Comparison of fan beam, slit-slat and multi-pinhole collimators for Molecular Breast Tomosynthesis.* Phys. Med. Bio. *63, 105009*

Conference Abstracts

van Roosmalen, J., Goorden, M. C., & Beekman, F. J., *Molecular breast tomosynthesis with a dedicated focusing pinhole geometry.* SNMMI Annual Meeting 2015, Baltimore, MD

Beekman, F. J., van der Have, F., Goorden, M. C., Vaissier, P. E. B., **van Roosmalen, J.,** During, H., & Vastenhouw, B. *G-SPECT-I: a full ring high sensitivity and ultra-fast clinical molecular imaging system with <3 mm resolution.* EANM 2015, Hamburg, Germany

van Roosmalen, J., Goorden, M. C., & Beekman, F. J. , *Optimizatio of a high resolution focussed Molecular Breast Tomosynthesis device.* IEEE NSS/MIC 2015, San Diego, CA

Wang, B., **van Roosmalen, J.**, Piët, L., van Schie, M. A., Beekman, F. J. and Goorden, M. C., *Fast and accurate ray-tracing simulation of multi-pinhole Molecular Breast Tomosynthesis.* SNMMI Annual Meeting 2016, San Diego, CA
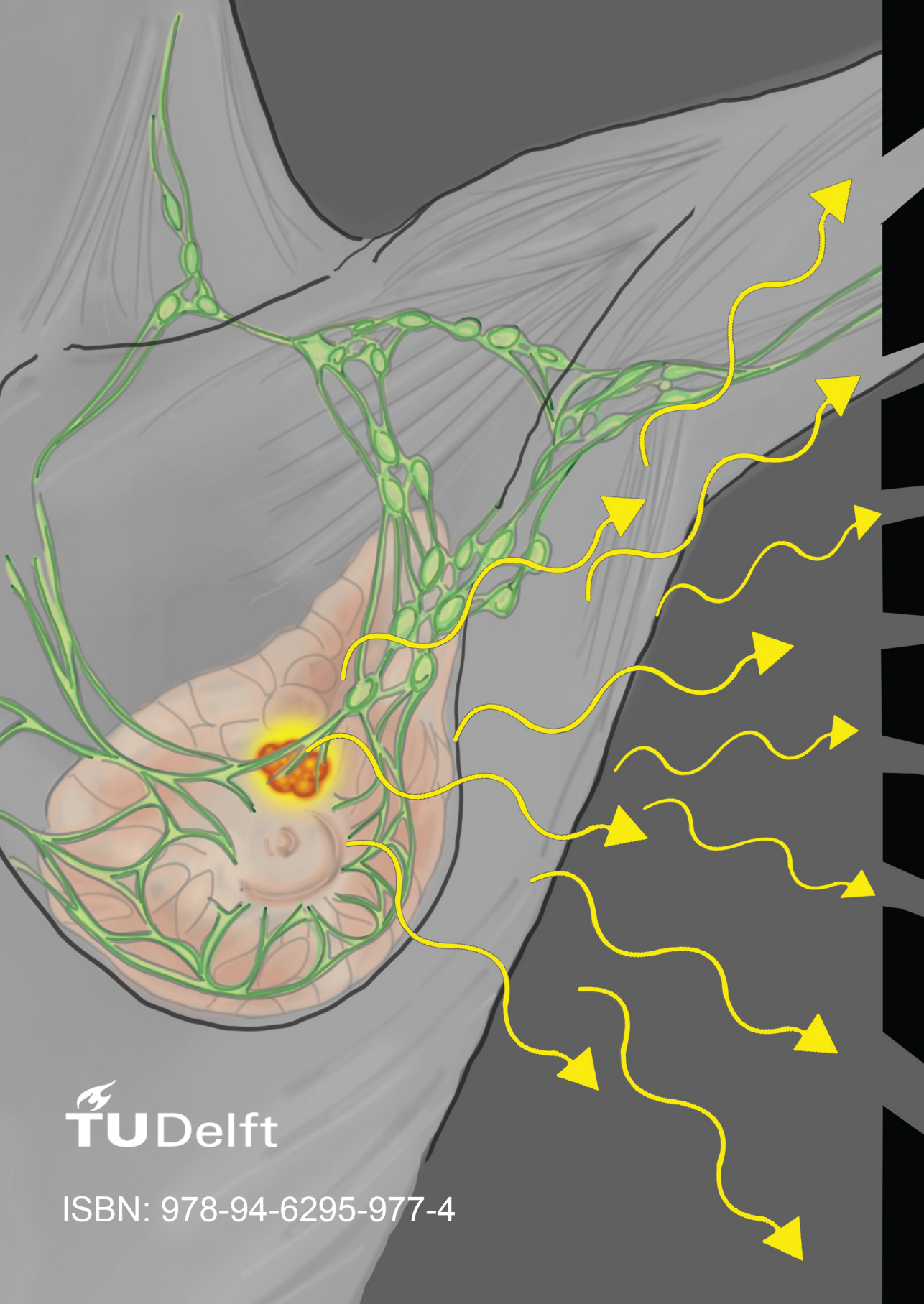
van Roosmalen, J., Beekman, F. J., & Goorden, M. C. *Non-diverging analytical expression for the sensitivity of converging SPECT collimators.* IEEE NSS/MIC 2016, Strasbourg, France

van Roosmalen, J., Beekman, F. J., & Goorden, M. C. , *Comparing multi-pinhole and fan beam collimation for Molecular Breast Tomosynthesis.* SNMMI Annual Meeting 2017, Denver CO

van Roosmalen, J., Beekman, F. J., & Goorden, M. C. , *Optimizing molecular breast tomosynthesis with slit-slat collimators.* IEEE NSS/MIC 2017, Atlanta, GA

Curriculum Vitae

Jarno van Roosmalen was born on march 14, 1987 in 's-Hertogenbosch. In 2005 he finished secondary school (VWO) at the Zwijssen College Veghel. In the same year, he started studying at Eindhoven University of Technology. He completed a combined first year program of Applied Physics and Applied Mathematics. He continued to pursue a BSc and followed by a MSc in Industrial and Applied Mathematics and completed the latter in 2013. In the same year he started working on his PhD project in the Radiation Detection and Medical Imaging group of prof. Beekman at Delft University of Technology.